DIPLOMARBEIT

Yttria-Stabilized-Zirconia: Metastable Phases, Oxygen Vacancies and Water Adsorption
– A First Principles Study –

zur Erlangung des akademischen Grades

Diplom-Ingenieur

im Rahmen des Studiums

Technische Physik

eingereicht von

Thomas Mayer
Matrikelnummer 01025782

ausgeführt am Institut für Angewandte Physik
der Fakultät für Physik der Technischen Universität Wien

Betreuung
Betreuer: Ao.Univ.Prof. Dipl.-Ing. Dr.techn. Josef Redinger
Mitwirkung: Projektass.(FWF) Dr.techn. Wernfried Mayr-Schmölzer
Projektass.(FWF) Ing. Jakub Planer
Privatdoz. Dipl.-Ing. Dr.techn. Florian Mittendorfer

Wien, 01.02.2019

(Unterschrift Verfasser)

(Unterschrift Betreuer)

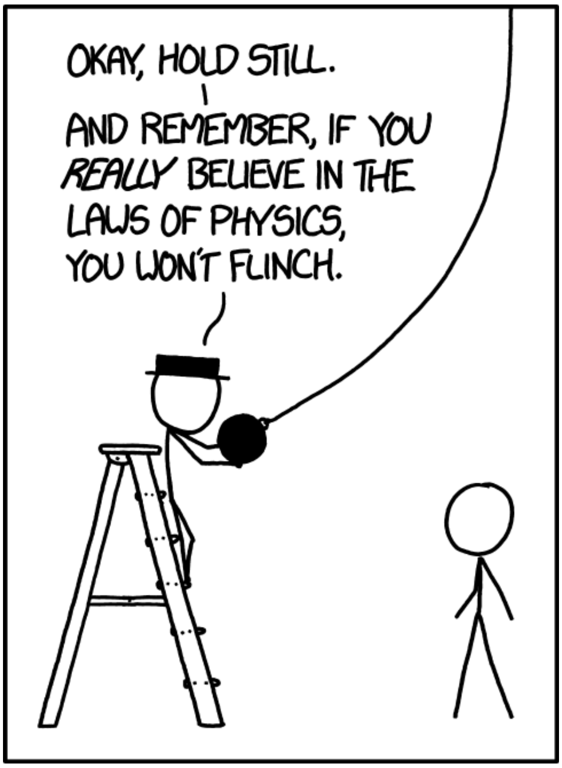

From: XKCD - A Webcomic Of Romance, Sarcasm, Math, And Language

Abstract

The aim of this thesis was to get an overview of the bulk and surface properties of Yttria-Stabilized-Zirconia (YSZ) by the use of Density Functional Theory (DFT). The investigated bulk concentrations were 3, 7, 10, 14 and 33 mol%, with special emphasis on cubic stabilized zirconia at amounts of 10 mol% Y_2O_3 doped to c-ZrO_2. For brevity we denote x mol% Y_2O_3 doped to cubic ZrO_2 as xYSZ. To create the bulk configurations, the special quasi-random structure approach from the Alloy Theoretic Automated Toolkit (ATAT) by Axel van de Walle was used. Also metastable phases were obtained during the bulk relaxations. A phonon investigation showed a phonon driven phase transition to a tetragonal-like phase in pure c-ZrO_2 and 3YSZ. In addition, another metastable monoclinic-like phase also occurred in YSZ, where the PBE functional predicted the wrong order of stability. Since these metastable phases got energetically unfavorable when using the SCAN functional and have not yet been found in any experiment, this wrong order of stability must be considered as a PBE artifact.

Afterwards, different 10YSZ(111) surfaces were investigated with special attention on one cut directly from the most favorable YSZ bulk structure and one concerning yttria segregation to the subsurface. The last part of this thesis contains adsorption studies of water on exactly these two surfaces with respect to the chemical environment of the adsorption site. In both cases the influence of nearby oxygen vacancies was considered and they seem to have a greater effect on the surface stability than on water adsorption.

Kurzfassung

Das Ziel dieser Arbeit war es, einen Überblick über die Eigenschaften von Yttria-Stabilisiertem-Zirkonia (YSZ) zu bekommen. Dafür wurde die Dichtefunktional Theorie verwendet. Es wurden Konzentrationen von 3, 7, 10, 14 und 33 mol% Y_2O_3 in c-ZrO_2 untersucht und dabei besonderes Augenmerk auf kubisch stabilisiertes Zirkonia bei 10 mol% Y_2O_3 gelegt. In dieser Arbeit wird für x mol% Y_2O_3 in kubischem ZrO_2 die Kurzform xYSZ verwendet. Um die Kristallphasen zu beschreiben, wurde der Ansatz spezieller quasi-zufälliger Strukturen verwendet. Während den Relaxationen tauchten auch metastabile Phasen auf und eine Phononenanalyse für kubisches ZrO_2 zeigte, dass ein Phononen getriebener Übergang zu einer tetragonal ähnlichen Strukturen in ZrO_2 und 3YSZ besteht. Außerdem fiel auf, dass das PBE Funktional sowohl diese tetragonal ähnliche, als auch die metamonokline Phase als energetisch am günstigsten einstufte. Dies wurde als PBE Artefakt behandelt, da sowohl das SCAN Funktional die richtige Reihenfolge liefert als auch Experimente bisher noch keinen eindeutigen Beweis für derartige Phasen erbrachten.

Danach wurden unterschiedliche 10YSZ(111) Oberflächenkonfigurationen untersucht, wobei hier das Augenmerk auf einer Festkörper ähnlichen und einer mit Yttrium Segregation lag. Im letzten Teil dieser Arbeit wurde noch das Verhalten bei Wasser Adsorption untersucht. Dabei wurde das chemische Umfeld der Adsorptionsplätze, vor allem in Bezug auf Sauerstoff Leerstellen, berücksichtigt und deren Auswirkung auf die Oberflächen- und Adsorptionsenergie analysiert.

Contents

1 Introduction 6

2 Fundamentals 7
- 2.1 Density Functional Theory . . . 7
  - 2.1.1 Hartree-Fock Approximation . . . 7
  - 2.1.2 Hohenberg-Kohn-Sham Theorem . . . 9
  - 2.1.3 Local Density Approximation - LDA . . . 11
  - 2.1.4 Generalized Gradient Approximation - GGA . . . 11
  - 2.1.5 Meta Generalized Gradient Approximation - meta-GGA . . . 12
  - 2.1.6 Hybrid Exchange Functionals . . . 12
- 2.2 VASP . . . 13
- 2.3 ATAT - MCSQS . . . 14
- 2.4 Birch-Murnaghan Equation of State . . . 16
- 2.5 Zirconia ZrO_2 . . . 17
- 2.6 Yttria Y_2O_3 . . . 20
- 2.7 Yttria-Substituted-Zirconia YSZ . . . 22
  - 2.7.1 The Ion Conductivity of YSZ . . . 22
  - 2.7.2 The Phases of YSZ . . . 23
- 2.8 Convergence - K-Point Grid and Energy Cut-Off . . . 26

3 Results and Discussion I 27
- 3.1 YSZ Bulk Properties . . . 27
  - 3.1.1 Lattice Parameter and Enthalpy of Formation . . . 27
  - 3.1.2 Metastable YSZ Phases . . . 32

4 Results and Discussion II 39
- 4.1 YSZ(111) Surface Configurations and -Energies . . . 39
- 4.2 Adsorption of H_2O on c-YSZ(111) . . . 44

5 Summary and Conclusion 53

6 Acknowledgements 55

Bibliography 56

Appendix 67
- List of Abbreviations . . . 67
- Conversion Table for YSZ . . . 68
- Characteristics of some Molecules . . . 68
- Density of States and STM-Images . . . 70

1 Introduction

This thesis tries to provide a deeper understanding of Yttria-Stabilized-Zirconia (YSZ), concerning its bulk phases, the (111) surface and also its adsorption behavior with water molecules on this surface.

YSZ is especially used in Solid-Oxide-Fuel-Cells (SOFCs) as electrolyte, due to its extraordinary high ion conductivity. ZrO_2 and YSZ both are used in a wide range of applications and because of their good mechanical durability and their good electronic and thermal insulating qualities as a ceramic, ZrO_2 for example is also used in microcrystalline form as smartphone rear-side material. Besides a good ionic conductivity, YSZ is corrosion resistant, chemically stable at high temperatures and exhibits an extraordinary micro hardness. Therefore it is also used for high temperature applications such as thermal barrier coatings for turbine engine components.

Due to the fact that for SOFCs and Solid-Oxide-Electrolysis-Cells (SOECs) the focus is on fuels that are readily available, such as hydrogen or synthesis gas, the understanding of the interface reaction with water is very important. The reaction on the anode is $H_2 + O^{2-} \rightarrow H_2O + 2e^-$, on the cathode $1/2O_2 + 2e^- \rightarrow O^{2-}$ which leads to $2H_2 + O_2 \rightarrow 2H_2O$ in total. In this thesis large 2x2x2 bulk models of up to 96 atoms and large surface models of 186 atoms in 4 trilayers were used. These models are needed to describe the effects of long range lattice relaxations in the bulk, especially around the oxygen defects (V_O) created by the doping, but also in the slab structures during water adsorption. In the case of larger cells and with periodic boundary conditions, vacancy-vacancy interactions and Y–V_O–Y defect cluster interactions can also be studied with adequate defect distances between them.

The first part of the present thesis includes a short description of the fundamentals, including the simulation setup, followed by the discussion of crystal structure and lattice properties of ZrO_2, Y_2O_3 and YSZ calculated via different functionals. In addition different YSZ(111) surfaces, one bulk-like surface and one surface including yttrium subsurface segregation, were investigated and water adsorption energies were calculated for these different settings. The results were compared to recent experimental results, as well as to other first-principles calculations about this topic.

The last section gives a short summary about the treated topics and a brief conclusion with possible future work.

2 Fundamentals

2.1 Density Functional Theory

2.1.1 Hartree-Fock Approximation

For the last decades Density Functional Theory (DFT) has been the dominant method for quantum mechanical simulations of periodic systems. In recent years it has also been adopted by other branches of science to simulate atoms, molecules, solids, surfaces, nuclei, quantum and classical fluids, adsorption behaviors, etc. In this section the basic concepts of DFT should be introduced to understand the background of this theory and get familiar with the workhorse of matter simulations.
The DFT is derived from the N-particle Schrödinger equation, which in the Born-Oppenheimer approximation, non-relativistic and time independent is

$$\hat{H}^{el}\Psi_N\left(\mathbf{x_1},\mathbf{x_2},...,\mathbf{x_N}\right)=E_N\Psi_N\left(\mathbf{x_1},\mathbf{x_2},...,\mathbf{x_N}\right)\qquad\text{with}\qquad\hat{H}\left(r_i,R_c\right)\equiv\hat{H}^{el}_{R_c}\left(r_i\right)\tag{2.1}$$

where $\mathbf{x}_i$ = $\mathbf{r}_i(x_i,y_i,z_i)\otimes\sigma(\pm\frac{1}{2})$ are the electron coordinates and spin, R_c are the nucleus coordinates and $\widehat{H}^{el}$ is the Hamiltonian

$$\hat{H}^{el}=\sum_{i=1}^{N}\underbrace{\left(-\frac{\nabla_i^2}{2}-\sum_c\frac{Z_c}{r_{ic}}\right)}_{\hat{h}_i}+\frac{1}{2}\sum_{i=1}^{N}\sum_{j\neq i}^{N}\underbrace{\frac{1}{r_{ij}}}_{\hat{\omega}_{ij}}\tag{2.2}$$

$\widehat{H}^{el}$ consists of three terms, the kinetic energy, the interaction with the external potential V_{ext} generated by the nuclei and the electron-electron interaction V_{ee}. Therefore the external potential for materials simulation is given by the interaction of the electrons with the atomic nuclei, with $r_{ic}=|\mathbf{r}_i-\mathbf{R}_c|$ the distance between the electron i at position $\mathbf{r}_i$ and nuclei at $\mathbf{R}_c$. To simplify the notation, the notation of the spin coordinate is neglected throughout this section. Besides, $\hat{h}_i$ describes the single particle part and $\hat{\omega}_{ij}$ describes the two particle interaction part. In the case of electrons, equation 2.1 is solved for a set of antisymmetric Ψ, so they change sign if the coordinates of two arbitrary electrons are interchanged. E_0 corresponds to the lowest energy eigenvalue, the ground state energy, where $|\Psi_0|^2$ describes the probability density of finding an electron with any particular set of coordinates $\mathbf{r}_i$. The average total energy for a state specified by a particular Ψ, which is the expectation value of $\hat{H}$, is

$$E_N\left[\Psi_N\right] = \frac{\langle \Psi_N\left(\mathbf{x_1}, ..., \mathbf{x_N}\right)|\hat{H}^{el}|\Psi_N\left(\mathbf{x_1}, ..., \mathbf{x_N}\right)\rangle}{\langle \Psi_N\left(\mathbf{x_1}, ..., \mathbf{x_N}\right)|\Psi_N\left(\mathbf{x_1}, ..., \mathbf{x_N}\right)\rangle} \tag{2.3}$$

This emphasizes, that the energy is a functional of the wavefunction Ψ. The resulting energy is higher than that of the ground state E_0 unless Ψ is equivalent to Ψ_0, which leads to the variational theorem $E[\Psi] \geq E_0$ [1].

The wavefunction and energy that deliver the ground state may be found by searching all possible wavefunctions for the one that minimizes the total energy. The ansatz for the structure of Ψ in the Hartree-Fock theory is assumed to be an antisymmetric product of single electron functions ϕ_i, received via the Slater-determinant. This splitting of the many body problem into single particle problems is called the Hartree-Fock approximation.

$$\Psi_{HF} = \frac{1}{\sqrt{N!}}\begin{vmatrix} \phi_1(x_1) & \phi_2(x_1) & \dots & \phi_N(x_1) \\ \phi_1(x_2) & \phi_2(x_2) & \dots & \phi_N(x_2) \\ \vdots & \vdots & \ddots & \vdots \\ \phi_1(x_N) & \phi_2(x_N) & \dots & \phi_N(x_N) \end{vmatrix} \tag{2.4}$$

Inserting this ansatz into the Schrödinger-Equation 2.1 results in an expression for the Hartree-Fock energy

$$E_{HF}[\phi_i] = \sum_{\alpha}^{N}\langle\phi_\alpha|\hat{h}|\phi_\alpha\rangle + \frac{1}{2}\sum_{\alpha}^{N}\sum_{\gamma\neq\alpha}^{N}\left(\langle\phi_\alpha\phi_\gamma|\hat{\omega}|\phi_\gamma\phi_\alpha\rangle - \langle\phi_\alpha\phi_\gamma|\hat{\omega}|\phi_\alpha\phi_\gamma\rangle\right) \tag{2.5}$$

Now one can use the Rayleigh-Ritz method to vary E as a functional of ϕ_i. To conserve the orthogonality of the single particle wave functions, the functional $\mathcal{L}$ is used with the method of Lagrange multipliers ε_{ij} and with constraint of pairwise orthogonal orbitals $\delta_{ij} - \langle\phi_i|\phi_j\rangle \overset{!}{=} 0$. In addition a basis $\tilde{\phi}_i$ is used, where ε_{ij} is diagonal $\varepsilon_{ij} = \varepsilon_i\delta_{ij}$.

$$\mathcal{L} = E[\{\phi_i\}] - \sum_{i}^{N}\sum_{j}^{N}\varepsilon_{ij}\left(\delta_{ij} - \langle\phi_i|\phi_j\rangle\right) = E[\{\tilde{\phi}_i\}] - \sum_{i}^{N}\varepsilon_i\left(1 - \langle\tilde{\phi}_i|\tilde{\phi}_i\rangle\right) \tag{2.6}$$

During further calculation, the tilde was omitted. Now $\mathcal{L}$ can be minimized with respect to ϕ_i using the variation $\partial\mathcal{L}/\partial\phi_i^*$. With the Fock-operator $\hat{F}$, this leads to the Hartree-Fock equations

$$\sum_i \left(\langle\delta\phi_i|\hat{F}|\phi_i\rangle + \langle\phi_i|\hat{F}|\delta\phi_i\rangle\right) \overset{!}{=} \sum_i \varepsilon_i \left(\langle\delta\phi_i|\phi_i\rangle + \langle\phi_i|\delta\phi_i\rangle\right) \quad \text{and} \quad \hat{F}|\phi_i\rangle = \varepsilon_i|\phi_i\rangle \tag{2.7}$$

This is a non-linear equation with a non-local integro-differential-operator and for N electrons, one gets 2N coupled integro-differential-equations. The Hartree-Fock equations describe non-interacting electrons under the influence of a mean field potential consisting of the classical Coulomb potential and a non-local exchange potential. Solving this equations is very time consuming, because the integration has to be done always for all considered wavefunctions and this scales with N!. For the case of planar waves, one can calculate the energy and exchange part analytically with the one particle energy of $E\left(\mathbf{k}\right) = k^2 - \varepsilon_x\left(\mathbf{k}\right)$. Summarizing over all occupied states via an integral limited by be Fermi-wavevector, which is the radius for a spherical Fermi-surface, delivers the contribution to the exchange energy by

$$E_x = -\left(\frac{3e^2}{2}\right) \cdot \left(\frac{3\rho}{8\pi}\right)^{\frac{1}{3}} \tag{2.8}$$

So for the free electron gas the exchange energy is proportional to $\rho^{\frac{1}{3}}$, which is also the ansatz for the Local Density Approximation (LDA). The generalization of this result leads to theories in which the total energy of a many body system is given by a functional of the density.

2.1.2 Hohenberg-Kohn-Sham Theorem

In 1964 Pierre Hohenberg and Walter Kohn published their two theorems concerning the relationship between the electron density and the ground state of a system [2].

- The ground state energy E_0 of a system of N identical particles in an external potential V_{ext} is a distinct functional of the particle density $\rho(\mathbf{r})$, $E_0 = E[\rho[\mathbf{r}]]$.
- This functional has its minimum, with respect to the variation $\partial\rho_(\mathbf{r})$ of the particle density, at an equilibrium density $\rho_0(\mathbf{r})$ with given external potential.

Concerning the Hamiltonian from equation 2.2, one may write the functional as

$$E[\rho] = T[\rho] + V_{ext}[\rho] + V_{ee}[\rho] \tag{2.9}$$

The external potential V_{ext} is given by the Coulomb interaction between electrons and cores, while the kinetic energy T and the many body interaction V_{ee} are unknown. So with good approximations for these two functionals, the minimization of the energy would be possible. Kohn and Sham introduced a fictitious system of N non-interacting electrons to be described by a single determinant wavefunction. Now the kinetic energy $T_s[\rho] = -1/2\sum_i \langle\phi_i|\nabla^2|\phi_i\rangle$ and also the electron density $\rho(\mathbf{r}) = \sum_i |\phi_i(\mathbf{r})|^2$ are known exactly from the orbitals. The energy functional and exchange-correlation functional itself can also be rearranged as

$$\begin{aligned} E[\rho] &= T_s[\rho] + V_{ext}[\rho] + V_H[\rho] + E_{xc}[\rho] \quad \text{with} \\ E_{xc}[\rho] &= (T[\rho] - T_s[\rho]) + (V_{ee}[\rho] - V_H[\rho]) \end{aligned} \tag{2.10}$$

V_H is the classical Coulomb interaction or Hartree energy and $E[xc]$ is simply the sum of the error made by using the previously mentioned non-interacting kinetic energy and using classical electron-electron interaction. Applying the variational theorem with the constraint of particle conservation, this leads to the so called Kohn-Sham equations, which deliver the conditions for the orbitals that minimize the energy.

$$\begin{aligned} &\left\{ -\frac{\hbar}{2m}\nabla^2 + \underbrace{V(\mathbf{r}) + e^2\int \frac{\rho(\mathbf{r}')}{|\mathbf{r}-\mathbf{r}'|}d^3r' + \mu_{xc}[\rho(\mathbf{r})]}_{V_{eff}} \right\} \phi_i(\mathbf{r}) = \varepsilon_i\phi_i(\mathbf{r}) \\ &E = \sum_i \varepsilon_i + \frac{e^2}{2}\int\int \frac{\rho(\mathbf{r})\rho(\mathbf{r}')}{|\mathbf{r}-\mathbf{r}'|}d^3r d^3r' + \int \rho(\mathbf{r})\left\{\varepsilon_{xc}[\rho(\mathbf{r})] - \mu_{xc}[\rho(\mathbf{r})]\right\} d^3r \end{aligned} \tag{2.11}$$

This means that the non-interacting particles move in a local effective external potential V_{eff}, called the Kohn-Sham potential. In this case the total energy consists of the energies of the single non-interacting particles ε_i, the Coulomb interaction part and the exchange-correlation term, where ε_{xc} denotes the exchange energy per particle of a homogeneous electron gas and $\mu_{xc}[\rho(\mathbf{r})] = \partial E_{xc}[\rho(\mathbf{r})]/\partial\rho(\mathbf{r})$ contains the exact exchange-correlation potential [3]. This approach results in an exact correspondence of the density and ground state energy of a system consisting of non-interacting particles and the many body system described by the Schrödinger equation, but this is only exact if the exact functional is known. In principle it is possible to solve the Schrödinger equation for any given system to calculate the energy and potential, but usually simplified functionals, which have to fulfill physical requirements, are used. The computational cost for solving equations 2.11 scales with N^3, but this can be dropping down to N, when using the locality of the orbitals. In total it is much cheaper in computation time than the Hartree-Fock or any other wavefunction method.

2.1.3 Local Density Approximation - LDA

The Local Density approximation uses only the local kinetic and exchange densities of the non-interaction homogeneous electron gas to describe the total energy functional. So within the LDA the exchange correlation energy per particle $\varepsilon_{xc}(\rho)$ is only a function of the local value of the electron density and can be separated into an exchange and correlation term $\varepsilon_{xc}(\rho) = \varepsilon_x(\rho) + \varepsilon_c(\rho)$.

$$E_{xc}^{LDA}[\rho(\mathbf{r})] = \int \rho(\mathbf{r}) \cdot \varepsilon_{xc}(\rho) \cdot d^3r \tag{2.12}$$

By the usage of techniques like Quantum Monte Carlo simulations, the correlation energy density can be calculated with good accuracy for some systems.

The LDA is a remarkable efficient and profitable approximation that has been used for the last decades to get reasonable results for many inhomogeneous systems. Properties like elastic moduli, vibrational frequencies, structure and phase stability are described in an adequate way. However, the calculated electronic structure for metals is in good agreement with theory and experimental results, but for stronger correlated systems like semiconductors or insulators, LDA delivers divergent or wrong results. Also the energy barriers for diffusion in chemical reactions may be too small, the binding energy is overestimated and the lattice parameters are underestimated, due to over-binding of the atoms.

2.1.4 Generalized Gradient Approximation - GGA

This Approximation uses a functional not only dependent on the local density, but also dependent on its gradient, so first order gradient terms are included in order to account the non-homogeneity of the electron density. The common form of a GGA functional is

$$E_{xc}^{GGA}[\rho(\mathbf{r})] = \int \rho(\mathbf{r}) \cdot \varepsilon_{xc}(\rho, \nabla\rho) \cdot d^3r \tag{2.13}$$

Nevertheless, the density and its gradient still supply only local information. Compared to the LDA, the GGA can deliver much better results for the lattice parameters and also the calculated total energies for atoms and molecules are more accurate, making it the standard tool in nowadays DFT calculations. In contrast to experimental values, the bond lengths and lattice parameters are often overestimated. In most instances nowadays the functional by Perdew et al. [4] PBE is used, due to its advantage of an analytical fit to the numerical GGA over other GGAs.

2.1.5 Meta Generalized Gradient Approximation - meta-GGA

Including second order gradient terms leads to potentially more accurate functionals, referred as meta-GGA functionals. Therefore they include the second order derivative of the electron density. Recently functionals depend not only on the Laplacian of the electron density, but could depend also on the Laplacian of the spin density or the local kinetic energy density.

$$E_{xc}^{mGGA}[\rho(\mathbf{r})] = \int \rho(\mathbf{r}) \cdot \varepsilon_{xc}(\rho, \nabla\rho, \nabla^2\rho, \tau) \cdot d^3r \quad \text{with} \quad \tau(\mathbf{r}) = \frac{1}{2} \cdot \sum_{i}^{occupied} |\nabla^2\phi_i(\mathbf{r})|^2 \tag{2.14}$$

So the exchange-correlation potential becomes orbital dependent. The usage of meta-GGAs usually leads to pretty good descriptions of equilibrium structures with an error of 5% or less compared to the experiment, even for some correlated systems. Also the accuracy of surface- and adsorption energies improves, compared to GGAs. One functional that fulfills nearly all known constraints for the exact density functional is the so called Strongly Constrained and Appropriately Normed Semilocal Density Functional (SCAN) meta-GGA [5]. In addition it is computational efficient, nonempirical and superior to most other GGAs and meta-GGAs for a wide range of properties.

2.1.6 Hybrid Exchange Functionals

Another way is to incorporate a certain amount of exact exchange from the Hartree-Fock theory to a local or semilocal density functional. A simple form describing this mixing is

$$E_{xc}^{hyb}[\rho(\mathbf{r})] = \alpha E_x^{HF} + (1+\alpha)E_x^{GGA} + E_c^{GGA} \tag{2.15}$$

where α is the mixing parameter, but various other types of mixing and hybrid functionals exist. The resulting functionals are referred as Hartree-Fock- or DFT hybrid functionals. So the exact exchange energy functional is expressed with Kohn-Sham orbitals, which could improve the calculated properties of many molecules, such as binding energies, bond lengths or vibrational frequencies, compared to the best GGAs functionals. In comparison all of these functionals are parameterized and computationally quite expensive, due to bi-electron integrals. [6, 7]

2.2 VASP

All studies were done using the Vienna Ab Initio Simulation Package (VASP) [8–11] (Ver. 5.4.4), to get a first look onto the different bulk phases and associated surfaces of Zirconia, Yttria, Yttria-Substituted-Zirconia (YSZ) and their specific adsorption behaviors for different molecules.

VASP delivers a numerically approximate solution to the many-body Schrödinger equation by solving the Kohn-Sham or Roothaan equations within the Hartree-Fock approximation. The self consistency cycles used to calculate the electronic ground-state and evaluate the solution of the Kohn-Sham functional are based on the Residual Minimisation Method - Direct Inversion in the Iterative Subspace (RMM-DIIS) [12, 13], Sequential Conjugate Gradient Minimisation (CG) [14, 15] and a Blocked Davidson Scheme (DAV) [16, 17]. The energy functional in this case can be dependent on e.g. the local electron density, its gradient or higher derivatives, typical van-der-Waals corrections and other geometric dependencies. In addition a full featured symmetry code, which determines the symmetry of arbitrary configurations automatically, is included. The integration of the band structure energy over the Brillouin zone is performed with the linear tetrahedron method [18] or weighted k-point sums. Quantities like the one-electron orbitals, the electron charge density and the local potential are expressed in plane wave basis sets. The electron-ion interaction is described using the Projector-Augmented-Wave Method (PAW).

VASP uses four important input files. The INCAR-file gives VASP the initial parameters, the POSCAR-file contains lattice-parameters and positions for each atom used. The POTCAR-file includes the pseudopotential for each atomic species and the KPOINTS-file provides information about the used k-point mesh. In addition VASP can use input information of the electronic charge density, given by the CHGCAR file or wavefunctions given by the WAVECAR file.

Another big advantage of VASP is the possibility that one can select different functionals. For the first bulk-, surface- and molecular-adsorption studies in this thesis, to give a first overview, the Generalized Gradient Approximation (GGA) by Perdew,Burke and Ernzerhof (PBE) [4] was used. Furthermore the meta-GGA SCAN [5] and two van-der-Waals corrected density functionals (vdW-DF), the optB86b [19–22] and GrimmeD3 [23, 24], were used to compare the output of this thesis with computational and experimental results.

2.3 ATAT - MCSQS

The ATAT is a collection of tools for alloy theory developed by Axel van de Walle. The tools have been constructed in collaboration with various research groups around the world. In this thesis the Monte Carlo Generator of Special Quasirandom Structures (MCSQS) was used [25].

The basic ingredient of the method is a Monte Carlo simulated annealing loop with an objective function seeking to perfectly match the maximum number of correlation functions. Traditionally, SQS are found by a tiresome enumeration of all possible occupations of the different sites in a supercell. On the one hand, this is the only known method that really leads to a optimal SQS, but on the other hand it is only manageable for small unit cells (up to 25 atoms). This arises from the fact, that the algorithm scales with the number of atoms in the unit cell which leads to an exponential order of complexity. However, electronic structure methods and the generation of SQS via stochastic approaches [26–28] as used in the MCSQS script, can handle fairly large cells very well (more than 50 atoms). So this method is a desirable alternative to the conventional SQS algorithm, especially when comparing the computing time.

At first, the used cluster expansion formalism for multicomponent multisublattice systems used in ATAT-MCSQS has to be explained a bit more in detail [29]. The Cluster Expansion (CE) itself takes the following form:

$$q\left(\sigma\right) = \sum_{\alpha} m_{\alpha} J_{\alpha} \left\langle \Gamma_{\alpha'}\left(\sigma\right)\right\rangle_{\alpha} \tag{2.16}$$

All variables σ_i which specify the occupation of lattice site i are contained in the vector σ. If one can assume that M$_i$ different species can occupy site i, then σ_i can take the values $\sigma_i = 0, ..., M_{i-1}$. Next, a cluster α is introduced, which is a list of sites considered in the calculation of a particular correlation. In the simplest case of a binary alloy system, the α_i can only be 0 or 1 for each site, due to the fact that each site has only one compositional degree of freedom, whereas for a multicomponent system the α_i can take the values $\alpha_i = 0, ..., M_{i-1}$ (0 indicates that the site is not part of the cluster). The sum is over all possible clusters α that are symmetrically distinct under the space group of the underlying lattice. J_α are expansion coefficients or Effective Cluster Interactions (ECI) which have to be determined, m_α are multiplicities indicating the number of clusters equivalent to α by symmetry. The correlation for this cluster α is then given by the following term:

$$\rho_{\alpha}\left(\sigma\right) \equiv \left\langle \Gamma_{\alpha'}\left(\sigma\right)\right\rangle_{\alpha} \tag{2.17}$$

The average $\langle ... \rangle_\alpha$ is taken over all clusters α' that are equivalent by symmetry to cluster α. In this case $\Gamma_{\alpha'}\left(\sigma\right)$ is the cluster function, defined as

$$\Gamma\left(\sigma\right) = \prod_{i} \gamma_{\alpha_i, M_i}\left(\sigma_i\right) \tag{2.18}$$

where $\gamma_{\alpha_i,M_i}(\sigma_i)$ satisfies $\gamma_{0,M_i}(\sigma_i) = 1$ and the following orthogonality condition:

$$\frac{1}{M_i} \cdot \sum_{\sigma_i=0}^{M_{i-1}} \gamma_{\alpha_i,M_i}(\sigma_i) \cdot \gamma_{\beta_i,M_i}(\sigma_i) = \begin{cases} 1 & \text{if } \alpha_i = \beta_i \\ 0 & else \end{cases} \tag{2.19}$$

A common choice for the simplest case of binary alloys is $\gamma_{0,2}(0) = 1$, $\gamma_{0,2}(1) = 1$, $\gamma_{1,2}(0) = -1$ and $\gamma_{1,2}(1) = 1$ which is related to the famous Ising model. However, the choice of $\gamma_{0,M_i}(\sigma_i) = 1$ ensures that equation 2.18 reduces only to a product over sites within cluster α. A more detailed view of the application of ATAT for multicomponent systems is described by van de Walle [29].

One can now assume that $\rho_\alpha\left(\sigma^{rnd}\right)$ is the correlation of the fully disordered state at some presupposed composition. It is now very easy to calculate $\rho_\alpha\left(\sigma^{rnd}\right)$ due to the fact, that in the totally disordered state, site occupations are independent, which leads to:

$$\rho_\alpha\left(\sigma^{rnd}\right) = \left\langle \prod_i \gamma_{\alpha_i',M_i}(\sigma_i) \right\rangle_\alpha = \prod_i \left\langle \gamma_{\alpha_i',M_i}(\sigma_i) \right\rangle_\alpha \tag{2.20}$$

where one can compute $\left\langle \gamma_{\alpha_i',M_i}(\sigma_i) \right\rangle_\alpha$ directly from the average composition of site i. $\rho_\alpha(\sigma)$ gives the correlation of a possible SQS candidate with the relation $\Delta\rho_\alpha(\sigma) = \rho_\alpha(\sigma) - \rho_\alpha\left(\sigma^{rnd}\right)$. The objective function that should be minimized is given by:

$$Q = -\omega L + \sum_{\alpha \in A} \left| \Delta\rho_\alpha(\sigma) \right| \tag{2.21}$$

ω is a user-specified weight, diam(α) is the length of the largest pair within the cluster α and L is the largest length l such that $\Delta\rho_\alpha(\sigma) = 0$ for all clusters α with diam(α)$\leq l$. A is a set of clusters which is also user-specified and typically much bigger than the set for which one wants to match the correlations exactly. SQS are traditionally built by just using pair correlation, however, the ATAT-MCSQS allows also using multibody correlations as well which will lead to a higher accuracy for the found SQS. The objective function 2.21 itself is minimized by some common steps. All cells have a user-specified number of atoms n and the lattice sites are occupied randomly according to the composition of each sublattice. For n_s sites on a sublattice s there are n_s! possible random permutations. For each of these supercells, the best SQS is chosen via the objective function 2.21. This function is then used in a simulated annealing loop. The configurations in the loop are sampled with a probability proportional to $e^{-Q/T}$ using a Metropolis algorithm. At each step, a different random supercell of the previously generated cells is taken and two atoms within the same sublattice are permuted. Based on the Metropolis algorithm these modifications are accepted or rejected and then the resulting configuration is compared to the best SQS found so far and updated if needed.

2.4 Birch-Murnaghan Equation of State

In physics and thermodynamics, the relation of state variables given by a thermodynamic equation is a so called Equation of State (EOS). It describes the properties and states of gases, liquids and solids under a given set of physical conditions, therefore the input parameters could be pressure, volume, temperature or internal energy [30]. The best-known EOS is the ideal gas law, also called general gas equation:

$$PV = nRT = Nk_BT \longleftrightarrow P = \rho\frac{R}{M}T \quad \text{with} \quad n = \frac{m}{M}, \quad \rho = \frac{m}{V} \tag{2.22}$$

in which P is the pressure of the gas, V the volume of the gas, n the amount of moles of the substance, R the gas constant, k$_B$ the Boltzmann constant, T the temperature, m the total mass of the gas in grams, M the molar mass and ρ the density. The Birch-Murnaghan third order EOS describes the relation between the volume V of a solid and the effective outer hydrostatic pressure P. Birch claimed that there is a relation between pressure P and free energy F and so he described it with a series expansion:

$$P = \left(\frac{\partial F}{\partial V}\right)_T \quad \rightarrow \quad F = \sum_{n=1}^{\infty} a_n\epsilon^n \quad \text{with} \quad \epsilon = \frac{1}{2}\left[1 - \left(\frac{V}{V_0}\right)^{-\frac{2}{3}}\right] \tag{2.23}$$

where ϵ corresponds to the Eulerian strain components. After carrying out this series expansion one gets the relation between pressure P and volume V:

$$P\left(V\right) = \frac{3B_0}{2}\left[\left(\frac{V_0}{V}\right)^{\frac{7}{3}} - \left(\frac{V_0}{V}\right)^{\frac{5}{3}}\right]\left[1 + \frac{3}{4}\left(B_0' - 4\right)\left[\left(\frac{V_0}{V}\right)^{\frac{2}{3}} - 1\right]\right] \tag{2.24}$$

where V$_0$ is the reference volume at zero pressure, V is the deformed volume, B$_0$ is the bulk modulus and B$_0'$ its derivative with respect to the pressure. With the use of the thermodynamic relation between internal energy E, volume V and pressure P

$$P = -\left(\frac{\partial E}{\partial V}\right)_{S,N_i} \tag{2.25}$$

and via integration, it is possible to calculate the internal energy as a function of the volume from equation 2.24. This output, the Birch-Murnaghan EOS 2.26 was used to fit the energy-volume curves in this thesis, calculated during bulk analysis. [31, 32]

$$E\left(V\right) = E_0 + \frac{9V_0B_0}{16}\left[\left[\left(\frac{V_0}{V}\right)^{\frac{2}{3}} - 1\right]^3 B_0' + \left[\left(\frac{V_0}{V}\right)^{\frac{2}{3}} - 1\right]^2\left[6 - 4\left(\frac{V_0}{V}\right)^{\frac{2}{3}}\right]\right] \tag{2.26}$$

2.5 Zirconia ZrO_2

Zirconia is one of the most studied and very well understood ceramic materials. The band gap is phase dependent and is approximately 4-6 eV [33–36], making ZrO_2 a good thermal- and electrical insulator.
In its solid state of aggregation, Zirconia has three temperature dependent phase transitions. The most stable phase of ZrO_2 at ambient pressure and low temperature is the monoclinic (m)- or α-phase, which crystallizes in the Baddeleyite structure (space group P2_1/c, no. 14). At a temperature of 1478K the monoclinic changes to a tetragonal (t) structure (space group P4_2/nmc, no. 137) and at 2650K the cubic (c)- or γ-phase becomes thermodynamically more stable. The cubic phase crystallizes in the calcium fluoride structure (space group Fm$\bar{3}$m, no. 225). The melting point of Zirconia is located at 2983K [37].
The c-phase structure is an fcc lattice of zirconium atoms with oxygen atoms at the tetrahedral sites. Due to this structure the zirconium atoms are eightfold coordinated and the oxygen atoms are fourfold coordinated. The cubic unit cell is fully specified by a single lattice constant a. Alternatively, the cubic unit cell can be derived from the tetragonal phase by placing the oxygen atoms at the same height, 0.25c and 0.75c, and a c/a ratio of $\sqrt{2}$. The advantage of using this bcc cell instead of the fcc cell is that one needs fewer formula units to describe the structure (fcc four f.u., bcc two f.u.), which leads directly to a shorter calculation time.
Vice versa the t-phase can be derived by displacing the oxygen atoms from the c-phase along the c axis. The t-phase is characterized by two lattice constants a=b and c and the displacement $d_z = \Delta z/c$ of the oxygen atoms with respect to the c-phase. In the t- and c-phase all angles are 90°.
If the t-phase gets further distorted, the m-phase evolves. One needs three independent lattice parameters, one angle unequal 90° and the positions of the Zr- and O-atoms to describe this phase - on the whole 13 parameters. In addition there are little symmetries in this phase, the Zr-atoms are only sevenfold and the O-atoms are three- or fourfold coordinated.
A summary of these informations can be found in table 2.1.

			Coordination		
Phase	**Space group**	**T** [K]	**Zr**	**O$_1$**	**O$_2$**
Cubic	Fm$\bar{3}$m - no. 225	2650 - 2983	8	4	4
Tetragonal	P4_2/nmc - no. 137	1478 - 2650	8	4	4
Monoclinic	P2_1/c - no. 14	$<$1478	7	3	4

Table 2.1: Summarized information about ZrO_2 phase structures [37].

In addition these crystal structures are shown in figures 2.1, 2.2 and 2.3. The optimized lattice parameters obtained with different functionals, which are used for further calculations in this thesis can be found in table 2.2 [38].

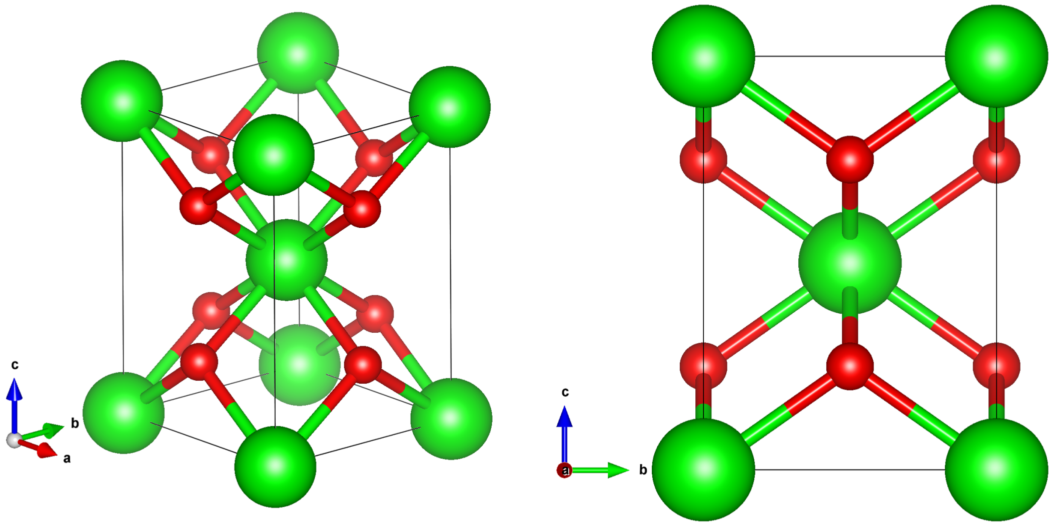

Figure 2.1: Cubic (bcc) unit cell of ZrO_2 made out of the tetragonal unit cell with a c/a-ratio of $\sqrt{2}$. All oxygen atoms are placed at 0.25c or 0.75c. (Zr=green, O=red)

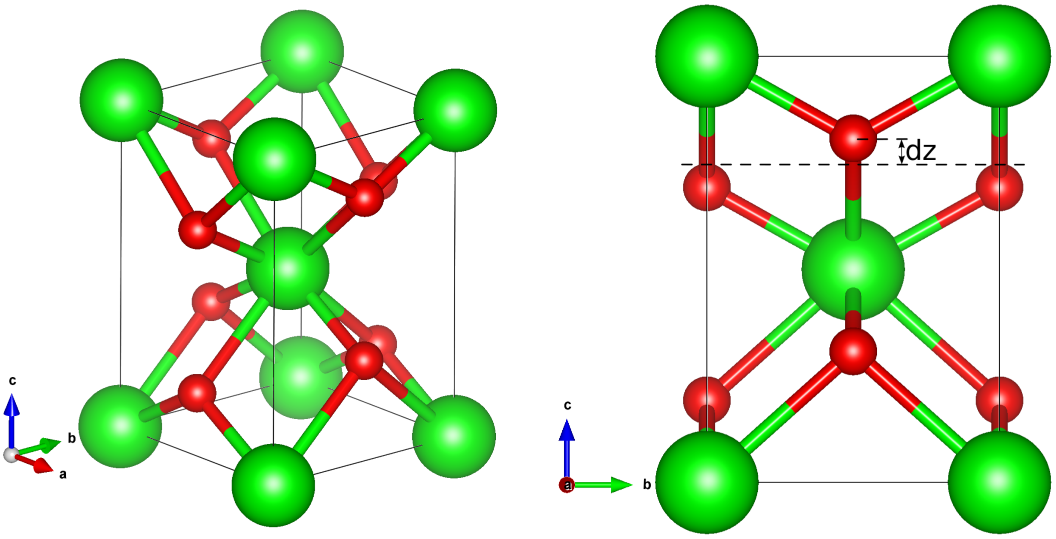

Figure 2.2: Tetragonal unit cell of ZrO_2 with marked parameter d_z, which gives the oxygen displacement referring to the position in the cubic unit cell. (Zr=green, O=red)

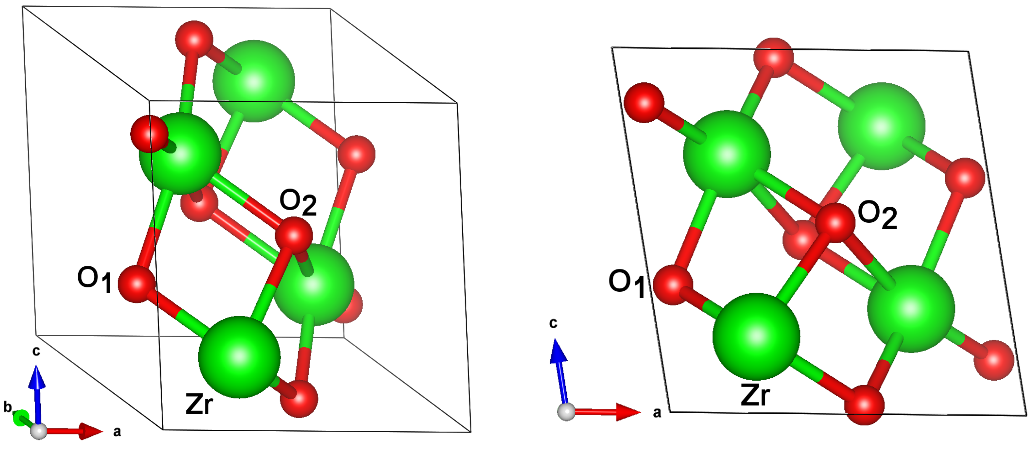

Figure 2.3: Monoclinic unit cell of ZrO_2 with important oxygen and zirconium labelled for determination of bond lengths and angles. (Zr=green, O=red)

	GrimmeD3	**optB86b**	**PBE**	**SCAN**	**exp.** [39–41]
Cubic					
ΔH / f.u. [eV]	-10.107	-10.619	-10.211	-11.670	
Volume / f.u. [Å^3]	33.16	33.25	33.76	33.05	32.89
a=b=c [Å]	5.10	5.10	5.13	5.09	5.09
Tetragonal					
ΔH / f.u. [eV]	-10.221	-11.060	-10.314	-11.756	
Volume / f.u. [Å^3]	34.08	34.11	34.77	33.95	33.67
a=b [Å]	3.58	3.61	3.63	3.60	3.61
c [Å]	5.31	5.23	5.29	5.23	5.18
d$_z$	0.055	0.051	0.057	0.054	0.057
Monoclinic					
ΔH / f.u. [eV]	-10.618	-11.132	-10.423	-11.827	-11.374
Volume / f.u. [Å^3]	35.42	35.39	36.15	35.34	35.22
a [Å]	5.15	5.14	5.19	5.15	5.15
b [Å]	5.23	5.25	5.25	5.22	5.21
c [Å]	5.33	5.31	5.38	5.33	5.32
β	99.4	99.2	99.6	99.3	99.2
x$_{Zr}$	0.277	0.277	0.276	0.276	0.275
y$_{Zr}$	0.043	0.042	0.044	0.042	0.040
z$_{Zr}$	0.210	0.210	0.210	0.210	0.208
x$_{O_1}$	0.069	0.074	0.065	0.067	0.070
y$_{O_1}$	0.334	0.342	0.327	0.330	0.332
z$_{O_1}$	0.343	0.335	0.350	0.348	0.345
x$_{O_2}$	0.449	0.447	0.451	0.450	0.450
y$_{O_2}$	0.758	0.758	0.757	0.757	0.757
z$_{O_2}$	0.478	0.480	0.475	0.477	0.479

Table 2.2: Calculated lattice parameters for ZrO_2 bulk-phases and different functionals used in comparison to experimental values. X-, y- and z-coordinates are dimensionless with respect to the unit cell lattice parameters a,b and c. The heat of formation is given per formula unit of ZrO_2 with respect to hcp-Zr and O_2 molecules.

For $_{40}$Zr also lots of isotopes exist, where the main stable ones with their abundance are ^{90}Zr (50.45%), ^{91}Zr (11.22%), ^{92}Zr (17.15%) and ^{94}Zr (17.38%). For all calculations, the default value of 91.224u from the potential file was used.

2.6 Yttria Y_2O_3

Yttria Y_2O_3 is one of the most important sesquioxides in the general class of ceramics, with a melting point located at 1800K and an electronic band gap of about 4-6eV [42], which is comparable to that of zirconia, making Y_2O_3 also a good thermal and electrical insulator. Yttrium (atomic number 39) itself is neighboring zirconium (atomic number 40) in the periodic table of the elements. Concerning the electronic configuration, both elements have a partially filled d-shell, in particular Y → $[Kr]4d^1 5s^2$, Zr → $[Kr]4d^2 5s^2$, which is common for transition metals. In its solid state at ambient pressure, Yttria appears in a cubic-like crystal structure (space group $Ia\bar{3}$, no. 206) with a lattice parameter of a = 10.6Å [43]. One can imagine an fcc lattice of yttrium atoms with oxygen atoms at the tetrahedral sites, but with some oxygen atoms missing and being replaced by vacancies. Due to the oxidation state of yttrium Y^{3+}, this configuration leads to sixfold coordinated yttrium atoms and fourfold coordinated oxygen atoms. Figure 2.4 shows the Y_2O_3 unit cell doubled in the b direction.

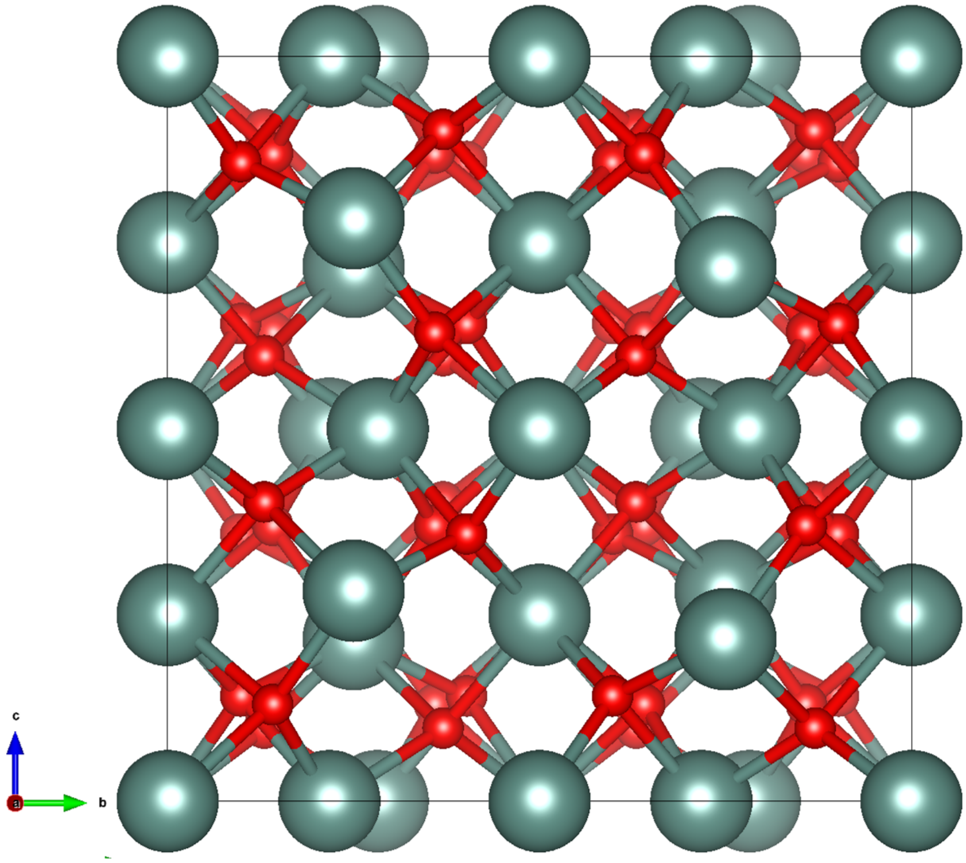

Figure 2.4: Unit cell of Y_2O_3. One can clearly recognize the different order of Y-rows. (Y=gray, O=red)

One can clearly recognize, that two different symmetry-sites for yttrium exist in this configuration. On the one hand, there are rows aligned at the same height, with respect to the orientation shown in the figure, and on the other hand, two yttrium atoms could be shifted against each other in one crystallographic direction. Just the yttrium atoms with coordinates [0(+0.5) ; 0(+0.5) ; 0(+0.5)] stay at their ideal positions, referring to their symmetric fcc positions, every other yttrium atom got shifted, resulting in the structure seen above. For each functional these yttrium atoms are shifted approximately 0.34 Å. In total this unit cell contains Y_1 at the 8a site, Y_2 at the 24d site and one O at the 48e site. In total there are 80 atoms in this unit cell of Y_2O_3. The optimized lattice parameters, obtained with different functionals and which are used for further calculations, can be found in table 2.3.

	GrimmeD3	**optB86b**	**PBE**	**SCAN**	**exp.** [42–44]
Cubic					
ΔH / f.u. [eV]	-18.545	-19.247	-18.132	-20.340	-20.032
Volume / f.u. [Å^3]	73.43	73.49	74.05	73.91	74.44
a [Å]	10.55	10.55	10.58	10.57	10.60
x_{Y_1}	0.000	0.000	0.000	0.000	0.000
y_{Y_1}	0.000	0.000	0.000	0.000	0.000
z_{Y_1}	0.000	0.000	0.000	0.000	0.000
x_{Y_2}	0.282	0.283	0.282	0.283	0.282
y_{Y_2}	0.000	0.000	0.000	0.000	0.000
z_{Y_2}	0.250	0.250	0.250	0.250	0.250
x_O	0.098	0.098	0.098	0.098	0.098
y_O	0.359	0.356	0.359	0.359	0.359
z_O	0.130	0.130	0.130	0.130	0.133
Y_1-O bonds [Å]	2.27	2.27	2.28	2.28	2.26
Y_2-O bonds [Å]	2.23	2.23	2.24	2.24	2.25
	2.26	2.26	2.26	2.26	2.28
	2.33	2.33	2.33	2.33	2.34

Table 2.3: Calculated lattice parameters for Y_2O_3 solid state phase and different functionals used in comparison to experimental values. X-, y- and z-coordinates are dimensionless with respect to the unit cell lattice parameter a. The heat of formation is given per Y_2O_3 formula unit with respect to hcp-Y and O_2 molecules.

Concerning this structure, there are six equal Y_1-O bonds of approximately 2.27Å and three pairs of Y_2-O bonds of 2.23Å, 2.26Å and 2.33Å, nearly independent of the used functional. Ishizawa et al. [45] found an approximately Y-O distance of 2.28, which is in good agreement with the results shown above. So each oxygen atom is bound to one Y_1 and three Y_2 atoms in the form of a distorted tetrahedron [42].
This average Y_i-O (i=1,2) distances are approximately 2% larger compared to the average Zr-O bond length in c-ZrO_2. Hence, the lattice parameter a is also 3% larger than in c-ZrO_2.

2.7 Yttria-Substituted-Zirconia YSZ

2.7.1 The Ion Conductivity of YSZ

If one combines ZrO_2 and Y_2O_3 to form YSZ, some of the smaller Zr^{4+}-atoms (ionic radius of 0.84Å) in the c-ZrO_2 lattice get replaced by the slightly larger Y^{3+}-atoms (ionic radius of 1.02Å) [46, 47] and for the sake of charge neutrality, one oxygen vacancy is generated for each pair of Y-atoms on the crystal lattice. In order to describe this replacement of Zr by Y, one can use the Kröger-Vink notation for lattice elements and defects in crystal structures:

$$Y_2O_3 \longrightarrow 2\,Y'_{Zr} + 3\,O_O^{\times} + V_O^{\bullet\bullet} \tag{2.27}$$

Therefore the amount of oxygen vacancies in the anionic sublattice can be received from the amount of Y ions placed in the cationic one. In contrast the concentration of thermally induced intrinsic defects is negligible, which is an explanation for the low ion conductivity of pure zirconia. The ion conductivity itself not only depends on the total amount of vacancies, but also on the size of the acceptors and the mobility of the oxygen vacancies $V_O^{\bullet\bullet}$ on the sublattice as along grain boundaries (in commonly used polycrystalline materials). These vacancies are usually mobile at high temperatures, which leads to an increase of the ion conductivity. It is also established that the oxide ions carry approximately 99% of the current in YSZ which is a reason why YSZ is used for SOFCs. One can now naively assume that the ion conductivity would increase linearly with the amount of Y-atoms and thereby created oxygen vacancies under the assumption of a constant mobility of the charge carriers, but this would hypothesize that Y_2O_3 should be one of the best ion conductors? Well, on the one hand these vacancies experience the attraction from the acceptor Y, but on the other hand they get repulsed by other positively charged carriers such us other oxygen vacancies. With higher Y-concentration, Y_2O_3 will form complexes and thereby can form clusters in which the oxygen vacancies are bonded to two cations, thus also leading to a decrease in the oxygen vacancy mobility [48]. Nevertheless, for YSZ the ion conductivity exhibits a maximum (in the range of 0.10 - 0.16Scm^{-1} at 1000°C) at 8-9mol% of Y_2O_3 doped to c-ZrO_2 and finally decreases with higher amount of Y_2O_3 [49–51]. For brevity, x mol% Y_2O_3 doped to cubic ZrO_2 are given as xYSZ. At last, the ion mobility is limited by the size and radius of the acceptors with respect to the host lattice, by the affinity of the dopant to form clusters and of course by the microstructure of the compound (grain boundaries, pores, cracks,...). The early studies of ion conductivity in the 1960s and 1970s found the maximum at 8-9mol% YSZ, predicting the structure as cubic, but it has turned out during longtherm stability experiments, that the ion conductivity of 8-9mol% YSZ decreases significantly during the first thousand operating hours of about 1000 °C [52–54] as can be seen in figure 2.5. There are lots of explanations for this effect of degradation of the bulk ion conductivity, but one can imagine, that this effect occurs due to the decrease of charge carriers and due to blocking of these carriers resulting in the decrease of their mobility. One explanation is, that the amount of 8mol% Y_2O_3 doped to c-ZrO_2 does not fully stabilize the cubic phase and with further aging and thermal exposure it decomposes into tetragonal- and cubic-rich regions of YSZ. This emerging tetragonal phase blocks the ion mobility due to different oxygen bond lengths and resulting barriers compared to pure c-ZrO_2 [55–57], but more about this topic is in the section about phases of YSZ. Another explanation was given by Kondoh et al. [52, 53, 54], where they found local clustering of oxygen vacancies during the heat treatment of YSZ. Such clustering would trap vacancies and would also result in the decrease of ion mobility, which would finally lead to a decrease of ion conductivity. So the impurity and defect segregation as well as grain boundaries play an important role in ion conductivity.

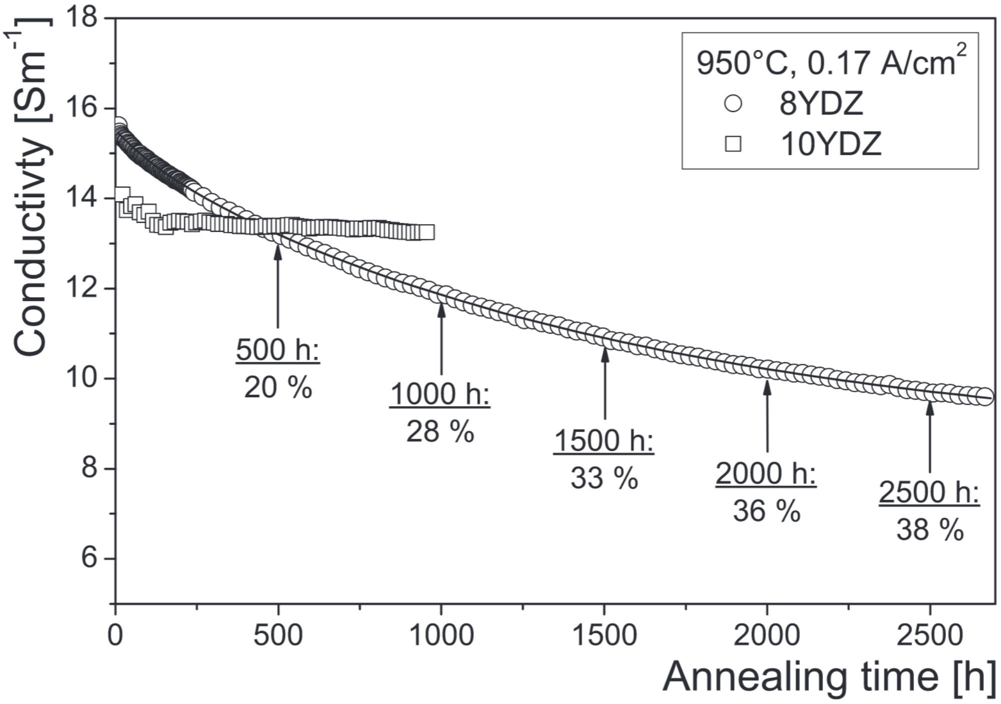

Figure 2.5: Ion conductivity of 8 mol% and 10 mol% Y_2O_3 substituted ZrO_2 at 950 °C as a function of time, taken from BUTZ et al. [56].

2.7.2 The Phases of YSZ

Especially the ZrO_2-Y_2O_3 system has been investigated for decades, delivering many different phase diagrams for this system, some more similar than others. Thus it has been naturalized to use the name 'Yttria-Stabilized-Zirconia' for 8mol% Y_2O_3 doped c-ZrO_2, because during early studies it was stated that this amount fully stabilizes the cubic phase at room temperature. As mentioned in the previous paragraph, this is not truly right. Long-term-studies showed, that the effect of keeping YSZ at 1000°C for several thousand hours results in the transformation to cubic and tetragonal regions inside the crystal [55–57].

One of the first phase diagrams showing the total range of ZrO_2-Y_2O_3 concentration was published by Scott [58], who studied the metastable and equilibrium phase

relationships by X-ray diffraction and stated their crystals structures with concentrations of more than 7mol% Y_2O_3 as cubic. For concentrations below this threshold they observed the coexistence of c-YSZ and metastable t′-YSZ. Since the decomposition of the pure cubic phase into the cubic and tetragonal phase is strongly limited by the mobility of the ions, one can use rapid cooling or quenching from high temperatures to prohibit diffusion-controlled reactions and phase transformations. Nevertheless, cubic YSZ diffusionlessly transforms into the metastable tetragonal t′ form of YSZ. Whereas pure tetragonal YSZ shows independent lattice parameters for different Y_2O_3 content, the t′-phase is defined by lattice parameters which depend on the amount of Y_2O_3. In this dopant range of about 2-6mol%, the lattice parameter $c_{t'}$ decreases while $\sqrt{2}\cdot a_{t'}$ increases with increasing amount of Y_2O_3. Both of these values converge asymptotically to the cubic lattice parameter at approximately 8.5mol%, hence the tetragonality $c_{t'}/(\sqrt{2}\cdot a_{t'})$ also converges [59–63]. In addition Zhou et al. [63] observed a second metastable tetragonal t″-phase in 8 mol%-doped ZrO_2 with tetragonality $c_{t''}/(\sqrt{2}\cdot a_{t''})\approx 1$, described as cubic-like.
STUBICAN et al. [64] proved the existence of the hexagonal $Zr_3Y_4O_{12}$ δ-phase (space group R$\bar{3}$, no. 148) at amounts higher than 40 mol% Y_2O_3 in their phase diagram, which is isostructural to UY_6O_{12}. Such a similar phase (space group R3m, no. 160) was also predicted for pure ZrO_2 by Wei et al. [65], using USPEX [66–68] and VASP. YASHIMA [69] took a closer look at the metastable phase diagram of the ZrO_2-Y_2O_3 system up to 16mol% Y_2O_3. Besides, they plotted a summary of YSZ phase diagrams found so far and showed the discrepancy in the results, especially at temperatures around 1000°C. They claimed, that this divergence is attributable to a variety of metastable states and to the difficulty in experiments. After this investigation, they found out, that it is difficult to maintain thermal equilibrium below 1000°C and one has to consider diffusional and cation-diffusionless phase transformations. This yields to the assumption, that for 8mol% Y_2O_3 a very slow decomposition into the tetragonal and cubic, monoclinic and cubic and even the metastable t′ and t″ phases are possible. Suzuki [70] investigated the phase transition $c + t \rightarrow t$ via conductance measurements for the 2.4-6mol% Y_2O_3 regime and found a relation between the transition temperature and the Y_2O_3 content for exactly this regime. Fabrichnaya et al. [71] reported a theoretical study and resulting phase diagram for the ZrO_2 rich part in 2005, where they claimed, that the cubic polymorph would not decompose at all upon lowering the temperature. A short summary of some phase diagrams mentioned above can be seen in figure 2.6.
Therefore the minimum amount of Y_2O_3 doped to ZrO_2 to stabilize the cubic phase is of major interest for high-temperature fuel-cell applications. As mentioned above, there is a big discrepancy in the published values, which range from 5 mol% to 9.2 mol% Y_2O_3 [72, 73], to reach this aim. In summary, it is known that 8.5 mol% YSZ is not completely stabilized at room temperature in its pure cubic phase and a tetragonal-type phase occurs during heat treating around 1000 °C for several thousands of hours [57]. Every occuring tetragonal t-, t′- and t″-phase can be described by a cubic ZrO_2 lattice with a distorted anionic sublattice, as can be seen in the section about ZrO_2, figure 2.2. To antagonize the confusion about mol% Y_2O_3, mol% $YO_{1.5}$, at% including and excluding oxygen atoms, one can find a conversion table in the appendix 6.

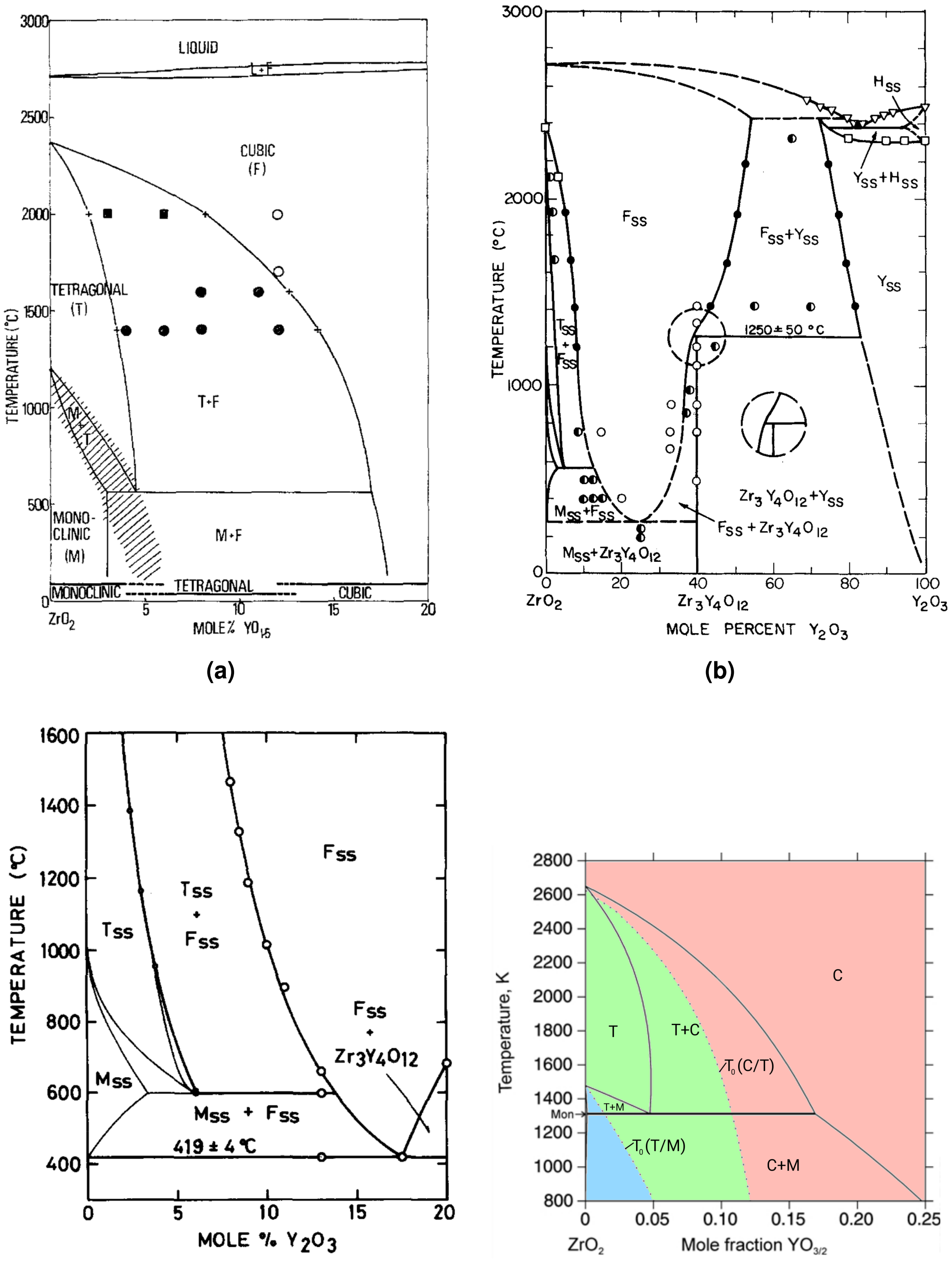

(a)

(b)

(c)

(d)

Figure 2.6: Phase diagrams for YSZ obtained via different methods, (a) by Scott [58] via XRD, (b) by STUBICAN et al. [64] via XRF and XRD, (c) by Suzuki [70] via electrical conductance measurements and (d) theoretically by Fabrichnaya and Aldinger [74]. One can also recognize the $Zr_3Y_4O_{12}$ R$\bar{3}$ phase in (b) and the rather small monoclinic region below 3 mol% in nearly every diagram. The metastable tetragonal t′ ($c_{t'}/a_{t'} > 1$) and t″ ($c_{t''}/a_{t''} \approx 1$) phases would be located at room temperature with concentrations ranging from 3 mol% to 8 mol% and 8 mol% to 10 mol%.

2.8 Convergence - K-Point Grid and Energy Cut-Off

The initial structures for each phase of Y_2O_3, ZrO_2 were built using VESTA [75], a 3D visualisation program for electronic and structural analysis. The initial parameters were taken from Mayr-Schmölzer [76], Curtis [43] and Xu et al. [42].

During simulations done by VASP and presumably every other density functional theory code, convergence plays a very important role, so it is essential to do convergence studies concerning the cut-off-energy and used k-point mesh. The cut-off-energy is relevant for the number of plane waves used in the basis set. All plane waves with a kinetic energy smaller than this energy are included. A higher cut-off-energy leads to more accurate simulations, but the calculation time also increases. Due to this fact one has to find a good compromise between accuracy and calculation time. For each phase of ZrO_2, Y_2O_3 and YSZ the cut-off-energy scan ranged from 100 to 800eV in steps of 25eV with a 6x6x6 Gamma-centered grid. For each of the phases and structures, a cut-off-energy of 425eV, in comparison to 800eV, is enough to get nice values with the advantage of faster calculations.

In addition, a k-point-scan was done using the previously calculated cut-off-energy of 425eV. The scan ranged from 2x2x2 to 15x15x15 k-points with a step size of 1 in each direction. In comparison to 15 k-points per direction, the energy difference to a smaller grid is in the region of meV and below. Therefore it is adequate to use such a grid for further calculations. Summarized, a cut-off-energy of 425eV, a k-point grid of 6x6x6 for the bulk ZrO_2 and Y_2O_3 phases, a grid of 2x2x2 for the different YSZ bulk configurations, a grid of 4x4x1 for Y_2O_3 and ZrO_2 surfaces and a grid of 2x2x1 k-points for YSZ surfaces was used for the calculations in this thesis. For each surface calculation, the atoms of the lowest trilayer or the atoms in the lowest oxygen and transition metal layer were kept at their positions to simulate the bulk environment.

3 Results and Discussion I

3.1 YSZ Bulk Properties

3.1.1 Lattice Parameter and Enthalpy of Formation

The starting point for all YSZ simulations is the prerelaxed c-ZrO_2 structure, mentioned in section 2.5, table 2.2. Due to doping with Y_2O_3 it is not necessary to use the simplified bcc structure, therefore the common fcc structure obtained via PBE functional is used. This relaxed structure with the ideal atomic positions is then used with the ATAT-MCSQS code to generate 2x2x2 supercells of YSZ with the desired amount of Y_2O_3. Such a supercell of pure c-ZrO_2 contains 96 atoms (32 formula units f.u. of ZrO_2). With each substituted Zr-pair for an Y-pair, one oxygen atom has to be removed to create an oxygen vacancy and keep charge neutrality, stated as one defect cluster of Yttrium-Vacancy-Yttrium (Y-V-Y). Doping amounts (in mol% Y_2O_3) of 3.2, 6.7, 10.3, 14.3 and 33.3 are used for bulk simulation, corresponding to 2, 4, 6, 8 and 16 Y-atoms in this supercell.
For the simplest case of 3.2 mol% Y_2O_3 substituted c-ZrO_2 (3YSZ) with just two yttrium atoms and one oxygen vacancy in the structure, eight different arrangements are investigated. With respect to the phase diagrams mentioned in section 2.7.2, the tetragonal phase should be most stable within this amount of Y_2O_3, as well as for 6.7 mol% Y_2O_3 substituted c-ZrO_2 (7YSZ). For higher amounts of doping, especially 10YSZ, 14YSZ and 33YSZ, the cubic phase should be most stable.

The calculated lattice parameters can be found in table 3.1. The slight differences to 90° in the lattice angles α, β and γ originate from the fact, that the relaxations are done allowing VASP to relax the ionic positions and to change the shape of the unit cell at a specific volume. Therefore 3YSZ and 7YSZ are stated as tetragonal stabilized ZrO_2 with a tetragonality of $c_{3YSZ}/a_{3YSZ} = 1.02$ and $c_{7YSZ}/a_{7YSZ} = 1.01$. One can clearly see, that PBE overestimates the lattice parameters for each amount of doping, in comparison to SCAN. In 3YSZ the short sides are 0.8% and the long side is 1.6% off the experimental values. For SCAN the parameters fit the experimental results quite well with an error of 0.5% for the long axis. For 7YSZ PBE overestimates the parameters by approximately 0.9-1.4%, the error for SCAN is in the range of -0.2-0.5%. In 10YSZ, stated as cubic, the average error for PBE lattice parameters is 1.2% and for SCAN just 0.4%. PBE again overestimates the parameters in the range of 0.9-1.3% for 14YSZ, SCAN fits well to the experimental results by an error of 0.1-0.4%. In the case of 33YSZ the parameters tend to go off-cubic with an error of 0.4-1.1% with PBE and -0.4-0.2% with SCAN. This result may arise due to the close R$\bar{3}$ $Zr_3Y_4O_{12}$ phase occuring in the area of 40 mol% Y_2O_3.

3YSZ	**ΔH** / f.u. [eV]	**a** [Å]	**b** [Å]	**c** [Å]	α[°]	β[°]	γ[°]
PBE	-0.075	10.29	10.29	10.52	90.0	90.0	89.9
SCAN	-0.060	10.21	10.21	10.40	90.0	90.0	89.9
exp. [77]		10.21	10.21	10.35	90.0	90.0	90.0

7YSZ	**ΔH** / f.u. [eV]	**a** [Å]	**b** [Å]	**c** [Å]	α[°]	β[°]	γ[°]
PBE	-0.062	10.37	10.35	10.45	90.5	90.5	90.1
SCAN	-0.045	10.31	10.24	10.31	90.0	90.3	90.0
exp. [77]		10.26	10.26	10.31	90.	90.	90.

10YSZ	**ΔH** / f.u. [eV]	**a** [Å]	**b** [Å]	**c** [Å]	α[°]	β[°]	γ[°]
PBE	-0.052	10.41	10.40	10.44	89.9	90.2	90.1
SCAN	-0.028	10.33	10.35	10.31	90.8	90.4	89.9
exp. [77, 78]		10.29	10.29	10.29	90.0	90.0	90.0

14YSZ	**ΔH** / f.u. [eV]	**a** [Å]	**b** [Å]	**c** [Å]	α[°]	β[°]	γ[°]
PBE	-0.060	10.40	10.39	10.44	91.0	90.2	90.3
SCAN	-0.032	10.32	10.34	10.35	90.0	89.0	89.5
exp. [78]		10.31	10.31	10.31	90.0	90.0	90.0

33YSZ	**ΔH** / f.u. [eV]	**a** [Å]	**b** [Å]	**c** [Å]	α[°]	β[°]	γ[°]
PBE	-0.029	10.47	10.51	10.54	90.5	89.7	90.0
SCAN	-0.014	10.39	10.42	10.45	90.2	89.8	89.9
exp. [78]		10.43	10.43	10.43	90.0	90.0	90.0

Table 3.1: Calculated lattice parameters of YSZ for different amounts of mol% Y_2O_3. PBE and SCAN functionals were used and compared to experimental results obtained via Rietveld refinement method [77, 78]. The heat of formation, with respect to cubic ZrO_2 and Y_2O_3, is given per ZrO_2 formula unit for an undoped 2x2x2 bulk like structure with 32 formula units in it.

In total, SCAN predicts smaller dimensions for the unit cell of each arrangement, in comparison to PBE, which clearly overestimates the lattice parameters. Compared to their ideal fcc positions of c-ZrO_2, some zirconium atoms are slightly shifted in one symmetry-related direction by 0.14 Å to 0.20 Å, which is in good agreement with Ishizawa et al. [45] and [79], denoting it as the Zr-shift model. This displacements are similar to c-Y_2O_3, which also forms shifted anion rows.

Figure 3.1 shows the behavior of the lattice parameters and the tetragonality described in section 2.7.2 with increasing amount of Y_2O_3 doped to c-ZrO_2.

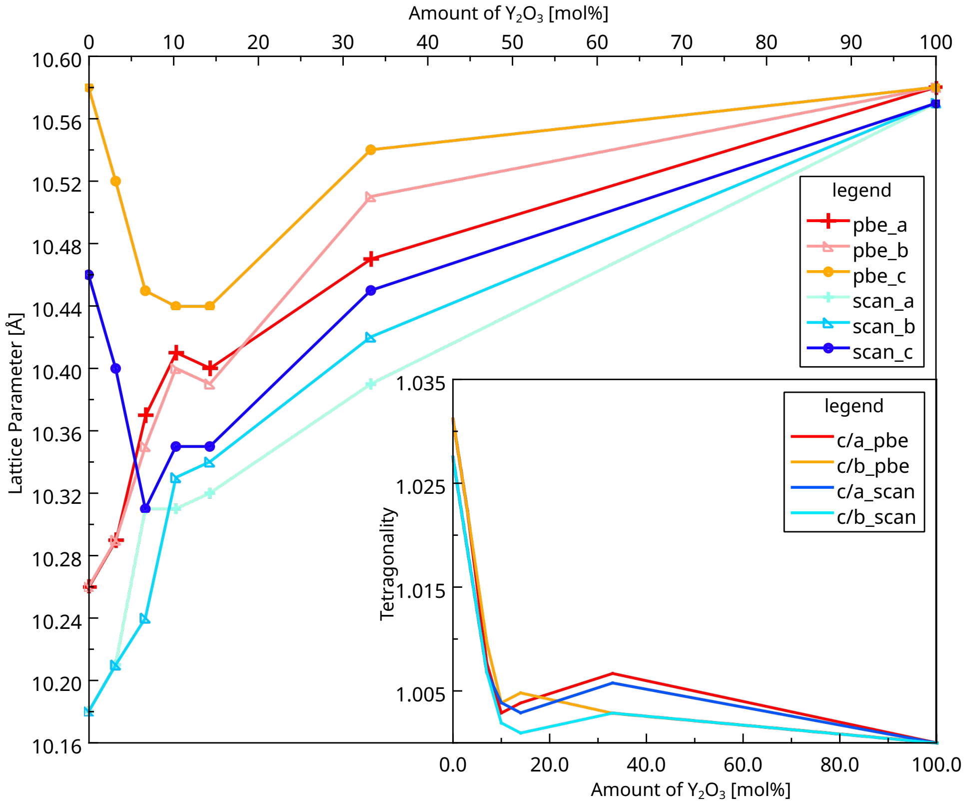

Figure 3.1: Behavior of the lattice parameters a,b and c for different amounts of Y_2O_3 and different functionals used. The subplot shows the tetragonality for both functionals.

So 3YSZ and 7YSZ were stated as tetragonal, whereas structures for higher amounts of doping were stated as quasi cubic. For a perfect cubic lattice, a,b and c should be of the same length. The error for 10YSZ and 14YSZ is approximately 0.4%. As mentioned in section 2.7.1, yttrium atoms are slightly larger than zirconium atoms and with a higher amount of doping, a higher concentration of larger yttrium atoms is present, which also increases the total cell volume. The expansion in the low doping regime between 0 and 10 mol% first leads to a phase transition from the tetragonal to the cubic phase [80, 81]. Afterwards each parameter increases nearly linear, so the structure stays cubic. This enlargement culminates in a phase transition from cubic to the hexagonal $Zr_3Y_4O_{12}$ δ-phase with space group R$\bar{3}$ above 33 mol%, till at last the pure cubic Y_2O_3 phase gets energetically most stable at the Y_2O_3 rich side of the diagram. One can also recognize that the PBE functional leads to larger lattice parameters than SCAN, which fits the experimental values much better.

As mentioned above, different configurations for each amount of doping are used. For 3YSZ different arrangements of Y-V-Y are investigated to find the best configuration for the defect cluster. Coming from the perfect c-ZrO_2 structure, the different lengths for the cationic lattice of the unit cell are shown in figure 3.2. One now has to imagine a 2x2x2 supercell, so this figure shows all possible positions for two yttrium atoms in such a supercell, due to symmetry and because the periodic boundary conditions limit the amount of different configurations.

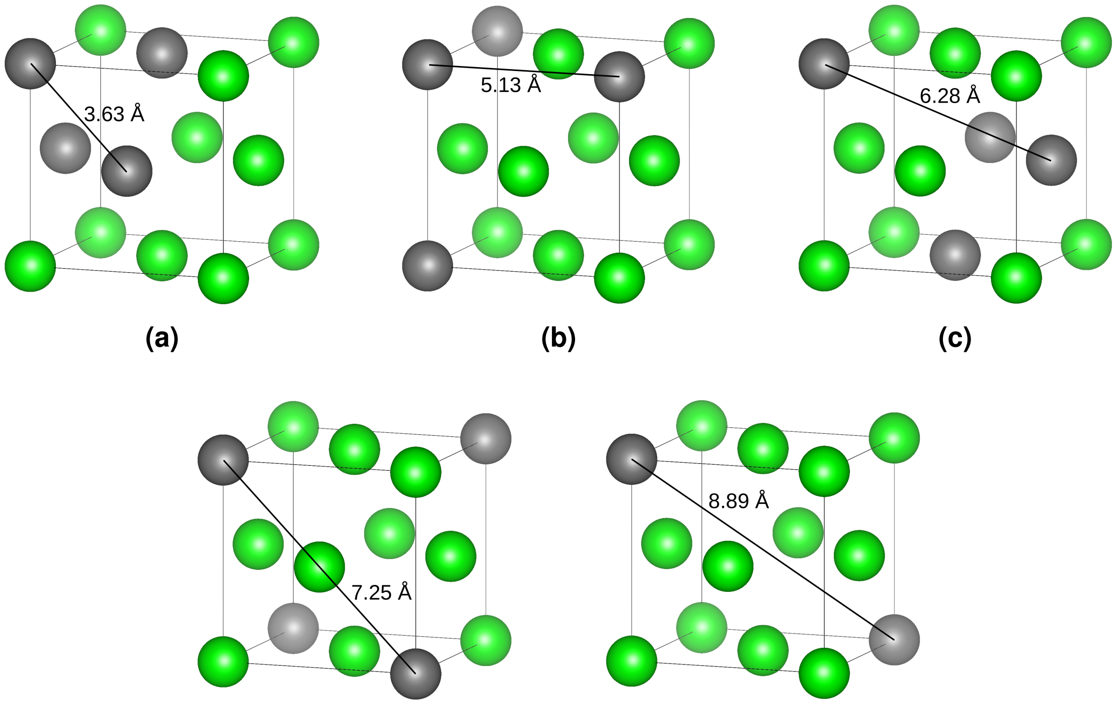

(a) **(b)** **(c)** **(d)** **(e)**

Figure 3.2: Visualization of the cationic fcc lattice of c-ZrO_2 and averaged distances for the possible arrangements of two yttrium atoms. In each subfigure, the gray atoms have the same distance from the atom in the left upper corner.

The results, including the heat of formation, Y-Y distances and oxygen vacancy positions are given in table 3.2. Negative values represent favorable arrangements, whereas arrangement 3 is the most unlikely to form, with respect to the investigated configurations. The explanation why arrangements 1.1 and 2 lead to the same heat of formation is comparatively simple. While in both arrangements the Y atoms are placed in nearest neighboring (nn) positions (about 3.63 Å), in arrangement 1.1 the oxygen vacancy is placed next nearest neighbor (nnn, distance of 4.25 Å to both Y atoms) and in arrangement 2 it is placed nearest neighbor (nn, distance of 2.22 Å to both Y atoms). Starting from an ideal cubic ZrO_2 lattice, the oxygen vacancy in arrangement 2 shifts to the nnn position very fast during early ionic relaxation steps. This leads to the assumption, that there is no barrier for the oxygen atom going from the nnn to the nn position when starting from a perfectly symmetric cubic lattice. This explanation is also valid for arrangement 4 with 4.1, but with the difference, that within these arrangements the same behavior also occurs for separated yttrium atoms. Arrangement 2.1 represents the same arrangement as 2, but with the oxygen vacancy kept at the nn position, with respect to the yttrium cluster, via using the selective dynamics tag within VASP and holding the oxygen atom at its initial position. This leads to a difference of 763 meV in the heat of formation.

Arr.	ΔH_{PBE} / f.u. [eV]	ΔH_{SCAN} / f.u. [eV]	Y–Y [Å]	Y_1–V_O [Å]	Y_2–V_O [Å]
1.1	-0.075	-0.060	3.63	4.25	4.25
2	-0.075	-0.060	3.63	$4.25_{2.22}$	$4.25_{2.22}$
7	-0.071	-0.047	5.13	4.25	5.59
4	-0.066	-0.052	6.28	$4.25_{2.22}$	$5.59_{6.66}$
4.1	-0.065	-0.052	6.28	4.25	5.59
6	-0.064	-0.044	6.28	5.59	6.66
1	-0.051	-0.040	3.63	5.59	5.59
2.1	-0.051	-0.033	3.63	2.22_{fix}	2.22_{fix}
5	-0.040	-0.031	6.28	2.22	4.25
3	-0.017	-0.001	8.89	2.22	8.40

Table 3.2: Calculated heat of formation for different arrangements of 3YSZ. The heat of formation is given per ZrO_2 formula unit of an undoped 2x2x2 c-ZrO_2 lattice with 32 formula units inside. The distances between the defect consitutents on the ideal $Fm\bar{3}m$ c-ZrO_2 lattice are given for each arrangement, whereas the subscript numbers denote the starting distances to the vacancy positon, because the oxygen vacancy moved during the relaxation.

Summarized, the most stable alignment for the Y–V_O–Y defect cluster in 3YSZ would be neighboring yttrium atoms (distance of 3.63 Å) and the oxygen vacancy placed nnn (distance of 4.25 Å), followed by nnn yttrium atoms. Arrangement 3 represents the most unstable configuration investigated in this thesis, where the yttrium atoms are placed farthest from each other and the vacancy is placed nn to one yttrium atom.

Table 3.1 shows the energetically most favorable arrangement for each amount of Y_2O_3, but in total many more configurations were tried, each showing the same behavior of yttrium attracting the oxygen atoms and leading to vacancies sitting nnn, if its possible. Especially for lower amounts of doping, this works fine, but reaching higher amounts of doping, one reaches a point, where it is nearly impossible to find a site for the oxygen vacancy, that is not connected to any yttrium atom. For example in 10YSZ it is simple to capture one vacancy inside an yttrium cluster, but the heat of formation denotes this configuration as very unstable and even SCAN delivers a positive heat of formation. This leads to the assumption, that this arrangement of an yttrium cluster with imprisoned oxygen vacancy is very unlikely to form on its own, which was also investigated with 14YSZ and 33YSZ, where the most unstable configurations included oxygen vacancies surrounded by yttrium atoms.

3.1.2 Metastable YSZ Phases

The main idea is to compare the stability of the c-ZrO_2 phase with YSZ by checking the phonon spectra. So first of all a phonon spectra of c-ZrO_2 was calculated using Phonopy [82] and VASP. Due to symmetry, only two atoms have to be displaced in c-ZrO_2. For the calculation of phonons, one needs very accurate forces after the relaxation and therefore the energy and force convergence was set to 10^{-6}, the energy cut-off was raised to 500 eV and the additional VASP tags PREC = A and ADDGRID = .TRUE. were set in the INCAR file. The well converged results are shown in the figures below.

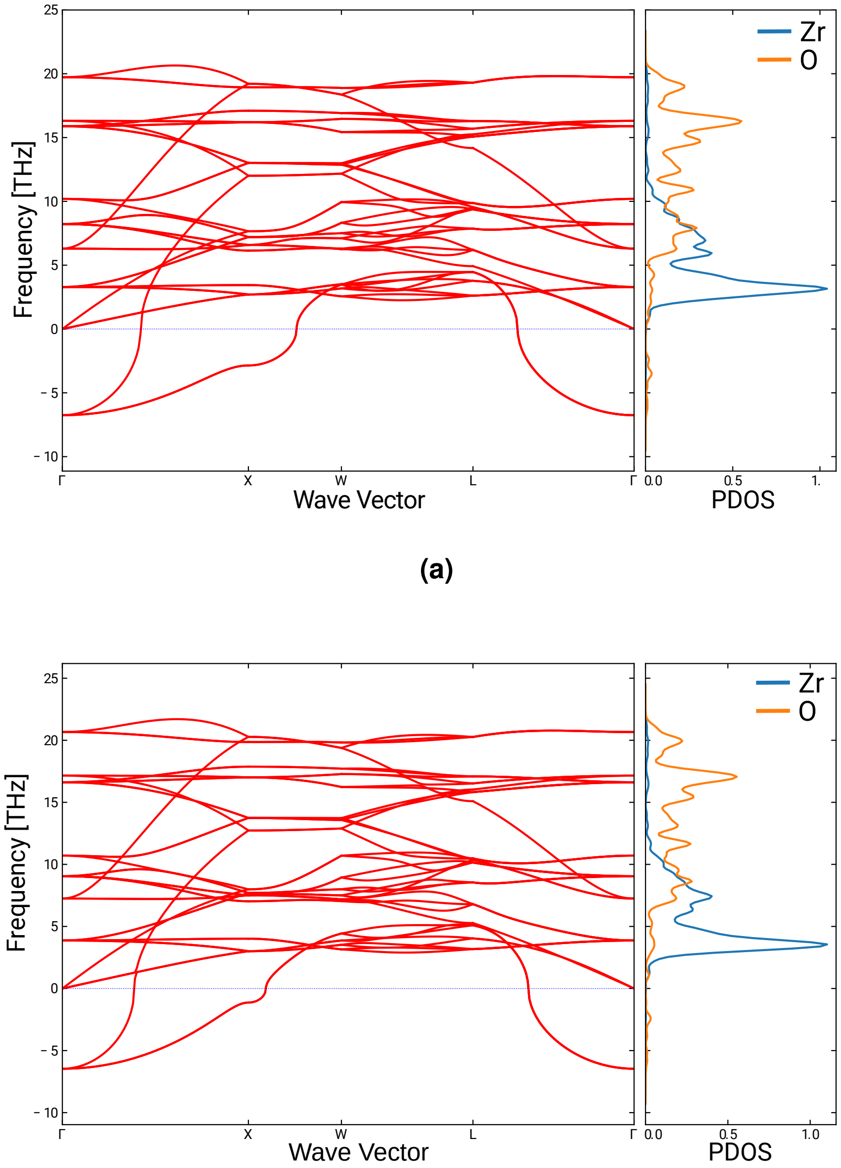

(a)

(b)

Figure 3.3: Phonon spectra for c-ZrO_2 calculated using (a) PBE and (b) SCAN functional.

Figure 3.3 shows the phonon spectra for both functionals used, PBE and SCAN, which are in good agreement with the results of Sternik and Parlinski [83]. The figure also shows the partial phonon density of states (PDOS) on the right hand side of each plot. One can clearly see, that the imaginary modes, which correspond to negative forces, just belong to oxygen atoms marked with the orange line in the PDOS plot. It is now possible to visualize the effect of these forces acting on the ions by a short script provided by Gugler et al. [84].

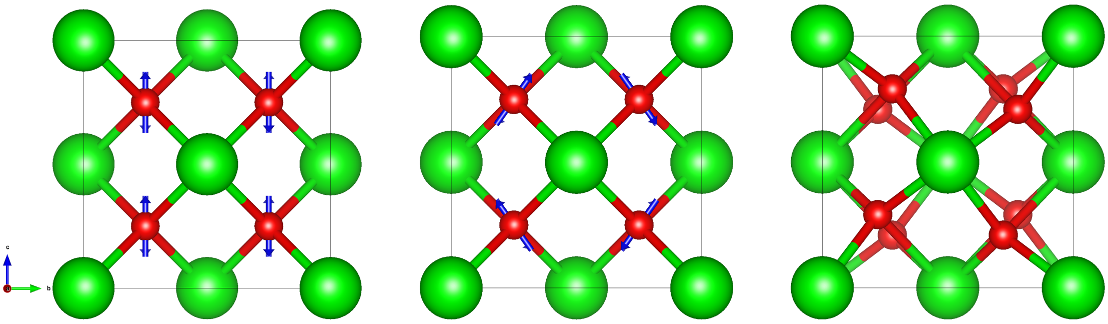

(a) (b) (c)

Figure 3.4: Visualization of the forces which correspond to the first three bands near the gamma point. (a) shows the tetragonal phase transition for band 3, (b) and (c) show the metastable tetragonal-2 structure for band 1 and 2 beneath the gamma point. (Zr=green, O=red)

Figure 3.4 visualizes the forces which correspond to the first three bands beneath the gamma point. Band 1 and 2 deliver a diagonal shift of the oxygen atoms, resulting in the metastable structure seen in (c). Due to symmetry only one of these displacements is shown in the figure above. Band 3 would lead to the common known tetragonal structure with shifted oxygen atoms along the c-axis, shown in section 2.5, figure 2.2. This metastable tetragonal-like phase is energetically located between the cubic and the stable tetragonal ZrO_2 phase, independent of the used functional. Calculating the phonon spectra for this metastable tetragonal-2 phase results in just one imaginary mode, which shifts the diagonal shifted oxygen atoms to their ideal and stable tetragonal ZrO_2 positions.

Doing the volume scans for the different arrangements of 3 mol% Y_2O_3 substituted c-ZrO_2, starting from the cubic $Fm\bar{3}m$ lattice, the energetically most stable final structure is stated as tetragonal like. Compared to a likewise substituted monoclinic structure, the monoclinic one would be the ground state, with an energy difference of approximately 22 meV per atom, using PBE functional. Compared to 7YSZ, a likewise built monoclinic structure would be less stable with an energy difference of 2 meV, stating the tetragonal phase as ground state. But starting from the cubic lattice in 3YSZ also could lead to the metastable tetragonal-2 phase, shown in figure 3.5, and stabilize it in the energetic range of the tetragonal phase.

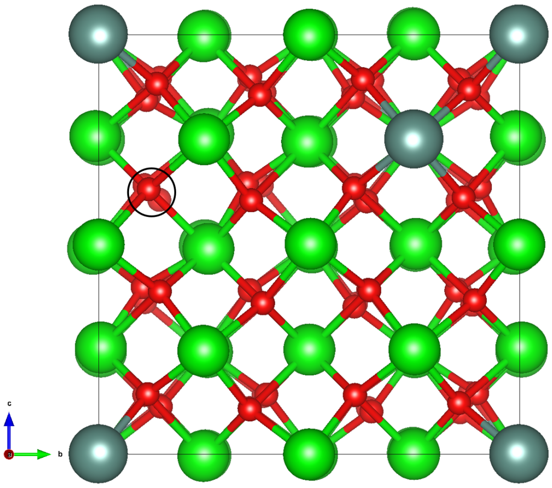

Figure 3.5: One arrangement for 3YSZ in which the metastable tetragonal-2 phase occurs. The black circle marks the oxygen row with the vacancy. (Y=gray, Zr=green, O=red)

This happens for example in arrangements 1 and 5, so what do they have in common? Both structures have the oxygen vacancy placed nnn or farther away from the yttrium atoms, so the vacancy only attracts oxygen atoms connected to zirconium atoms and locally pulling them towards itself. In arrangement 5, the yttrium atoms are also separated and therefore the defects are not localized as Y-V-Y in their favorable configuration, but distributed on the lattice. These tetragonal-2 aligned oxygen atoms also occur in other investigated arrangements, but just locally in the oxygen vacancy surrounding.

To sum this up, starting from cubic $Fm\bar{3}m$ ZrO_2 lattice and placing one Y-V-Y defect cluster to this structure, both, the tetragonal and the metastable tetragonal-2 phases occur, dependent on the defect positions. Comparing them, the tetragonal structure is energetically more favorable against the metastable one. This metastable tetragonal-2 phase could also explain the appearance of the previously found tetragonal t' and t'' phases in many phase diagrams [59–63].

Another interesting metastable phase of ZrO_2 is the so called metamonoclinic or monoclinic-like phase. This phase is located between the tetragonal and monoclinic phase and evolves at a higher unit cell volume, with respect to the common monoclinic one. One can also imagine the tetragonal unit cell with a slightly larger volume and additional shearing applied to it, to reach this metamonoclinic phase. One can try to describe the origin of the name, because this phase is tetragonal like, but with coordination numbers like in the stable monoclinic ZrO_2 phase - zirconium atoms are 7-fold coordinated and oxygen atoms are 3- and 4-fold coordinated.

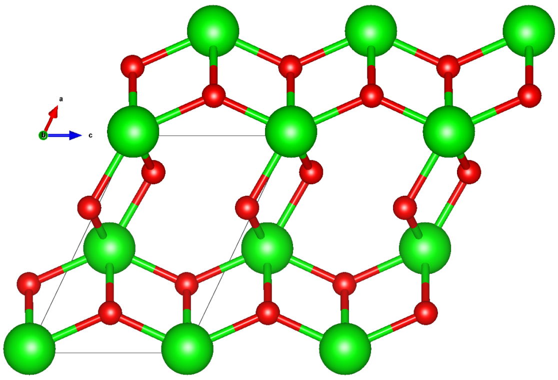

Figure 3.6: Metamonoclinic phase of ZrO_2.

Figure 3.6 shows exactly this metamonoclinic phase and one can see the tetragonal like rows with the shifted oxygen atoms and of course the 'tunnel' along the b-axis. The curious thing about this phase is, that it appears in nearly every of the investigated doping regions. Some examples are shown in the figure 3.7 below.

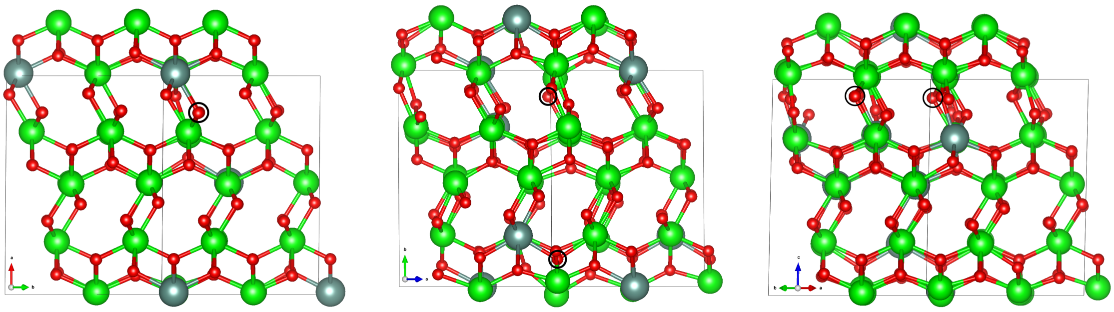
(a) (b) (c)

Figure 3.7: The metamonoclinic phase appearing in (a) 3YSZ, (b) 7YSZ and (c) 10YSZ. The black circles denote the rows with the oxygen vacancies. (Y=gray, Zr=green, O=red)

It is obvious, that this phases correspond to the metamonoclinic phase found for pure ZrO_2. One can also see the tetragonal arrangement of the rows, but in contrast to the pure metamonoclinic phase, the neighboring tunnels are not aligned in one direction, but form a zig-zag-pattern. The rows with the oxygen vacancies are marked via a black circle, therefore it is recognizable that the surrounding oxygen atoms are pulled towards the vacancies. It is also interesting that the vacancies are mostly located in the oxygen rows in this tunnel-like structures. One explanation could be that this vacancy arrangement favors the appearance of this metastable phase, and of course, it is more likely to remove one 3-fold coordinated oxygen atom from this tunnel-rows than from the 4-fold coordinated tetragonal-like rows. In a sense, Rushchanskii et al. [85] also found this structure with USPEX and VASP using PBE+U. Rebuilding their substoichiometric Zr_4O_7 phase, named as red phase with space group Cm (no. 8), and doing a simple ionic relaxation using PBE without additional Hubbard-U leads directly to the metamonoclinic phase, but also aligned in the zig-zag-pattern as shown for YSZ. The vacancy in their configuration is also located in a tetragonal-like oxygen row.

The even more curious occurrence can be found when calculating energy-volume-curves, which is a main preparation task when doing structure analysis via DFT. In 3YSZ, 7YSZ and 10YSZ this curves calculated with PBE would predict exactly this metamonoclinic phase as energetically most favorable, compared to the cubic, tetragonal and monoclinic one. Doing these calculations using SCAN functional, the metamonoclinic structure gets less stable within all configurations. These curves for 10YSZ can be seen in figure 3.8. Summarized, one has to be very careful when calculating bulk properties of YSZ just using PBE functional, because it leads to a wrong energetic order of the phases, compared to the SCAN functional, which seems to solve this problem and delivers the right description. Because this metamonoclinic structure has not been found yet by any experiment, it is claimed to be a PBE artifact.

Back to the beginning of this section, figure 3.9 shows the calculated phonon spectrum for 10YSZ. Even for very accurate forces, the calculated phonon spectrum for the energetically most favorable arrangement of 10YSZ shows negative frequencies. This result is in contrast to the reported values of Xia et al. [86], who used a force-field approach, and the expected results, where there should be no negative frequencies for 10YSZ at all. In comparison to c-ZrO_2, the negative forces in this case correspond mostly to zirconium and yttrium atoms instead of oxygen atoms. This could mean, that the oxygen atoms and even the oxygen vacancies are described very well, whereas the Y and Zr atoms could be caught in locally metastable positions, which is definitely possible, due to the results of the metastable phases with PBE functional shown above. It is also recognizable, that with the additional defects in the lattice, there is a higher amount of low frequencies than in the clean c-ZrO_2 lattice. Especially Y and Zr atoms tend to lower frequencies. The negative frequencies of c-ZrO_2 are located at −7 THz and belong to oxygen atoms, whereas the negative frequencies of 10YSZ are located at approximately −1 THz and belong to Y and Zr atoms. Another difference is, that the negative bands for c-ZrO_2 in the gamma point start at their negative values, but in 10YSZ these bands at the gamma point start directly at zero and then migrate slightly into the negative region.

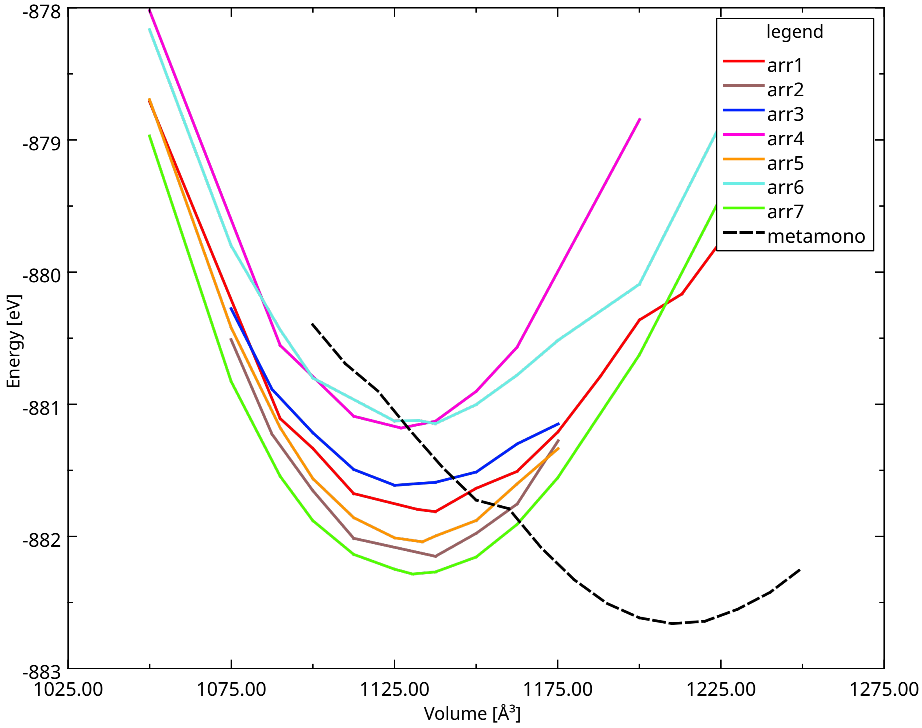

(a)

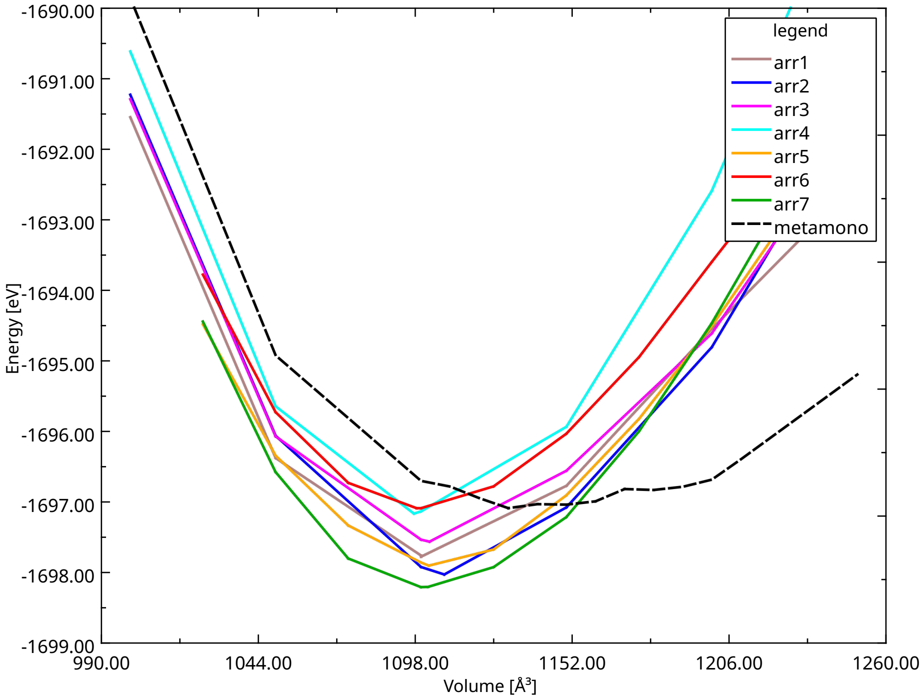

(b)

Figure 3.8: Energy-volume curves for 10YSZ, calculated using (a) PBE and (b) SCAN functional.

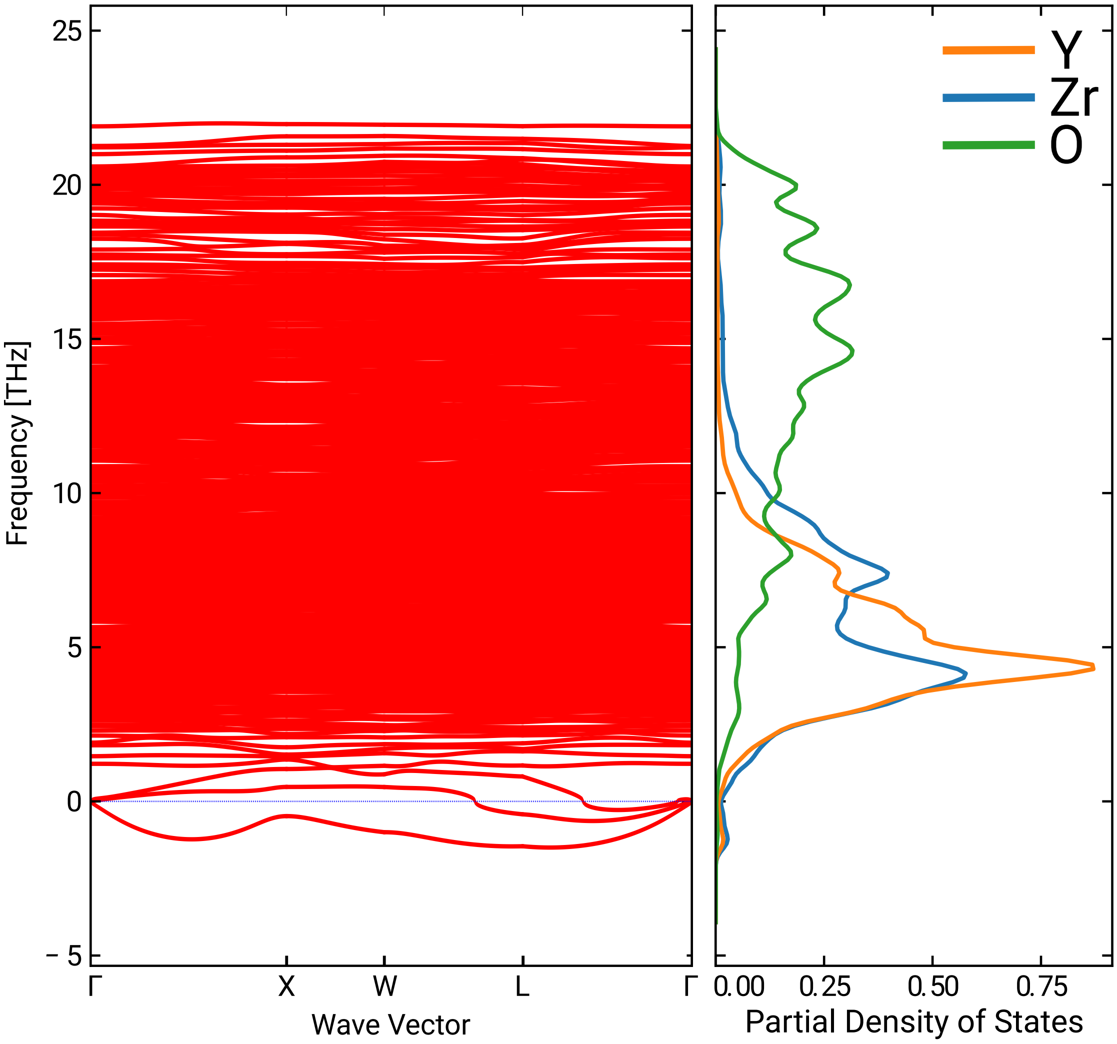

Figure 3.9: Phonon spectrum for 10YSZ calculated using PBE functional. The imaginary modes belong essentially to Y and Zr atoms.

4 Results and Discussion II

4.1 YSZ(111) Surface Configurations and -Energies

Other density functional theory calculations on low index planes for cubic YSZ showed, that the (111) terminated surface is the most stable one [87]. For further calculations the (111) surface was chosen and different arrangements, also concerning yttrium segregation [88], were chosen to investigate their stability and calculate their surface energy via equation 4.1.

$$\gamma = \frac{1}{2A} \cdot (E_{slab} - N \cdot E_{bulk}) \tag{4.1}$$

E_{slab} is the energy of the relaxed slab, E_{bulk} is the bulk energy of each species (ZrO_2 and Y_2O_3), N is their amount and A is the surface area. The initial configurations of two of the investigated surfaces can be seen in figure 4.1.

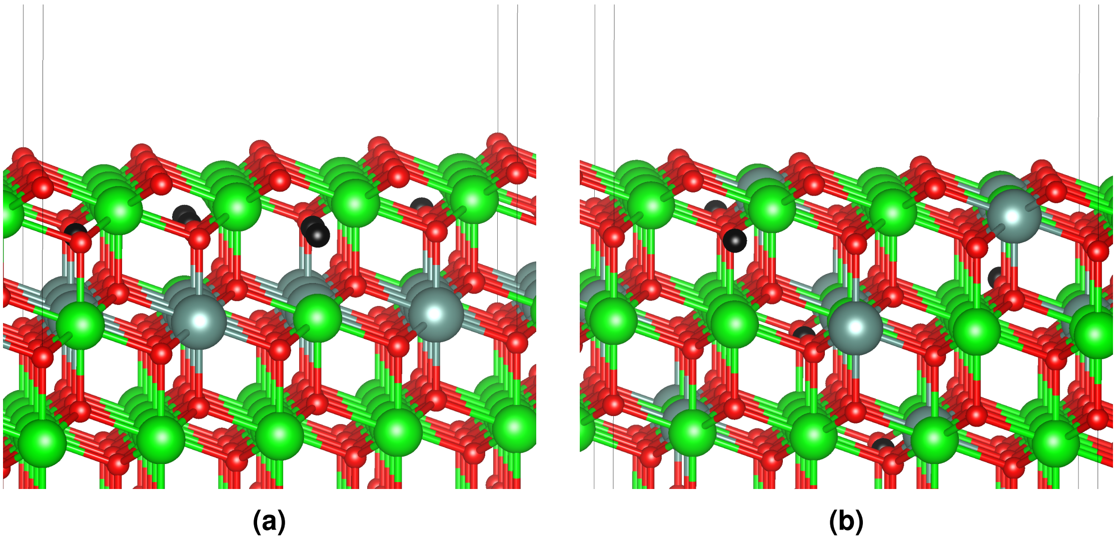

Figure 4.1: The initial positions of the surfaces (a) containing yttrium segregation and oxygen vacancies in the top surface O-Zr-O trilayer, and (b) cut from the bulk of 10YSZ with oxygen vacancies aligned and distributed through the surface slab. (Y=gray, Zr=green, O=red, V_O=black)

This figure shows two completely different settings for a (111) surface of YSZ. The first arrangement shows a subsurface yttrium layer, corresponding to 10 mol% Y_2O_3 in the surface slab, with all oxygen vacancies put above this layer. This slab was created directly from the pure c-ZrO_2 (111) surface by adding yttrium and removing oxygen.

The second one shows a 10YSZ (111) surface, created directly from the energetically most favorable bulk structure of 10YSZ, in which the yttrium atoms are aligned in rows along the [010] direction and oxygen vacancies are distributed through the bulk, placed in nn and nnn postions to the yttrium atoms. The relaxed structures can be seen in figure 4.2.

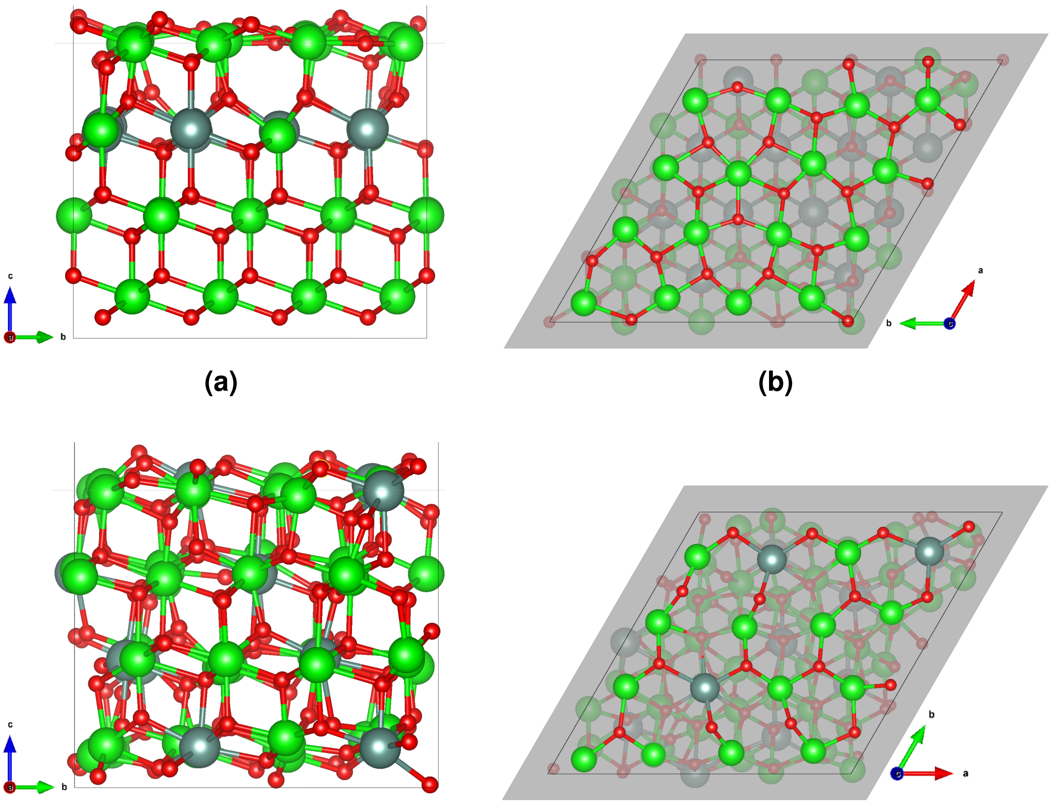

(a) (b)

(c) (d)

Figure 4.2: (a,b) side and top view of a YSZ (111) surface with a subsurface yttrium layer and oxygen vacancies put above this layer. (c,d) side ant top view of a (111) surface, cut directly from the bulk arrangement of 10YSZ.

Both surfaces are oxygen terminated, but just the second one shows 2-fold coordinated and stable surface oxygen atoms on bridging sites, which can also be found on the monoclinic ZrO_2 ($\bar{1}11$) surface. In comparison, the c(111) ZrO_2 surface has 3-fold coordinated oxygen atoms and 7-fold coordinated Zr atoms, the m($\bar{1}11$) ZrO_2 has 2- and 3-fold coordinated oxygen atoms and 6- and 7-fold coordinated Zr atoms.

The first report about segregation in YSZ, which is associated with the first surface arrangement shown above, was given by Winnubst et al. [89]. They used AES to claim that yttrium atoms segregate to the surface, which leads to an enrichment of the surface layer, with respect to the bulk concentration. Burggraaf et al. [90] and Theunissen et al. [91] used XPS and AES to reveal the key features about segregation in YSZ. They found a surface composition of 19 mol% to 23 mol% yttria, independent of the bulk concentration, which varied between 3 mol% to 21 mol% Y_2O_3

in their investigated structures. They also observed this segregation-enrichment of YSZ both for tetragonal zirconia polycrystals and cubic YSZ. At last they found out, that silicon also exhibited segregation if it is present as an impurity in the crystal structure. Further experimental investigations using SIMS and angle resolved XPS by Hughes [92] showed, that the outermost surface layer is predominantly enriched with impurities like silicon, whereas the sublayer within 7 nm is enriched with yttrium atoms, due to the fact that the Si/Zr ratio shows a much higher angle dependency than the Y/Zr ratio. These impurity atoms segregate to the surface independently of the bulk concentration and this could also lead to a yttria-rich silicate interface structure that is quite stable.

Anyway, for the investigated (111) surfaces of YSZ only yttrium, zirconium and oxygen atoms were used to reduce the amount of parameters and possible degrees of freedom. The two surfaces shown above deliver the lowest surface energies, with respect to the investigated ones. The first one, including yttrium segregation, results in 38 meV/Å^2 (616 mJ/m^2), whereas the surface cut directly from the bulk leads to 37 meV/Å^2 (593 mJ/m^2), using the PBE functional for both surfaces. These values are slightly smaller than those for the pure c-ZrO_2 (111) surface calculated via PBE (862 mJ/m^2) or found by Christensen and Carter [93] (1193 mJ/m^2) and Grau-Crespo et al. [94] (1080 mJ/m^2). With the use of the SCAN functional, the surface energies are slightly higher than those calculated with PBE. The surface energy for the bulk-like configuration is 56 meV/Å^2 (898 mJ/m^2), whereas the yttrium segregated surface results in 50 meV/Å^2 (797 mJ/m^2). This results are somehow comparable to the experimental values and fit much better than those calculated with PBE. It is also interesting, that the configuration with the yttrium subsurface layer and the oxygen vacancies put below this layer, results in a surface energy of 56 meV/Å^2 (899 mJ/m^2, PBE) and is therefore not as stable as the favored surface configuration, where the vacancies are put above this layer. In addition the bulk structures with yttrium layers in the (111) plane belong to the rather unfavorable ones, with respect to the investigated ones in this thesis. For 10YSZ it is possible to create one small yttrium layer in the bulk 2x2x2 unit cell of c-ZrO_2, whereas in 33YSZ it is possible to create alternating layers of Zr and Y in the same unit cell, but the results are the same, both structures are still stable, but belong to the most unfavorable investigated ones. In the surface configuration with the oxygen vacancies above the yttrium layer it is also recognizable, that the oxygen yttrium bonds got extended by an average of 5 %, which is comparable to the values of the bulk structure of Y_2O_3 and could be explained with the larger ionic and covalent radius of yttrium.

In the structure with the yttrium subsurface layer, one has to remove some oxygen atoms and create oxygen vacancies due to charge neutrality. If such an oxygen vacancy is present on the bottom side of the surface O–Zr–O trilayer, one of the surface oxygen atoms got attracted by this vacancy and they switch positions. The oxygen vacancy, now on the top side of the surface trilayer, attracts the nearby oxygen atoms and elevating them towards the surface. This leads to broken bonds between oxygen atoms in the surface trilayer and yttrium atoms in the subsurface layer. The whole process can be seen in figure 4.3. The new position of the oxygen vacancy isn't a big surprise, now located at the surface maximizing the distance to the subsurface yttrium atoms and located in the middle of the triangular structure, the distance to the subsurface yttrium atoms is approximately 4.25 Å, which is the same distance as in the most favorable configuration for a Y–V_O–Y defect cluster in the 3YSZ bulk, where the oxygen vacancy sits 4.25 Å (next nearest neighbor position) away from the yttrium atoms. This leads to the assumption, that this action of position changing is favored by the oxygen vacancies. The resulting surface structure is comparable with the honeycomb structure on the c-ZrO_2 (111) surface, but with one oxygen atom placed in the middle of such a formation, creating this triangle configuration in the middle of the structure. In this configuration, the surface zirconium atoms are 5-, 6- or 7-fold coordinated, due to the defect rich surface trilayer, but nonetheless the surface honeycomb symmetry is broken and a triangular superstructure occurred.

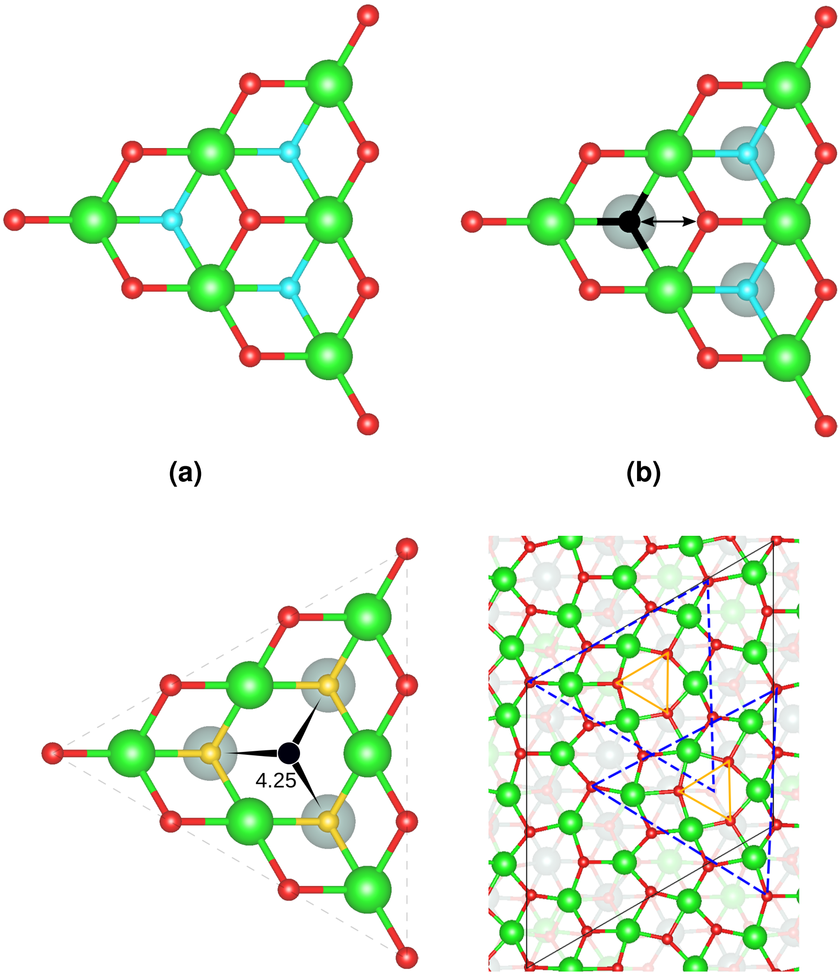

(a) (b)

(c) (d)

Figure 4.3: Schematic top view of the mechanism that leads to surface oxygen vacancies. (a) shows a clean c-ZrO_2 (111) surface. The green balls are Zr atoms, the small red balls are topmost oxygen atoms and the light blue balls are oxygen atoms on the bottom side of the surface O–Zr–O trilayer. (b) When adding yttrium atoms to the subsurface layer (gray balls) one has to also add oxygen vacancies (black balls). The oxygen vacancy changes position with one surface oxygen atom due to the next nearest yttrium atoms. (c) The oxygen vacancy is equidistant away 4.25 Å on a next nearest neighboring position to the subsurface yttrium atoms and pulling the surrounding oxygen atoms from the bottom of the surface trilayer upwards (yellow balls) to the same height as the Zr atoms, so they break their bonds to the yttrium atoms below. (d) The relaxed surface with Y in the subsurface. One can recognize the triangle superstructures with the oxygen vacancy located in the middle. The overlapping could occur due to a too small unit cell.

Summarized, the oxygen atoms in the surface trilayer are more likely to get and stay 3-fold coordinated, instead of preferring 2-fold coordination, when oxygen vacancies are present in this trilayer or below. In the bulk-like surface slab, these vacancies are distributed throughout the slab, and therefore enabling surface oxygen atoms to stay at a preferred 2-fold coordinated site without vacancies attracting them and pulling them towards the bulk, which would result in 3-fold coordinated surface oxygen atoms.

For a better overview and for future use during adsorption studies, the surface Zr and Y atoms got numbered. Figure 4.4 not only shows the numbering of the surface cations, but also the differences between the used functionals. One of the main differences of the bulk-like surfaces in the first row concerns atoms 5, 6 and 14. With PBE there is a 2-fold coordinated oxygen atom including atom 6 and 14, whereas using SCAN functional, this oxygen atom gets 3-fold coordinated to atoms 5, 6 and 14, which could have a strong effect on molecular or dissociative adsorption of molecules on this surface. The second row shows the surface concerning yttria segregation, but one can see, that there is no big difference in the calculated surface structure, but in both cases these elevated and mirrored oxygen atoms occur.

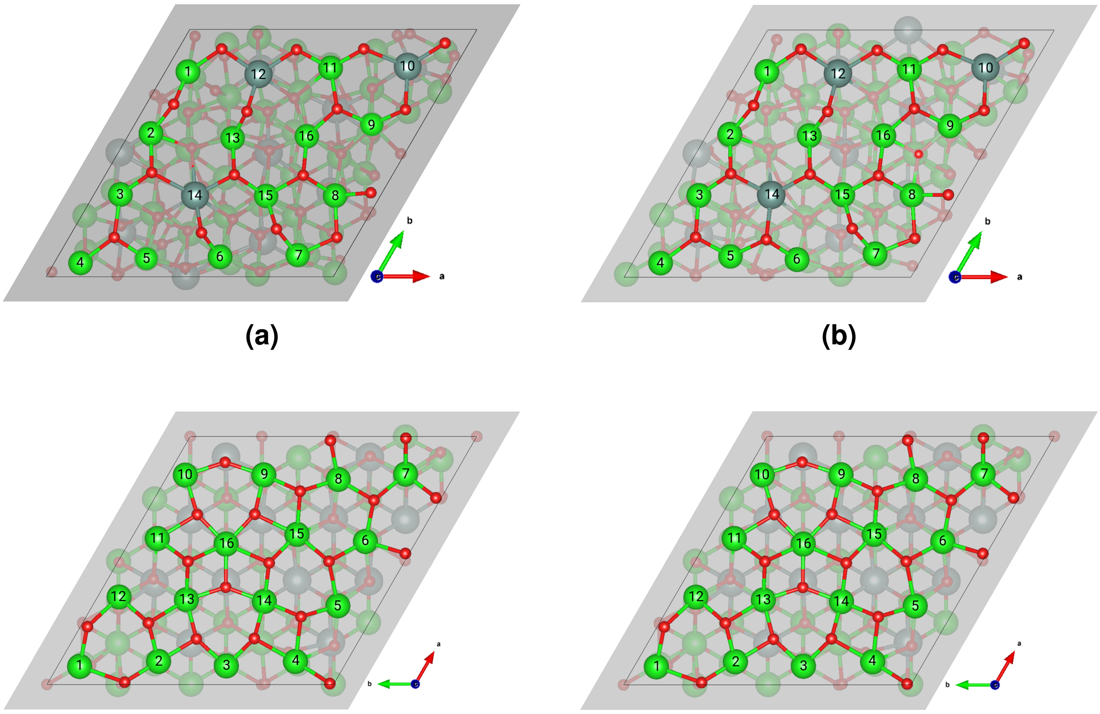

(a) (b) (c) (d)

Figure 4.4: The first row shows the calculated surface cut from the energetically most favorable bulk structure of 10YSZ and calculated with the use of (a) PBE and (b) SCAN functional. The second row shows the surface concerning yttrium segregation to the subsurface layer, also calculated with the use of (c) PBE and (d) SCAN functional.

4.2 Adsorption of H_2O on c-YSZ(111)

The energetically most favorable surface configurations mentioned in the previous section were taken to investigate the adsorption behavior of H_2O molecules on them. The water molecules were placed directly above the surface zirconium or yttrium atoms, which corresponds to a coverage of 6 % for each investigated configuration (each occupied surface cation on-top site would be 100 % coverage). The two hydrogen atoms, with respect to the oxygen atom of the molecule, were placed on the far side of the surface. Due to the different coordination numbers of the surface atoms and different chemical environment, also treated in the previous section, one would expect varying site-dependent adsorption energies. Because of the relatively large surface area of approximately 180 Å^2, self interaction with neighboring water molecules can be neglected. These interactions have to be considered when calculating smaller surface areas, due to the use of periodic boundary conditions.

Starting with the (111) surface concerning yttrium segregation and only Zr and O atoms in the surface trilayer, the results in table 4.1 and 4.2 calculated with the use of PBE and SCAN functional, show, that molecular adsorption occurs on 5- and 6-fold coordinated surface cations. The adsorption energy for it with PBE ranges from –283 meV to –724 meV and has therefore an energy difference ΔE_{ads} of 441 meV. With SCAN the results range from –491 meV to –960 meV with a difference ΔE_{ads} of 469 meV, which both are similar to the results of Chaopradith et al. [95]. During the process of adsorption, the hydrogen atoms got tilted towards the surface and one of these hydrogen atoms can form a hydrogen bond with one surface oxygen. The average distance between surface cations and adsorbed water oxygen atom is 2.44 Å and it seems, that the positions of the oxygen vacancies in the layer below are not the crucial factor for the strength of adsorption. The average O-H bond length of the adsorbed molecules got extended by 3 % just like the H-O-H angle.

Dissociative adsorption is possible on 5-, 6- and 7-fold coordinated cations when using the PBE functional and happens on 5 different investigated sites, starting with the previously mentioned on-top arrangement of the water molecules. When using the SCAN functional, dissociative adsorption occurs only 3 times and just on 6 fold coordinated surface cations with subsurface oxygen vacancies and no additional elevated subsurface oxygen atoms nearby. But this surrounding seems to be not the driving force for dissociative adsorption, due to other cation sites which also fulfill these settings. Dissociative adsorption leads to adsorption energies of –764 meV to –1245 meV with an energy difference ΔE_{ads} of 481 meV, similar to molecular adsorption and similar to dissociative adsorption energies for water calculated with PBE functional for the c-ZrO_2 (111) surface (–1347 meV). SCAN delivers –1286 meV to –1444 meV with ΔE_{ads} of 158 meV. The dissociation causes an average shift of 2 % to 7 % of the positions of local cations and nearby oxygen atoms. This could result in broken Y-O bonds in the subsurface, broken surface Zr-O bonds and also in 2-fold coordinated surface oxygen atoms, due to elevated cations. Due to the splitting of water in two surface hydroxy groups and straightening them up on the surface, the local repulsion of the oxygen atoms is pushing nearby oxygen atoms more towards the bulk and can lead to additional and weak Y-O bonds. So one hydroxy is placed right on top of one surface cation 1-fold coordinated with an average bond length of 2.08 Å and the other one takes the position of a bridging 2-fold coordinated hydroxy with an average bond length of 2.21 Å to the nearby cations. This mode of adsorption is also the same as for the pure c-ZrO_2 (111) surface, as can be seen in figure 4.5. In this figure one can also realize, that the surface cations and surface and subsurface anions got shifted slightly, due to the presence of the hydroxy groups. The average bond length for the 1-fold coordinated hydroxy on the c-ZrO_2 (111) surface is 2.02 Å and for the 2-fold coordinated it is 2.24 Å, comparable to YSZ. Nudged elastic band calculations of Chaopradith et al. [95] showed that this process of water dissociation on YSZ is barrierless, but the results for molecular adsorption show longer H–O bonds for some sites, but no dissociation occurs. This leads to the assumption, that there is a barrier which could be dependent on the surface configuration, as shown by Gorski et al. [96].

10YSZ(111) - Y Segregation - PBE						
#	$\#_{coord}$	E_{ads} [meV]	Zr/Y-O [Å]	O-$H_{\#1}$ [Å]	O-$H_{\#2}$ [Å]	∠H-O-H [°]
1_{Zr}	6	-724_m	2.38	0.97	1.02	110
2_{Zr}	5	-481_m	2.47	0.97	0.98	107
3_{Zr}	6	-612_m	2.40	0.97	1.00	109
4_{Zr}	7	-1245_d	2.09	0.97	1.02	/
5_{Zr}	5	-1126_d	2.10	0.97	1.03	/
6_{Zr}	6	-560_m	2.44	0.97	0.98	108
7_{Zr}	6	-283_m	2.54	0.97	0.98	108
8_{Zr}	6	-464_m	2.47	0.97	0.99	106
9_{Zr}	5	-596_m	2.45	0.97	0.98	107
10_{Zr}	6	-700_m	2.39	0.97	1.03	109
11_{Zr}	6	-764_d	2.09	0.97	1.03	/
12_{Zr}	6	-947_d	2.09	0.97	1.02	/
13_{Zr}	6	-547_m	2.44	0.97	0.99	108
14_{Zr}	5	-464_m	2.48	0.97	0.98	107
15_{Zr}	6	-1168_d	2.07	0.97	1.01	/
16_{Zr}	6	-686_m	3.38	0.97	1.02	109

Table 4.1: Calculated adsorption energies for each surface-cation on-top site including surface cation coordination number, distances between adsorbed water oxygen and surface cation, oxygen-hydrogen bond lenths and H-O-H angles, calculated using the PBE functional. The letters 'm' and 'd' denote molecular or dissociative adsorption. In the case of dissociative adsorption the oxygen-hydrogen bond length is given with respect to the surface oxygen atom.

10YSZ(111) - Y Segregation - SCAN						
#	$\#_{coord}$	E_{ads} [meV]	Zr/Y-O [Å]	O-$H_{\#1}$ [Å]	O-$H_{\#2}$ [Å]	∠H-O-H [°]
1_{Zr}	6	-960_m	2.34	0.96	0.99	111
2_{Zr}	5	-707_m	2.40	0.97	0.97	108
3_{Zr}	6	-861_m	2.37	0.97	0.99	109
4_{Zr}	7	-883_m	2.37	0.97	0.98	107
5_{Zr}	6	-1286_d	2.10	0.96	1.02	/
6_{Zr}	6	-791_m	2.39	0.97	0.97	109
7_{Zr}	6	-491_m	2.46	0.97	0.97	109
8_{Zr}	6	-770_m	2.39	0.97	0.97	110
9_{Zr}	5	-842_m	2.40	0.97	0.97	108
10_{Zr}	6	-948_m	2.37	0.97	1.01	110
11_{Zr}	6	-674_m	2.41	0.97	0.97	109
12_{Zr}	6	-1163_d	2.08	0.96	1.02	/
13_{Zr}	6	-790_m	2.39	0.97	0.98	109
14_{Zr}	5	-703_m	2.42	0.97	0.97	108
15_{Zr}	6	-1444_d	2.06	0.96	1.01	/
16_{Zr}	6	-905_m	2.36	0.96	1.00	111

Table 4.2: Calculated adsorption energies for each surface-cation on-top site including surface cation coordination number, distances between adsorbed water oxygen and surface cation, oxygen-hydrogen bond lenths and H-O-H angles, calculated using the SCAN functional. The letters 'm' and 'd' denote molecular or dissociative adsorption. In the case of dissociative adsorption the oxygen-hydrogen bond length is given with respect to the surface oxygen atom.

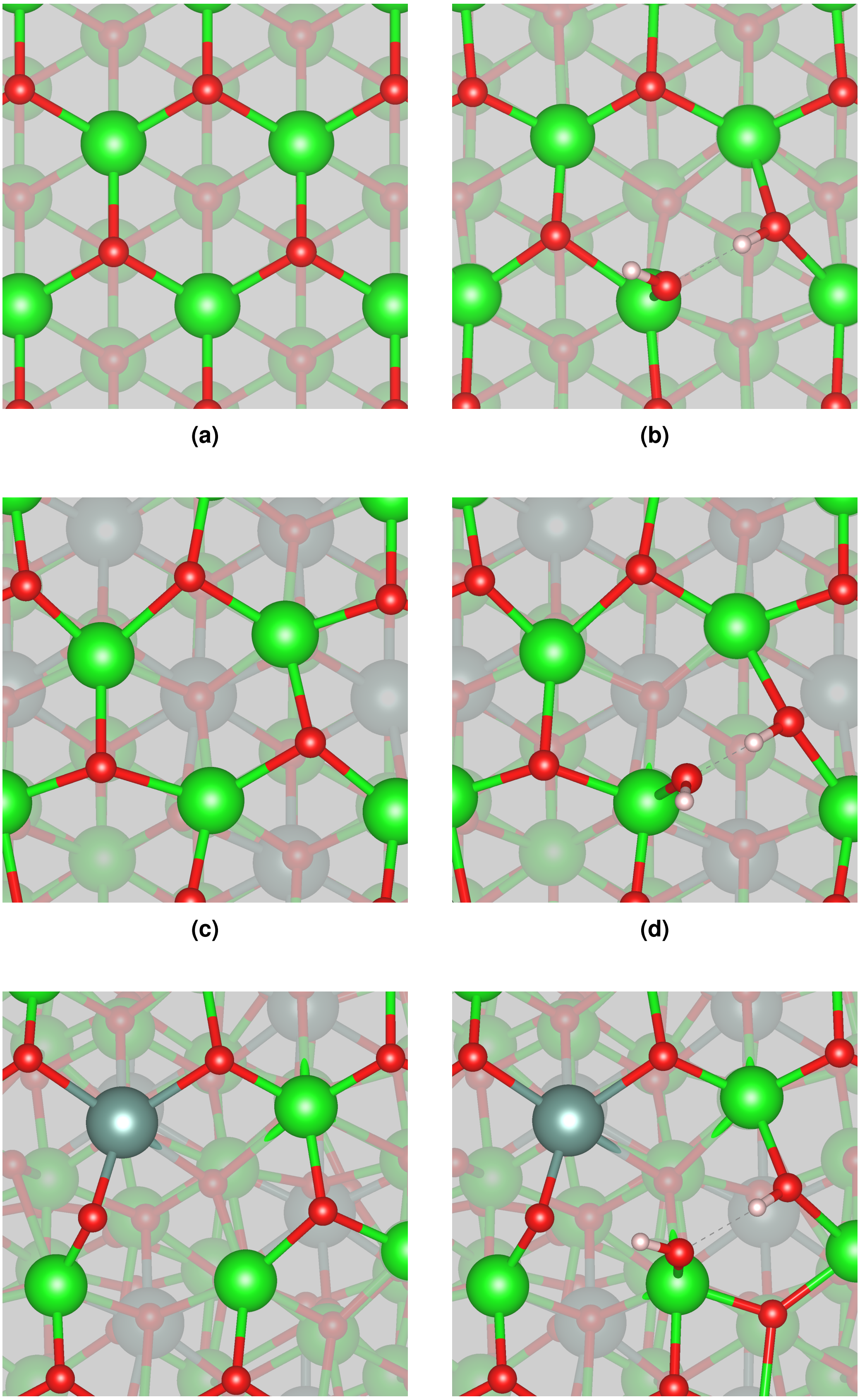

(a) (b)

(c) (d)

(e) (f)

Figure 4.5: In the left column there are the top views of clean (111) surfaces for (a) c-ZrO_2, (b) 10YSZ with subsurface Y segregation and (c) 10YSZ directly cut from the energetically most favorable bulk structure. The right column shows the modes of dissociative water adsorption on these surfaces with one broken surface bond, respectively. (Zr=green, Y=gray, O=red, H=white)

On the 10YSZ(111) bulk-like surface, molecular water adsorption occurs on 6- and 7-fold coordinated surface Zr and Y atoms, whereas molecular adsorption seems to be stronger on Y atoms. The results for PBE and SCAN functional can be found in tables 4.3 and 4.4. The resulting energy of molecular adsorption ranges from –371 meV to –926 meV with an energy difference ΔE_{ads} of 555 meV for the PBE functional. The results for the SCAN functional range from –548 meV to –947 meV with a difference ΔE_{ads} of 399 meV. In the previous section, a 2- or 3- fold functional dependent surface oxygen atom was mentioned between surface cations 5, 6 and 14. With the SCAN functional this configuration is stable also with an molecular adsorbed water molecule on surrounding cations, bending this molecule towards this surface oxygen atom. With the use of the PBE functional the water molecule adsorbs molecularly on top of atom 6 and 14, pulling this 2-fold coordinated oxygen atom up. Adsorption on atom 5 leads to the dissociation of the water molecule and the same adsorption modes as shown in figure 4.5, but without breaking any surface Zr-O bond, because the surface oxygen atom is already 2-fold coordinated. Apart from that, the molecular adsorption behavior is nearly the same as for the previously discussed surface with an average surface cation and anion displacement of 1 % to 3 %. The bond length between the water oxygen atom and the surface cation is 2.41 Å for PBE and 2.37 Å for SCAN.

Dissociative adsorption only occurs on Zr atoms and only on those, where a 2-fold coordinated surface oxygen atom is nearby. That is also the case for adsorption on atom 5, with PBE functional dissociative adsorption occurs, whereas with SCAN functional water adsorbs molecularly. Therefore it is also interesting, that there is no dissociative adsorption on atom 6, maybe because of the two neighboring 2-fold coordinated surface oxygen atoms seen on the PBE surface. The PBE functional delivers an adsorption energy of –1023 meV to –1540 meV with an difference ΔE_{ads} of –517 meV. The SCAN functional results are –1544 meV to –1982 meV with a difference ΔE_{ads} of –438 meV for dissociative adsorption of water. In this case, the splitting of water to form two hydroxy groups also leads to a local deformation of the surface and subsurface layer, which could result in additional broken weak bonds, due to elevated cations and repelled oxygen atoms. This happens because the hydroxy groups get straightened up and displacing the surface oxygen and zirconium atoms.

–523 meV to –560 meV was the calculated adsorption energy by Shishkin and Ziegler [97] for molecular water adsorption, and for dissociative water adsorption they got –1043 meV to –1473 meV, with the use of PBE functional and for different terminated YSZ(111) surfaces. Gorski et al. [96] found –432 meV for molecular water adsorption and –1700 meV for dissociative water adsorption by fitting simulations to experimentally found TPD curves. They also found an activation barrier between molecular and dissociative adsorption of approximately 1700 meV for adsorption on cationic sites or 300 meV for adsorption on an anionic site via pushing one surface oxygen to an oxygen vacancy site below. Chaopradith et al. [95] calculated –500 meV to –1190 meV and –2200 meV for molecular and dissociative water adsorption by trying different adsorption sites.

Finally, on the following pages figures 4.7 and 4.6 can be found, showing the investigated 10YSZ(111) surfaces with corresponding energies of adsorption for water.

10YSZ(111) - bulk-like - PBE						
#	$\#_{coord}$	E_{ads} [meV]	Zr/Y-O [Å]	O-$H_{\#1}$ [Å]	O-$H_{\#2}$ [Å]	$\angle$H-O-H [°]
1_{Zr}	6	-515_m	2.41	0.98	0.99	107
2_{Zr}	6	-609_m	2.41	0.97	1.01	107
3_{Zr}	6	-533_m	2.41	0.98	0.97	109
4_{Zr}	6	-699_m	2.36	0.98	1.00	106
5_{Zr}	6	-1540_d	2.07	0.97	1.01	/
6_{Zr}	6	-575_m	2.39	0.98	0.99	107
7_{Zr}	6	-371_m	2.42	0.98	0.99	109
8_{Zr}	6	-514_m	2.40	0.97	0.98	109
9_{Zr}	6	-634_m	2.37	0.98	1.00	107
10_Y	7	-746_m	2.40	0.98	1.01	106
11_{Zr}	6	-567_m	2.44	0.98	1.00	107
12_Y	6	-634_m	2.49	0.97	1.00	108
13_{Zr}	5	-1028_d	2.06	0.97	1.02	/
14_Y	7	-717_m	2.47	0.97	1.01	106
15_{Zr}	7	-926_m	2.37	0.98	1.00	105
16_{Zr}	6	-1343_d	2.01	0.97	0.99	/

Table 4.3: Calculated adsorption energies for each surface-cation on-top site including surface cation coordination number, distances between adsorbed water oxygen and surface cation, oxygen-hydrogen bond lenths and H-O-H angles, calculated using the PBE functional. The letters 'm' and 'd' denote molecular or dissociative adsorption. In the case of dissociative adsorption the oxygen-hydrogen bond length is given with respect to the surface oxygen atom.

10YSZ(111) - bulk-like - SCAN						
#	$\#_{coord}$	E_{ads} [meV]	Zr/Y-O [Å]	O-$H_{\#1}$ [Å]	O-$H_{\#2}$ [Å]	∠H-O-H [°]
1_{Zr}	6	-789_m	2.32	0.97	0.98	111
2_{Zr}	6	-774_m	2.37	0.97	1.00	106
3_{Zr}	6	-675_m	2.36	0.97	0.97	110
4_{Zr}	6	-643_m	2.37	0.97	0.97	105
5_{Zr}	7	-658_m	2.36	0.97	0.97	108
6_{Zr}	6	-947_m	2.27	0.96	1.04	111
7_{Zr}	6	-689_m	2.36	0.97	0.97	110
8_{Zr}	6	-780_m	2.30	0.97	0.97	112
9_{Zr}	6	-610_m	2.34	0.98	0.97	108
10_{Y}	7	-783_m	2.40	0.97	0.97	109
11_{Zr}	7	-619_m	2.45	0.97	0.98	107
12_{Y}	6	-645_m	2.44	0.96	0.97	109
13_{Zr}	6	-1544_d	2.06	0.96	1.01	/
14_{Y}	7	-756_m	2.41	0.97	0.97	109
15_{Zr}	7	-548_m	2.40	0.97	0.98	109
16_{Zr}	6	-1982_d	2.03	0.96	1.00	/

Table 4.4: Calculated adsorption energies for each surface-cation on-top site including surface cation coordination number, distances between adsorbed water oxygen and surface cation, oxygen-hydrogen bond lenths and H-O-H angles, calculated using the SCAN functional. The letters 'm' and 'd' denote molecular or dissociative adsorption. In the case of dissociative adsorption the oxygen-hydrogen bond length is given with respect to the surface oxygen atom.

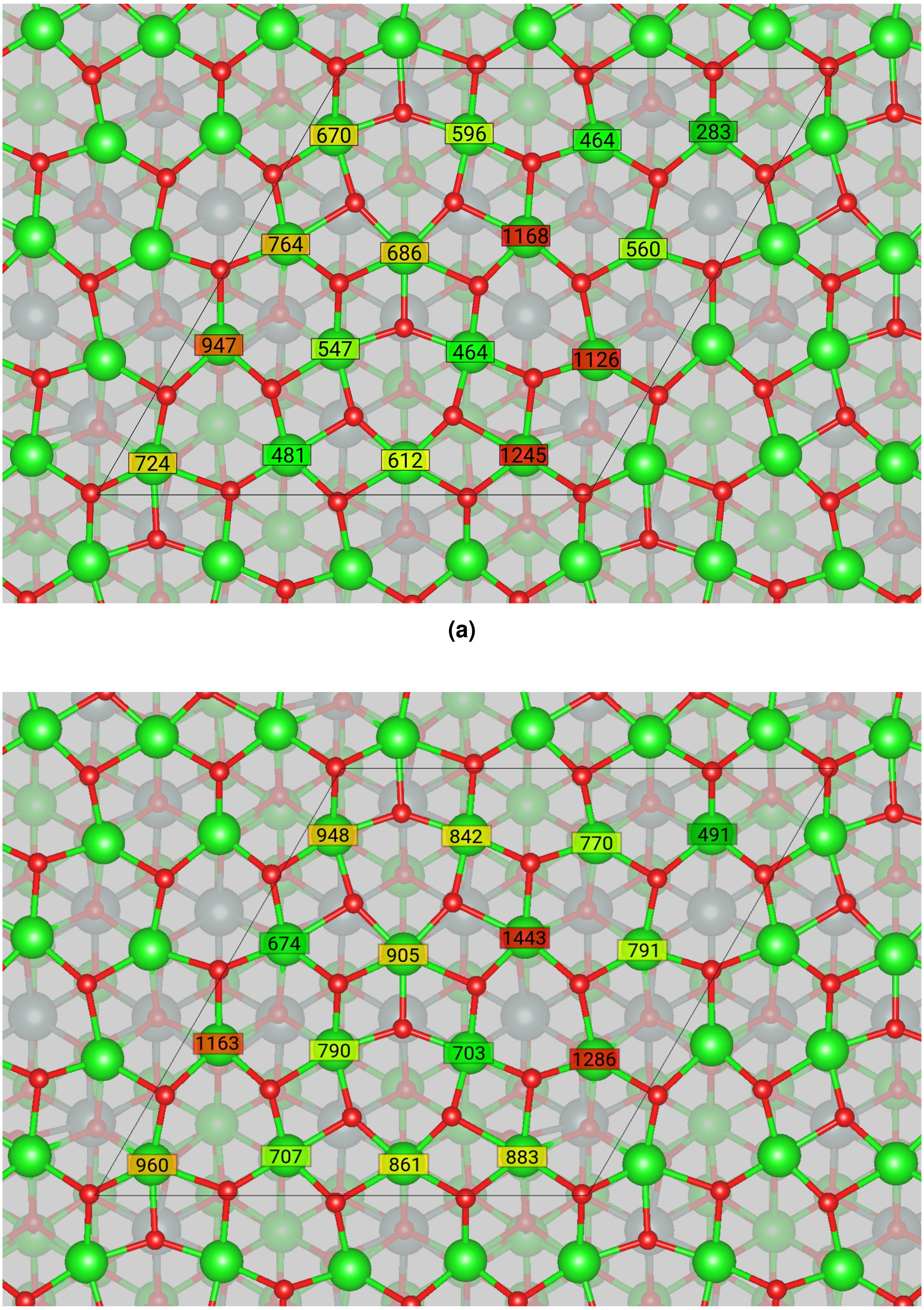

(a)

(b)

Figure 4.6: Calculated adsorption energies in meV for water on a 10YSZ(111) surface with yttrium segregated to the first subsurface trilayer, using (a) PBE and (b) SCAN functional.

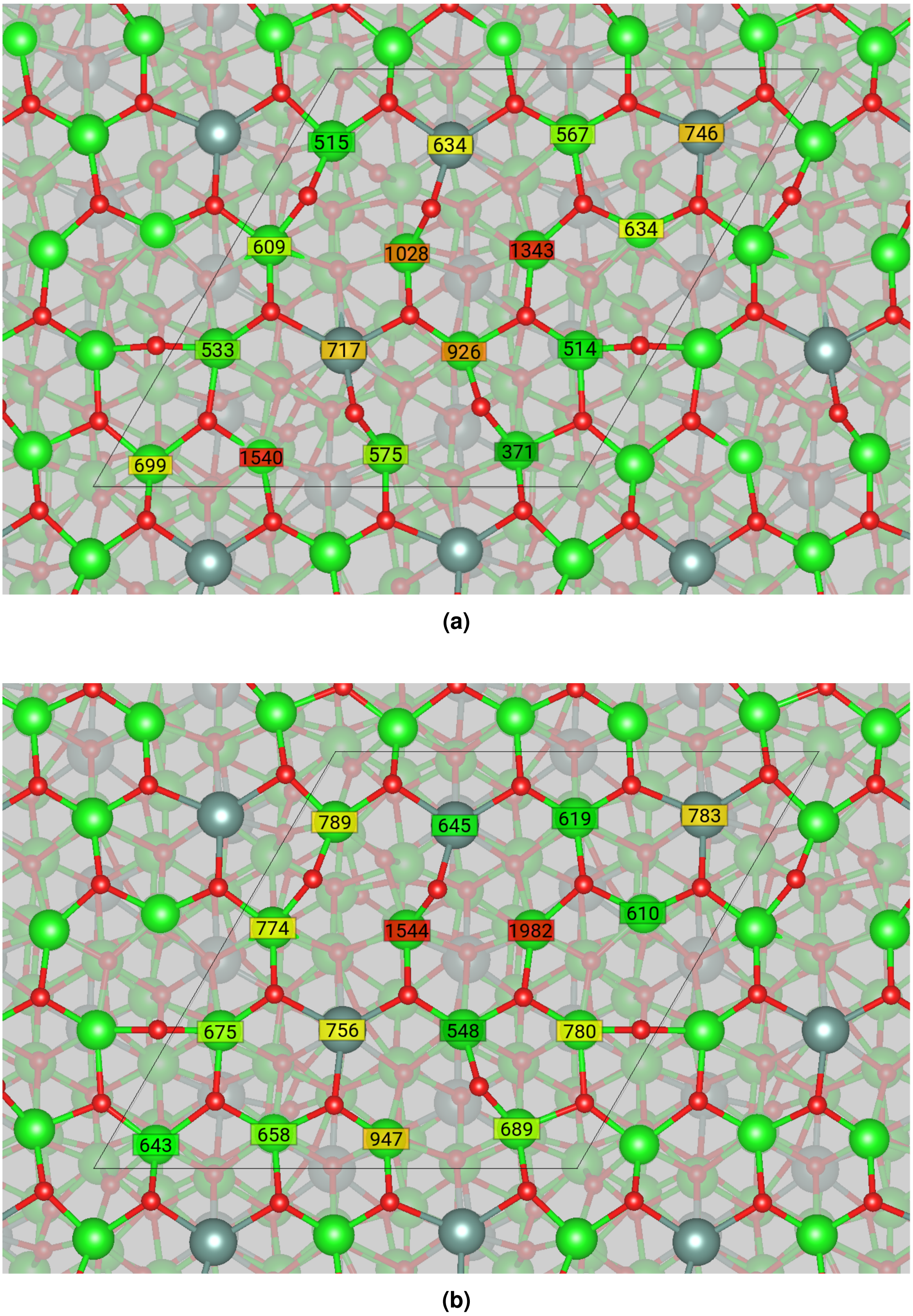

Figure 4.7: Calculated adsorption energies in meV for water on a 10YSZ(111) bulk-like surface, using (a) PBE and (b) SCAN functional.

5 Summary and Conclusion

The bulk investigations showed, that for amounts of 3 mol % to 7 mol % Y_2O_3 in c-ZrO_2 the resulting structure is tetragonal-like, whereas above the cubic phase gets stabilized. Calculations for different configurations of the Y-V_O-Y defect cluster in 3YSZ showed and proved the energetically favorable positions for yttrium atoms sitting on nearest neighboring positions with on oxygen vacancy on a next nearest neighboring position.

During the bulk relaxations, also metastable phases occurred, which can be seen in the calculated energy volume curves. Additional Phonon spectra calculation and analysis showed a phonon driven phase transition to a tetragonal-like phase which also appeared in 3YSZ and just locally for higher amounts of yttria. In contrast to this, the meta-monoclinic phase arose in every investigated doping regime. PBE predicts this metastable phases as energetically most favorable structures, which was claimed as a PBE artifact and should be kept at the back of one's mind. The SCAN functional predicts the right order of phases and also delivers very accurate results for bulk parameters and a better description of oxygen atom and oxygen vacancy positions.

Afterwards, surface investigations on different surface terminations were done and resulted in two favorable configurations - one bulk-like slab and one slab containing yttrium subsurface segregation and oxygen vacancies placed in the surface O-Zr-O trilayer. The second configuration also showed broken Y-O bonds in the subsurface and elevated oxygen atoms to the surface trilayer with oxygen atoms changing positions with oxygen vacancies. So if an aging effect and therefore also yttrium segregation in YSZ occurs, then this would lead to a local barrier for oxygen vacancies, generated by the yttrium subsurface layer, which they are very unfavorable to pass. This behavior was shown for 3YSZ with different unfavorable defect cluster configurations and could result in a lower ion conductivity, as well as a lower adsorption energy for water on this surface. Compared to the 10YSZ(111) surface cut directly from the bulk, the adsorption energies are lower on the 10YSZ(111) surface with the subsurface yttrium layer and oxygen vacancies in the surface trilayer of O-Zr-O. A summary of the results can be found in tables 5.1 and 5.2.

This leads to the assumption, that the oxygen vacancies predominantly influence the stability of the different 10YSZ(111) surfaces. The agglomeration of these vacancies leads to only 3-fold coordinated surface oxygen atoms which are very likely to break bonds to nearby Zr atoms during dissociative water adsorption when using the PBE functional, but with SCAN, dissociative adsorption mainly occurs beneath surface defects or 2-fold coordinated surface oxygen atoms, which are found on the bulk-like surface but not on the one with the yttrium sublayer. On this surface water only dissociates, if an oxygen vacancy or no other elevated subsurface oxygen atoms are nearby.

10YSZ(111) - Configuration 1	**PBE**	**SCAN**
Surf. Energy [meV/Å ^{2}]	38	56
Surf. Energy [mJ/m^2]	616	898
H_2O - $E_{ads,mol.}$ [meV]	-283 to -724	-491 to -960
H_2O - $E_{ads,diss.}$ [meV]	-764 to -1245	-1286 to -1444

Table 5.1: Summary for the calculated properties of the 10YSZ(111) surface with an yttrium layer in the subsurface and oxygen vacancies in the surface O-Zr-O trilayer.

10YSZ(111) - Configuration 2	**PBE**	**SCAN**
Surf. Energy [meV/Å ^{2}]	37	50
Surf. Energy [mJ/m^2]	593	797
H_2O - $E_{ads,mol.}$ [meV]	-371 to -926	-548 to -947
H_2O - $E_{ads,diss.}$ [meV]	-1023 to -1540	-1544 to -1982

Table 5.2: Summary for the calculated properties of the 10YSZ(111) bulk-like surface.

On the bulk-like (111) surface the distribution of the vacancies through the surface slab, and therefore only a few vacancies in the first two trilayers, stabilize 2-fold coordinated surface oxygen atoms. These 2-fold coordinated oxygen atoms promote dissociative adsorption and are the main reason for it on this surface. Summarized all surface related values calculated with PBE functional in this thesis fit to formerly found values for other YSZ(111) surface configurations and adsorption studies. Nonetheless, SCAN seems to describe the YSZ(111) surface structure and adsorption behavior of water much better, due to a more accurate bond length prediction.

Future work could consist of trying a hybrid exchange functional for smaller supercells and fewer atoms to describe the properties of YSZ. Also CO and CO_2 adsorption with the use of SCAN and hybrid exchange functionals would be interesting to study. In addition, bulk and surface core level shifts, due to different bulk structures and surface terminations and configurations, could be interesting to explain XPS results and therein maybe shifts originating from adsorbed molecules or undercoordinated surface oxygen atoms. Therefore YSZ thin films would also be interesting to study and simulated STM images could help to explain the experimentally found results for these films.

6 Acknowledgements

I would like to thank my supervisor Josef Redinger for giving me the chance to work on this topic and for giving me the opportunity to finish my diploma thesis. In addition, I would like to express my gratitude to all members of the Computational Materials Science Group at the Vienna University of Technology for their support, the nice working atmosphere and the nice physical and non-physical discussions at lunch, which I was allowed to listen and participate to. Special thanks go to Wernfried Mayr-Schmölzer and Jakub Planer, who had always time for helping me out with computational issues and for answering my questions evolving during my research. They consistently allowed this thesis to be my own work, but steered me in the right scientific direction whenever I needed it.

I am also grateful for the funding by the Austrian Science Foundation FWF and the FOXSI program, as well as the VSC-3 team for their support and providing a stable computational environment.

Finally I would like to express my gratitude to my family, my girlfriend, my friends and my study colleagues, who always supported me morally and financially. Without their support I would not have been able to finish my studies and my diploma thesis - Thank You!

Bibliography

[1] Jos Thijssen. *Computational Physics*. Cambridge University Press, Cambridge, 2007. ISBN 9781139171397. doi: 10.1017/CBO9781139171397. URL http://ebooks.cambridge.org/ref/id/CBO9781139171397.

[2] P. Hohenberg and W. Kohn. Inhomogeneous Electron Gas. *Physical Review*, 136(3B):864–871, 1964. ISSN 0378620X. doi: 10.1007/BF01198136.

[3] Silke Bühler-Paschen and Peter Mohn. *Festkörperphysik II*. Vienna, 2014.

[4] John P Perdew, Kieron Burke, and Matthias Ernzerhof. Generalized Gradient Approximation Made Simple. *Physical Review Letters*, 77(18):3865–3868, oct 1996. ISSN 0031-9007. doi: 10.1103/PhysRevLett.77.3865. URL https://link.aps.org/doi/10.1103/PhysRevLett.77.3865.

[5] Jianwei Sun, Adrienn Ruzsinszky, and John P. Perdew. Strongly Constrained and Appropriately Normed Semilocal Density Functional. *Physical Review Letters*, 115(3):036402, jul 2015. ISSN 0031-9007. doi: 10.1103/PhysRevLett.115.036402. URL https://link.aps.org/doi/10.1103/PhysRevLett.115.036402.

[6] Jorge M. Seminario. An introduction to density functional theory in chemistry. In *Theoretical and Computational Chemistry*, volume 2, pages 1–27. Department of Chemistry, Imperial College of Science Technology and Medicine, London, London, 1995. ISBN 9780470373. doi: 10.1016/S1380-7323(05)80031-7. URL https://linkinghub.elsevier.com/retrieve/pii/S1380732305800317.

[7] Marie-Liesse Doublet. *Introduction to Density Functional Theory*. Institut Charles Gerhardt, CNRS - Université Montpellier, Montpellier, 2018. URL https://meeticc2018.sciencesconf.org/data/pages/DFT{_}GDR{_}Meeticc.pdf.

[8] G. Kresse and J. Hafner. Ab initio molecular dynamics for liquid metals. *Physical Review B*, 47(1):558–561, jan 1993. ISSN 0163-1829. doi: 10.1103/PhysRevB.47.558. URL https://link.aps.org/doi/10.1103/PhysRevB.47.558.

[9] G. Kresse and J. Hafner. Ab initio molecular-dynamics simulation of the liquid-metal–amorphous-semiconductor transition in germanium. *Physical Review B*, 49(20):14251–14269, may 1994. ISSN 0163-1829. doi: 10.1103/PhysRevB.49.14251. URL https://link.aps.org/doi/10.1103/PhysRevB.49.14251.

[10] G. Kresse and J. Furthmüller. Efficiency of ab-initio total energy calculations for metals and semiconductors using a plane-wave basis set. *Computational Materials Science*, 6(1):15–50, jul 1996. ISSN 09270256. doi: 10.1016/0927-0256(96)00008-0. URL http://linkinghub.elsevier.com/retrieve/pii/0927025696000080.

[11] G. Kresse and J. Furthmüller. Efficient iterative schemes for ab initio total-energy calculations using a plane-wave basis set. *Physical Review B*, 54(16): 11169–11186, oct 1996. ISSN 0163-1829. doi: 10.1103/PhysRevB.54.11169. URL https://link.aps.org/doi/10.1103/PhysRevB.54.11169.

[12] D M Wood and Alex Zunger. A new method for diagonalising large matrices. *Journal of Physics A: Mathematical and General*, 18(9):1343–1359, jun 1985. ISSN 0305-4470. doi: 10.1088/0305-4470/18/9/018. URL http://stacks.iop.org/0305-4470/18/i=9/a=018?key=crossref.ead0ad749bd4e8eb83699277e98b8828.

[13] Péter Pulay. Convergence Acceleration of Iterative Sequences - The Case of SCF Iteration. *Chemical Physics Letters*, 73(2):393–398, jul 1980. ISSN 00092614. doi: 10.1016/0009-2614(80)80396-4. URL http://linkinghub.elsevier.com/retrieve/pii/0009261480803964.

[14] Michael P. Teter, Michael C. Payne, and Douglas C. Allan. Solution of Schrödinger's equation for large systems. *Physical Review B*, 40(18):12255–12263, dec 1989. ISSN 0163-1829. doi: 10.1103/PhysRevB.40.12255. URL https://link.aps.org/doi/10.1103/PhysRevB.40.12255.

[15] D. M. Bylander, Leonard Kleinman, and Seongbok Lee. Self-consistent calculations of the energy bands and bonding properties of B12C3. *Physical Review B*, 42(2):1394–1403, jul 1990. ISSN 0163-1829. doi: 10.1103/PhysRevB.42.1394. URL http://prb.aps.org/pdf/PRB/v42/i2/p1394{_}1.

[16] Geerd H.F. Diercksen and Stephen Wilson. *Methods in Computational Molecular Physics*. Springer Netherlands, Dordrecht, 1983. ISBN 978-94-009-7202-5. doi: 10.1007/978-94-009-7200-1. URL http://link.springer.com/10.1007/978-94-009-7200-1.

[17] E.R. Davidson. Numerical Algorithms in Chemistry: Algebraic Methods. Technical report, University of California, Lawrence Berkeley Laboratory, 1978.

[18] P. E. Blöchl. Projector augmented-wave method. *Physical Review B*, 50 (24):17953–17979, dec 1994. ISSN 0163-1829. doi: 10.1103/PhysRevB.50.17953. URL https://link.aps.org/doi/10.1103/PhysRevB.50.17953.

[19] M Dion, H Rydberg, E. Schröder, D C Langreth, and B I Lundqvist. Van der Waals Density Functional for General Geometries. *Physical Review Letters*, 92(24):246401, jun 2004. ISSN 0031-9007. doi: 10.1103/PhysRevLett.92.246401. URL https://link.aps.org/doi/10.1103/PhysRevLett.92.246401.

[20] David R Bowler and Angelos Michaelides. Van der Waals density functionals applied to solids. 195131:1–13, 2011. doi: 10.1103/PhysRevB.83.195131.

[21] Guillermo Román-Pérez and José M. Soler. Efficient Implementation of a van der Waals Density Functional: Application to Double-Wall Carbon Nanotubes. *Physical Review Letters*, 103(9):096102, aug 2009. ISSN 0031-9007. doi: 10.1103/PhysRevLett.103.096102. URL https://link.aps.org/doi/10.1103/PhysRevLett.103.096102.

[22] Kyuho Lee, Éamonn D. Murray, Lingzhu Kong, Bengt I Lundqvist, and David C Langreth. Higher-accuracy van der Waals density functional. *Physical Review B*, 82(8):081101, aug 2010. ISSN 1098-0121. doi: 10.1103/PhysRevB.82.081101. URL https://link.aps.org/doi/10.1103/PhysRevB.82.081101.

[23] Stefan Grimme, Jens Antony, Stephan Ehrlich, and Helge Krieg. A consistent and accurate ab initio parametrization of density functional dispersion correction (DFT-D) for the 94 elements H-Pu. *The Journal of Chemical Physics*, 132(15):154104, apr 2010. ISSN 0021-9606. doi: 10.1063/1.3382344. URL http://aip.scitation.org/doi/10.1063/1.3382344.

[24] Stefan Grimme, Stephan Ehrlich, and Lars Goerigk. Effect of the damping function in dispersion corrected density functional theory. *Journal of Computational Chemistry*, 32(7):1456–1465, may 2011. ISSN 01928651. doi: 10.1002/jcc.21759. URL http://doi.wiley.com/10.1002/jcc.21759.

[25] A. van de Walle, P. Tiwary, M. de Jong, D.L. Olmsted, M. Asta, A. Dick, D. Shin, Y. Wang, L.-Q. Chen, and Z.-K. Liu. Efficient stochastic generation of special quasirandom structures. *Calphad*, 42:13–18, sep 2013. ISSN 03645916. doi: 10.1016/j.calphad.2013.06.006. URL https://linkinghub.elsevier.com/retrieve/pii/S0364591613000540.

[26] I. A. Abrikosov, S. I. Simak, B. Johansson, A. V. Ruban, and H. L. Skriver. Locally self-consistent Green's function approach to the electronic structure problem. *Physical Review B*, 56(15):9319–9334, oct 1997. ISSN 0163-1829. doi: 10.1103/PhysRevB.56.9319. URL https://link.aps.org/doi/10.1103/PhysRevB.56.9319.

[27] Dongwon Shin, Axel van de Walle, Yi Wang, and Zi-Kui Liu. First-principles study of ternary fcc solution phases from special quasirandom structures. *Physical Review B*, 76(14):144204, oct 2007. ISSN 1098-0121. doi: 10.1103/PhysRevB.76.144204. URL https://link.aps.org/doi/10.1103/PhysRevB.76.144204.

[28] Johann von Pezold, Alexey Dick, Martin Friák, and Jörg Neugebauer. Generation and performance of special quasirandom structures for studying the elastic properties of random alloys: Application to Al-Ti. *Physical Review B*, 81(9):094203, mar 2010. ISSN 1098-0121. doi: 10.1103/PhysRevB.81.094203. URL https://link.aps.org/doi/10.1103/PhysRevB.81.094203.

[29] Axel van de Walle. Multicomponent multisublattice alloys, nonconfigurational entropy and other additions to the Alloy Theoretic Automated Toolkit. *Calphad*, 33(2):266–278, jun 2009. ISSN 03645916. doi: 10.1016/j.calphad.2008.12.005. URL https://linkinghub.elsevier.com/retrieve/pii/S0364591608001314.

[30] Pierre Perrot. *A to Z of Thermodynamics*. Oxford University Press, New York, 1998. ISBN 9780198565529.

[31] F. D. Murnaghan. The Compressibility of Media under Extreme Pressures. *Proceedings of the National Academy of Sciences*, 30(9):244–247, sep 1944. ISSN 0027-8424. doi: 10.1073/pnas.30.9.244. URL http://www.pnas.org/cgi/doi/10.1073/pnas.30.9.244.

[32] Francis Birch. Finite Elastic Strain of Cubic Crystals. *Physical Review*, 71(11):809–824, jun 1947. ISSN 0031-899X. doi: 10.1103/PhysRev.71.809. URL https://link.aps.org/doi/10.1103/PhysRev.71.809.

[33] R. H. French, S. J. Glass, F. S. Ohuchi, Y. N. Xu, and W. Y. Ching. Experimental and theoretical determination of the electronic structure and optical properties of three phases of ZrO2. *Physical Review B*, 49(8):5133–5142, feb 1994. ISSN 0163-1829. doi: 10.1103/PhysRevB.49.5133. URL https://link.aps.org/doi/10.1103/PhysRevB.49.5133.

[34] Balázs Králik, Eric K. Chang, and Steven G. Louie. Structural properties and quasiparticle band structure of zirconia. *Physical Review B*, 57(12):7027–7036, mar 1998. ISSN 0163-1829. doi: 10.1103/PhysRevB.57.7027. URL https://link.aps.org/doi/10.1103/PhysRevB.57.7027.

[35] Jane P. Chang, You-Sheng Lin, and Karen Chu. Rapid thermal chemical vapor deposition of zirconium oxide for metal-oxide-semiconductor field effect transistor application. *Journal of Vacuum Science & Technology B: Microelectronics and Nanometer Structures*, 19(5):1782, 2001. ISSN 0734211X. doi: 10.1116/1.1396639. URL http://scitation.aip.org/content/avs/journal/jvstb/19/5/10.1116/1.1396639.

[36] Hong Jiang, Ricardo I. Gomez-Abal, Patrick Rinke, and Matthias Scheffler. Electronic band structure of zirconia and hafnia polymorphs from the GW perspective. *Physical Review B*, 81(8):085119, feb 2010. ISSN 1098-0121. doi: 10.1103/PhysRevB.81.085119. URL https://link.aps.org/doi/10.1103/PhysRevB.81.085119.

[37] Xinyuan Zhao and David Vanderbilt. Phonons and lattice dielectric properties of zirconia. *Physical Review B*, 65(7):075105, jan 2002. ISSN 0163-1829. doi: 10.1103/PhysRevB.65.075105. URL https://link.aps.org/doi/10.1103/PhysRevB.65.075105.

[38] Thomas Mayer, Wernfried Mayr-Schmölzer, Jakub Planer, and Josef Redinger. Co-adsorption studies of CO, CO2 and H2O on cubic(111) and

monoclinic(-111) ZrO2 surfaces. Technical report, Vienna University of Technology, 2018.

[39] E. V. Stefanovich, A. L. Shluger, and C. R. A. Catlow. Theoretical study of the stabilization of cubic-phase ZrO2 by impurities. *Physical Review B*, 49 (17):11560–11571, may 1994. ISSN 0163-1829. doi: 10.1103/PhysRevB.49.11560. URL https://link.aps.org/doi/10.1103/PhysRevB.49.11560.

[40] Pierre Aldebert and Jean-Pierre Traverse. Structure and Ionic Mobility of Zirconia at High Temperature. *Journal of the American Ceramic Society*, 68(1):34–40, jan 1985. ISSN 0002-7820. doi: 10.1111/j.1151-2916.1985.tb15247.x. URL https://onlinelibrary.wiley.com/doi/full/10.1111/j.1151-2916.1985.tb15247.x.

[41] M. W. Chase. NIST-JANAF Thermochemical Tables. *Journal of Physical and Chemical Reference Data*, 4:1769–1772, 1998.

[42] Yong-Nian Xu, Zhong-quan Gu, and W. Y. Ching. Electronic, structural, and optical properties of crystalline yttria. *Physical Review B*, 56(23):14993–15000, dec 1997. ISSN 0163-1829. doi: 10.1103/PhysRevB.56.14993. URL https://link.aps.org/doi/10.1103/PhysRevB.56.14993.

[43] C. E. Curtis. Properties of Yttrium Oxide Ceramics. *Journal of the American Ceramic Society*, 40(8):274–278, aug 1957. ISSN 0002-7820. doi: 10.1111/j.1151-2916.1957.tb12619.x. URL http://doi.wiley.com/10.1111/j.1151-2916.1957.tb12619.x.

[44] L. R. Morss, P. P. Day, C. Felinto, and H. Brito. Standard molar enthalpies of formation of Y2O3, Ho2O3 and Er2O3 at the temperature 298.15K. *Journal of Chemical Thermodynamics*, 25:415–422, 1993. doi: 10.1006/jcht.1993.1045.

[45] N. Ishizawa, Y. Matsushima, M. Hayashi, and M. Ueki. Synchrotron radiation study of yttria-stabilized zirconia. *Acta Crystallographica Section B Structural Science*, 55(5):726–735, oct 1999. ISSN 0108-7681. doi: 10.1107/S0108768199005108. URL http://scripts.iucr.org/cgi-bin/paper?S0108768199005108.

[46] L.H. Ahrens. The use of ionization potentials Part 1. Ionic radii of the elements. *Geochimica et Cosmochimica Acta*, 2(3):155–169, jan 1952. ISSN 00167037. doi: 10.1016/0016-7037(52)90004-5. URL http://linkinghub.elsevier.com/retrieve/pii/0016703752900045.

[47] R D Shannon. Revised effective ionic radii and systematic studies of interatomic distances in halides and chalcogenides. *Acta Crystallographica Section A*, 32(5):751–767, sep 1976. ISSN 0567-7394. doi: 10.1107/S0567739476001551. URL http://scripts.iucr.org/cgi-bin/paper?S0567739476001551.

[48] Jetske Karina Stortelder. *Ionic Conductivity in Yttria-Stabilized Zirconia Thin Films grown by Pulsed Laser Deposition*. PhD thesis, University of Twente, Twente, 2005. URL https://www.utwente.nl/en/tnw/ims/people/former-msc/files/JetskeStortelder.pdf.

[49] J. M. Dixon, L. D. LaGrange, U. Merten, C. F. Miller, and J. T. Porter. Electrical Resistivity of Stabilized Zirconia at Elevated Temperatures. *Journal of The Electrochemical Society*, 110(4):276, 1963. ISSN 00134651. doi: 10.1149/1.2425731. URL http://jes.ecsdl.org/cgi/doi/10.1149/1.2425731.

[50] D. W. STRICKLER and W. G. CARLSON. Ionic Conductivity of Cubic Solid Solutions in the System CaO-Y2O3-ZrO2. *Journal of the American Ceramic Society*, 47(3):122–127, mar 1964. ISSN 0002-7820. doi: 10.1111/j.1151-2916.1964.tb14368.x. URL http://doi.wiley.com/10.1111/j.1151-2916.1964.tb14368.x.

[51] R. E. W. Casselton. Low field DC conduction in yttria-stabilized zirconia. *Physica Status Solidi (a)*, 2(3):571–585, jul 1970. ISSN 00318965. doi: 10.1002/pssa.19700020319. URL http://doi.wiley.com/10.1002/pssa.19700020319.

[52] J. Kondoh, T. Kawashima, S. Kikuchi, Y. Tomii, and Y. Ito. Effect of Aging on Yttria-Stabilized Zirconia: I. A Study of Its Electrochemical Properties. *The Electrochemical Society*, 145(5):1292, 1998.

[53] J. Kondoh, S. Kikuchi, Y. Tomii, and I. Yasuhiko. Effect of Aging on Yttria-Stabilized Zirconia: II. A Study of the Effect of the Microstructure on Conductivity. *The Electrochemical Society*, 145(5):173, 1998.

[54] J Kondoh, S Kikuchi, Y Tomii, and V Ito. Effect of Aging on Yttria-Stabilized Zirconia: III. A Study of the Effect of Local Structures on Conductivity. *The Electrochemical Society*, 145(5):698, 1998.

[55] Nalini Balakrishnan, Tomonari Takeuchi, Katsuhiro Nomura, Hiroyuki Kageyama, and Yasuo Takeda. Aging Effect of 8 mol % YSZ Ceramics with Different Microstructures. *Journal of The Electrochemical Society*, 151(8):A1286, 2004. ISSN 00134651. doi: 10.1149/1.1769271. URL http://jes.ecsdl.org/cgi/doi/10.1149/1.1769271.

[56] B BUTZ, P KRUSE, H STORMER, D GERTHSEN, A MULLER, A WEBER, and E IVERSTIFFEE. Correlation between microstructure and degradation in conductivity for cubic Y2O3-doped ZrO2. *Solid State Ionics*, 177(37-38):3275–3284, dec 2006. ISSN 01672738. doi: 10.1016/j.ssi.2006.09.003. URL https://linkinghub.elsevier.com/retrieve/pii/S0167273806005066.

[57] B. Butz, R. Schneider, D. Gerthsen, M. Schowalter, and A. Rosenauer. Decomposition of 8.5mol.% Y2O3-doped zirconia and its contribution to the degradation of ionic conductivity. *Acta Materialia*, 57(18):5480–5490, oct 2009. ISSN 13596454. doi: 10.1016/j.actamat.2009.07.045. URL https://linkinghub.elsevier.com/retrieve/pii/S1359645409004790.

[58] H. G. Scott. Phase relationships in the zirconia-yttria system. *Journal of Materials Science*, 10(9):1527–1535, sep 1975. ISSN 0022-2461. doi: 10.1007/BF01031853. URL http://link.springer.com/10.1007/BF01031853.

[59] Hajime Suto, Taketo Sakuma, and Noboru Yoshikawa. Discussion on the Phase Diagram of Y2O3-Partially Stabilized Zirconia and Interpretation of the Structures. *Transactions of the Japan Institute of Metals*, 28 (8):623–630, 1987. ISSN 0021-4434. doi: 10.2320/matertrans1960.28.623. URL https://www.jstage.jst.go.jp/article/matertrans1960/28/8/28{_}8{_}623/{_}article.

[60] A.H. Heuer, R Chaim, and V. Lanteri. The displacive cubic - tetragonal transformation in ZrO2 alloys. *Acta Metallurgica*, 35(3):661–666, mar 1987. ISSN 00016160. doi: 10.1016/0001-6160(87)90189-1. URL http://linkinghub.elsevier.com/retrieve/pii/0001616087901891.

[61] Tatsuo Noma, Masahiro Yoshimura, Shigeyuki Somiya, Masaharu Kato, Mezame S. Yanagisawa, and Hiroshi Seto. Formation of diffusionlessly transformed tetragonal phases in rapid quenching of ZrO2-Y2O3 melts. *Journal of Materials Science*, 23(8):2689–2692, aug 1988. ISSN 0022-2461. doi: 10.1007/BF00547438. URL http://link.springer.com/10.1007/BF00547438.

[62] Masahiro Yoshimura, Masatomo Yashima, Tatsuo Noma, and Shigeyuki Somiya. Formation of diffusionlessly transformed tetragonal phases by rapid quenching of melts in ZrO2-RO1.5 systems (R = rare earths). *Journal of Materials Science*, 25(4):2011–2016, apr 1990. ISSN 0022-2461. doi: 10.1007/BF01045757. URL http://link.springer.com/10.1007/BF01045757.

[63] Yu Zhou, Ting-Chuan Lei, and Taketo Sakuma. Diffusionless Cubic-to-Tetragonal Phase Transition and Microstructural Evolution in Sintered Zirconia-Yttria Ceramics. *Journal of the American Ceramic Society*, 74(3):633–640, mar 1991. ISSN 0002-7820. doi: 10.1111/j.1151-2916.1991.tb04071.x. URL http://doi.wiley.com/10.1111/j.1151-2916.1991.tb04071.x.

[64] V. S. STUBICAN, R. C. HINK, and S. P. RAY. Phase Equilibria and Ordering in the System ZrO2-Y2O3. *Journal of the American Ceramic Society*, 61(1-2):17–21, jan 1978. ISSN 0002-7820. doi: 10.1111/j.1151-2916.1978.tb09220.x. URL http://doi.wiley.com/10.1111/j.1151-2916.1978.tb09220.x.

[65] Yingfen Wei, Pavan Nukala, Mart Salverda, Sylvia Matzen, Hong Jian Zhao, Jamo Momand, Arnoud S Everhardt, Guillaume Agnus, Graeme R Blake, Philippe Lecoeur, Bart J Kooi, Jorge Íñiguez, Brahim Dkhil, and Beatriz Noheda. A rhombohedral ferroelectric phase in epitaxially strained Hf0.5Zr0.5O2 thin films. *Nature Materials*, 17(12):1095–1100, dec 2018. ISSN 1476-1122. doi: 10.1038/s41563-018-0196-0. URL http://www.nature.com/articles/s41563-018-0196-0.

[66] Artem R. Oganov and Colin W. Glass. Crystal structure prediction using ab initio evolutionary techniques: Principles and applications. *The Journal of Chemical Physics*, 124(24):244704, jun 2006. ISSN 0021-9606. doi: 10.1063/1.2210932. URL http://aip.scitation.org/doi/10.1063/1.2210932.

[67] Colin W. Glass, Artem R. Oganov, and Nikolaus Hansen. USPEX—Evolutionary crystal structure prediction. *Computer Physics Communications*, 175(11-12):713–720, dec 2006. ISSN 00104655. doi: 10.1016/j.cpc.2006.07.020. URL https://linkinghub.elsevier.com/retrieve/pii/S0010465506002931.

[68] Andriy O. Lyakhov, Artem R. Oganov, Harold T. Stokes, and Qiang Zhu. New developments in evolutionary structure prediction algorithm USPEX. *Computer Physics Communications*, 184(4):1172–1182, apr 2013. ISSN 00104655. doi: 10.1016/j.cpc.2012.12.009. URL https://linkinghub.elsevier.com/retrieve/pii/S0010465512004055.

[69] M YASHIMA. Metastable-stable phase diagrams in the zirconia-containing systems utilized in solid-oxide fuel cell application. *Solid State Ionics*, 86-88:1131–1149, jul 1996. ISSN 01672738. doi: 10.1016/0167-2738(96)00386-4. URL http://linkinghub.elsevier.com/retrieve/pii/0167273896003864.

[70] Y. Suzuki. Phase transition temperature of ZrO2-Y2O3 solid solutions (2.4–6 mol% Y2O3). *Solid State Ionics*, 95(3-4):227–230, mar 1997. ISSN 01672738. doi: 10.1016/S0167-2738(96)00606-6. URL http://linkinghub.elsevier.com/retrieve/pii/S0167273896006066.

[71] O Fabrichnaya, S Lakiza, Ch Wang, M Zinkevich, C.G. Levi, and F Aldinger. Thermodynamic Database for the ZrO2-YO3/2-GdO3/2-AlO3/2 System and Application to Thermal Barrier Coatings. *Journal of Phase Equilibria & Diffusion*, 27(4):343–352, aug 2006. ISSN 15477037. doi: 10.1361/154770306X116270. URL http://openurl.ingenta.com/content/xref?genre=article{&}issn=1547-7037{&}volume=27{&}issue=4{&}spage=343.

[72] F Hund. Anomale Mischkristalle im System ZrO2-Y3O2 Kristallbau der Nernst-Stifte. *Zeitschrift für Elektrochemie*, 5(5), 1951. doi: 10.1002/bbpc.19510550505.

[73] František Hanic, M. Hartmanová, F. Kundracik, and E.E: Lomonova. Stabilization and Properties of High Temperature Forms of Zirconia. *Solid State Phenomena*, 90-91:303–308, apr 2003. ISSN 1662-9779. doi: 10.4028/www.scientific.net/SSP.90-91.303. URL https://www.scientific.net/SSP.90-91.303.

[74] Olga Fabrichnaya and Fritz Aldinger. Assessment of thermodynamic parameters in the system ZrO 2 –Y 2 O 3 –Al 2 O 3. *Zeitschrift für Metallkunde*,

95(1):27–39, jan 2004. ISSN 0044-3093. doi: 10.3139/146.017909. URL http://www.hanser-elibrary.com/doi/abs/10.3139/146.017909.

[75] Koichi Momma and Fujio Izumi. VESTA : a three-dimensional visualization system for electronic and structural analysis. *Journal of Applied Crystallography*, 41(3):653–658, jun 2008. ISSN 0021-8898. doi: 10.1107/S0021889808012016. URL http://scripts.iucr.org/cgi-bin/paper?S0021889808012016.

[76] Wernfried Mayr-Schmölzer. *First-Principles Studies of Zirconia and its Interface to Platinum-Zirconium Alloys*. PhD thesis, Technical University of Vienna, 2012. URL http://repositum.tuwien.ac.at/obvutwhs/content/titleinfo/1621601.

[77] Jessica A. Krogstad, Maren Lepple, Yan Gao, Don M. Lipkin, and Carlos G. Levi. Effect of Yttria Content on the Zirconia Unit Cell Parameters. *Journal of the American Ceramic Society*, 94(12):4548–4555, dec 2011. ISSN 00027820. doi: 10.1111/j.1551-2916.2011.04862.x. URL http://doi.wiley.com/10.1111/j.1551-2916.2011.04862.x.

[78] R. P. INGEL and D. LEWIS III. Lattice Parameters and Density for Y2O3-Stabilized ZrO2. *Journal of the American Ceramic Society*, 69(4):325–332, apr 1986. ISSN 0002-7820. doi: 10.1111/j.1151-2916.1986.tb04741.x. URL http://doi.wiley.com/10.1111/j.1151-2916.1986.tb04741.x.

[79] Vedran Vonk, Navid Khorshidi, Andreas Stierle, and Helmut Dosch. Atomic structure and composition of the yttria-stabilized zirconia (111) surface. *Surface Science*, 612:69–76, jun 2013. ISSN 00396028. doi: 10.1016/j.susc.2013.02.014. URL https://linkinghub.elsevier.com/retrieve/pii/S0039602813000654.

[80] Thomas Götsch, Wolfgang Wallisch, Michael Stöger-Pollach, Bernhard Klötzer, and Simon Penner. From zirconia to yttria: Sampling the YSZ phase diagram using sputter-deposited thin films. *AIP Advances*, 2016. ISSN 21583226. doi: 10.1063/1.4942818.

[81] Thomas Götsch, Michael Stöger-Pollach, and Simon Penner. From zirconia to yttria: sampling the crystallographic and electronic phase diagram using sputter-deposited YSZ thin films. In *European Microscopy Congress 2016: Proceedings*, pages 724–725. Wiley-VCH Verlag GmbH & Co. KGaA, Weinheim, Germany, dec 2016. doi: 10.1002/9783527808465.EMC2016.5801. URL http://doi.wiley.com/10.1002/9783527808465.EMC2016.5801.

[82] Atsushi Togo and Isao Tanaka. First principles phonon calculations in materials science. *Scripta Materialia*, 108:1–5, nov 2015. ISSN 13596462. doi: 10.1016/j.scriptamat.2015.07.021. URL https://linkinghub.elsevier.com/retrieve/pii/S1359646215003127.

[83] M. Sternik and K. Parlinski. Lattice vibrations in cubic, tetragonal, and monoclinic phases of ZrO2. *The Journal of Chemical Physics*, 122(6):064707, feb 2005. ISSN 0021-9606. doi: 10.1063/1.1849157. URL http://aip.scitation.org/doi/10.1063/1.1849157.

[84] Johannes Gugler, Thomas Astner, Andreas Angerer, Jörg Schmiedmayer, Johannes Majer, and Peter Mohn. Ab initio calculation of the spin lattice relaxation time T 1 for nitrogen-vacancy centers in diamond. *Physical Review B*, 98 (21):214442, dec 2018. ISSN 2469-9950. doi: 10.1103/PhysRevB.98.214442. URL https://link.aps.org/doi/10.1103/PhysRevB.98.214442.

[85] Konstantin Z. Rushchanskii, Stefan Blügel, and Marjana Ležaić. Ab initio phase diagrams of Hf–O, Zr–O and Y–O: a comparative study. *Faraday Discussions*, 2019. ISSN 1359-6640. doi: 10.1039/C8FD00104A. URL http://xlink.rsc.org/?DOI=C8FD00104A.

[86] Xin Xia, Richard Oldman, and Richard Catlow. Computational Modeling Study of Bulk and Surface of Yttria-Stabilized Cubic Zirconia. *Chemistry of Materials*, 21(15):3576–3585, aug 2009. ISSN 0897-4756. doi: 10.1021/cm900417g. URL http://pubs.acs.org/doi/abs/10.1021/cm900417g.

[87] G. Ballabio, M. Bernasconi, F. Pietrucci, and S. Serra. Ab initio study of yttria-stabilized cubic zirconia surfaces. *Physical Review B*, 70(7):075417, aug 2004. ISSN 1098-0121. doi: 10.1103/PhysRevB.70.075417. URL https://link.aps.org/doi/10.1103/PhysRevB.70.075417.

[88] Xiao-Gang Wang. Yttrium segregation and surface phases of yttria-stabilized zirconia (111) surface. *Surface Science*, 602(1):L5–L9, jan 2008. ISSN 00396028. doi: 10.1016/j.susc.2007.11.007. URL https://linkinghub.elsevier.com/retrieve/pii/S0039602807011326.

[89] A.J.A. Winnubst, P.J.M. Kroot, and A.J. Burggraaf. AES/STEM grain boundary analysis of stabilized zirconia ceramics. *Journal of Physics and Chemistry of Solids*, 44(10):955–960, jan 1983. ISSN 00223697. doi: 10.1016/0022-3697(83)90144-0. URL http://linkinghub.elsevier.com/retrieve/pii/0022369783901440.

[90] AJ Burggraaf, M Van Hemert, D Scholten, and AJA Winnubst. Defect Segregation in Y2O3 doped ZrO2. In Pierre Barret and Louis-Claude Dufour, editors, *Reactivity of Solids 1984: International Symposium Proceedings (Materials Science Monographs)*, chapter 28, page 1158. Elsevier Science Ltd, Amsterdam, 1985. ISBN 0444424962.

[91] G S A M Theunissen, A J A Winnubst, and A J Burggraaf. Segregation aspects in the ZrO2-Y2O3 ceramic system. *Journal of Materials Science Letters*, 8(1):55–57, jan 1989. ISSN 0261-8028. doi: 10.1007/BF00720250. URL http://link.springer.com/10.1007/BF00720250.

[92] Anthony E (Anthony Edward) Hughes. *X-ray photoelectron spectroscopy study of segregation phenomena in yttria-zirconia solid electrolytes*. PhD thesis, Royal Melbourne Institute of Technology, 1991.

[93] A. Christensen and Emily A. Carter. First-principles study of the surfaces of zirconia. *Physical Review B - Condensed Matter and Materials Physics*, 58 (12):8050–8064, 1998. ISSN 1550235X. doi: 10.1103/PhysRevB.58.8050.

[94] Ricardo Grau-Crespo, Norge Cruz Hernández, Javier F. Sanz, and Nora H. de Leeuw. Theoretical Investigation of the Deposition of Cu, Ag, and Au Atoms on the ZrO 2 (111) Surface. *The Journal of Physical Chemistry C*, 111 (28):10448–10454, jul 2007. ISSN 1932-7447. doi: 10.1021/jp0704057. URL http://pubs.acs.org/doi/abs/10.1021/jp0704057.

[95] Dominic T. Chaopradith, David O. Scanlon, and C. Richard A Catlow. Adsorption of Water on Yttria-Stabilized Zirconia. *The Journal of Physical Chemistry C*, 119(39):22526–22533, oct 2015. ISSN 1932-7447. doi: 10.1021/acs.jpcc.5b06825. URL http://pubs.acs.org/doi/10.1021/acs.jpcc.5b06825.

[96] Alexandr Gorski, Vitaliy Yurkiv, Dzmitry Starukhin, and Hans-Robert Volpp. H2O chemisorption and H2 oxidation on yttria-stabilized zirconia: Density functional theory and temperature-programmed desorption studies. *Journal of Power Sources*, 196(17):7188–7194, sep 2011. ISSN 03787753. doi: 10.1016/j.jpowsour.2010.09.090. URL https://linkinghub.elsevier.com/retrieve/pii/S0378775310016964.

[97] Maxim Shishkin and Tom Ziegler. The Oxidation of H 2 and CH 4 on an Oxygen-Enriched Yttria-Stabilized Zirconia Surface: A Theoretical Study Based on Density Functional Theory. *The Journal of Physical Chemistry C*, 112(49):19662–19669, dec 2008. ISSN 1932-7447. doi: 10.1021/jp808049p. URL http://pubs.acs.org/doi/10.1021/jp808049p.

[98] K. P. Huber and G. Herzberg. Constants of diatomic molecules. In *Molecular Spectra and Molecular Structure*, pages 8–689. Springer US, Boston, MA, 1979. doi: 10.1007/978-1-4757-0961-2_2. URL http://link.springer.com/10.1007/978-1-4757-0961-2{_}2.

[99] J. B. Hasted. Liquid Water: Dielectric Properties. In *The Physics and Physical Chemistry of Water*, pages 255–309. Springer New York, Boston, MA, 1972. doi: 10.1007/978-1-4684-8334-5_7. URL http://link.springer.com/10.1007/978-1-4684-8334-5{_}7.

[100] P.J. Linstrom and W.G. Mallard. NIST Chemistry WebBook, NIST Standard Reference Database Number 69.

[101] G. Herzberg. *Spectra Of Polyatomic Molecules*. New York, 1966.

[102] B. deB Darwent. Bond dissociation energies in simple molecules. Technical Report January, National Bureau of Standards, Gaithersburg, MD, 1970. URL https://nvlpubs.nist.gov/nistpubs/Legacy/NSRDS/nbsnsrds31.pdf.

Appendix

List of Abbreviations

ATAT	Alloy Theoretic Automated Toolkit
CE	Cluster Expansion
CG	Sequential Conjugate Gradient Minimisation
DAV	Blocked Davidson Scheme
DFT	Density Functional Theory
EOS	Equation of State
GGA	Generalized Gradient Approximation
LDA	Local Density Approximation
MCSQS	Monte Carlo Generator of Special Quasirandom Structures
PAW	Projector-Augmented-Wave Method
PBE	GGA by Perdew, Burke and Ernzerhof
RMM-DIIS	Residual Minimisation Method - Direct Inversion in the Iterative Subspace
SCAN	Strongly Constrained and Appropriately Normed Semilocal Density Functional
VASP	Vienna Ab Initio Simulation Package
YSZ	Yttria-Substituted-Zirconia

Conversion Table for YSZ

$x \rightarrow$	**mol%** Y_2O_3	**mol%** $YO_{1.5}$	**at%** Y(incl. O)	**at%** Y(excl. O)	**Zr/Y** Ratio
mol% Y_2O_3	/	$y = \frac{x}{2-x}$	$y = \frac{3x}{2-2x}$	$y = \frac{x}{2-x}$	$y = \frac{1}{1+2x}$
mol% $YO_{1.5}$	$y = \frac{2x}{1+x}$	/	$y = \frac{6x}{x+2}$	$y = x$	$y = \frac{1}{1+x}$
at% Y(incl. O)	$y = \frac{2x}{2x+3}$	$y = \frac{2x}{6-x}$	/	$y = \frac{2x}{6-x}$	$y = \frac{2}{6x+5}$
at% Y(excl. O)	$y = \frac{2x}{1+x}$	$y = x$	$y = \frac{6x}{x+2}$	/	$y = \frac{1}{1+x}$
Zr/Y Ratio	$y = \frac{1-x}{2x}$	$y = \frac{1-x}{x}$	$y = \frac{2-5x}{6x}$	$y = \frac{1-x}{x}$	/

Table 6.1: Conversion table from Götsch et al. [80] between concentration values for YSZ, where x corresponds to the top row and y to the farthest left column.

Characteristics of selected Molecules

Bond-Lengths and -Angles

	Bond Length [pm]	**Bond Angle** [°]	**Bond Energy** [kJ/mol]
$\mathbf{H_2}$ [98]	74.1_{H-H}		432
$\mathbf{H_2O}$ [99]	95.718_{O-H}	104.474_{H-O-H}	499
CO [100]	112.8_{C-O}		1077
$\mathbf{CO_2}$ [101]	116.2_{C-O}	180_{O-C-O}	532
$\mathbf{N_2O}$ [101]	118.4_{N-O}	180_{N-O-N}	481
NO [100]	115.4_{N-O}		201

Table 6.2: Bond-lengths and -angles of common molecules. Bond Energies taken from [102].

Properties of Molecules

H_2: non polar, very low polarizability, very weak donor and acceptor properties. Molecular adsorption only at low temperature (physisorption), under UHV conditions chemisorption generally not possible.

On reactive oxide surfaces, H_2 can dissociate to give a H^+ bound to a surface O- atom, and a H^- bound to a surface metal atom, but this action requires an under coordinated pair. On less reductive surfaces, H-atoms can be adsorbed through atomic hydrogen.

H_2O: It has a large dipole moment and a lone electron pair. Molecular adsorption happens mostly through heterolytic acid/base reactions. Under UHV conditions it often only adsorbs strongly on defects. Real powder systems adsorb water strongly through heterolytic dissociation (many defects).

For many surface reactions, the OH^- groups adsorbed at surface cations block molecular adsorption and reaction of other particles → so the surface has to be activated through desorption of water.

CO: has a small dipole moment and due to a lone electron pair it is only a weak donor. Bonds to transition metal surfaces are enhanced through back donation into the antibonding p-orbital, which means CO acts simultaneously as donor and acceptor.

The adsorption depends on the pre-treatment of the surface, CO may react with pre- adsorbed or lattice oxygen to give CO_2 or CO_3^{2-}, it may also react with hydroxyl groups to give $HCOO^-$.

CO_2: is a colourless and mostly inert gas. The molecule has a linear shape and is centrosymmetric, therefore it has no electric dipole moment.

N_2O: can react with oxygen vacancies to give N_2, which usually desorbs immediately, and O, filling lattice vacancies.

NO: is isoelectric with CO and adsorbs molecularly on under saturated cations, although the desorption is stronger than with CO. Reduction of NO by NH_3 or CO is very desirable as it removes two atmospheric pollutants simultaneously.

Density of States and STM-Images

Cubic ZrO_2 and c-ZrO_2 (111) Surface

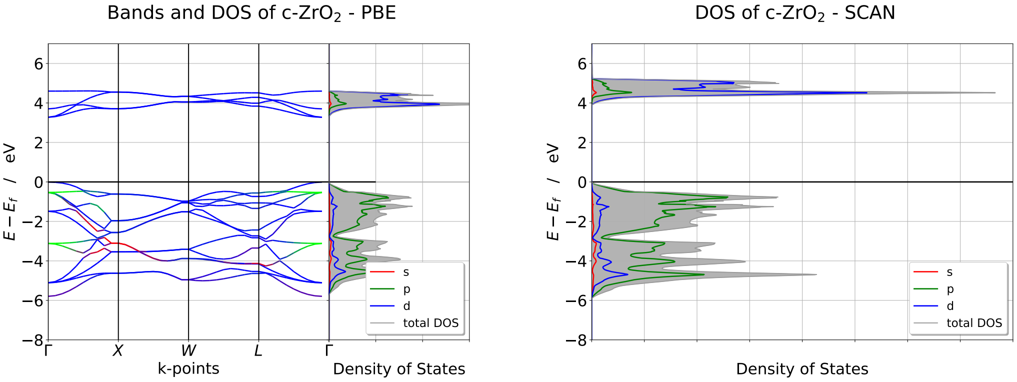

(a) **(b)**

Figure 6.1: Band spectra and density of states for cubic ZrO_2 calculated with (a) PBE and (b) SCAN functional. In both cases there is a band gap of approximately 4 eV.

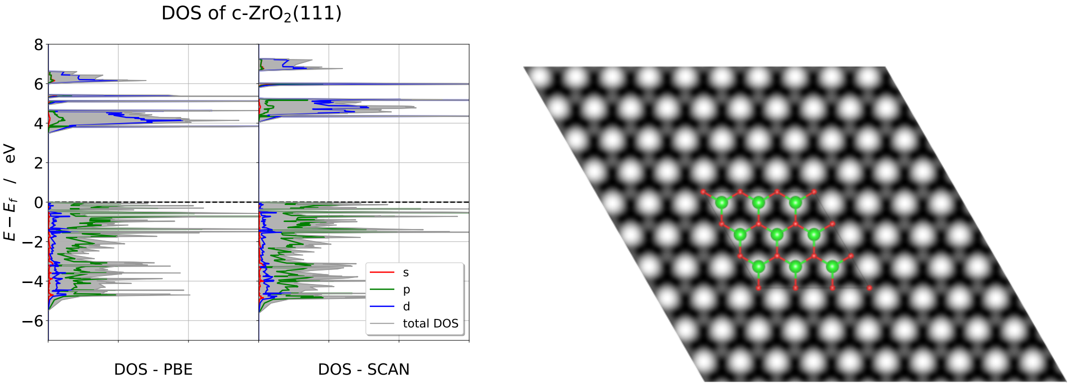

(a) **(b)**

Figure 6.2: Density of states for the c-ZrO_2 (111) surface calculated with (a) PBE and SCAN functional. (b) shows a simulated STM image of this surface (U_{bias} = 4 eV). The green balls are zirconium and the red balls are oxygen atoms.

Cubic Y_2O_3 and c-Y_2O_3 (111) Surface

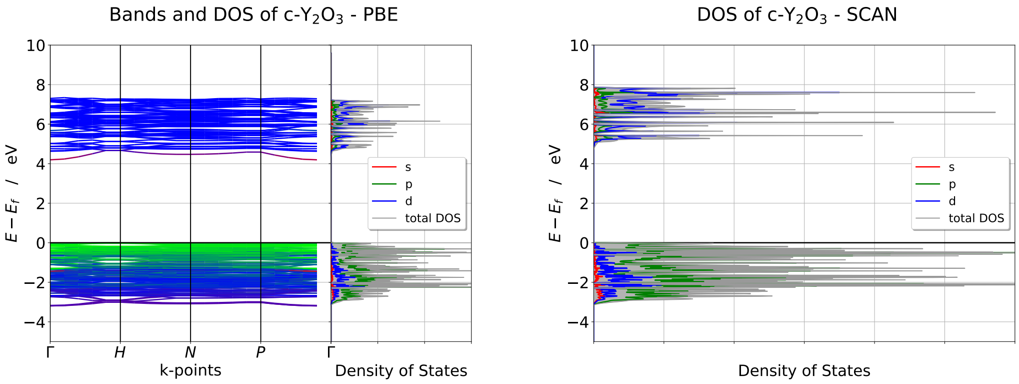

(a) **(b)**

Figure 6.3: Band spectra and density of states for cubic Y_2O_3 calculated with (a) PBE and (b) SCAN functional. There is a band gap of approximately 5 eV.

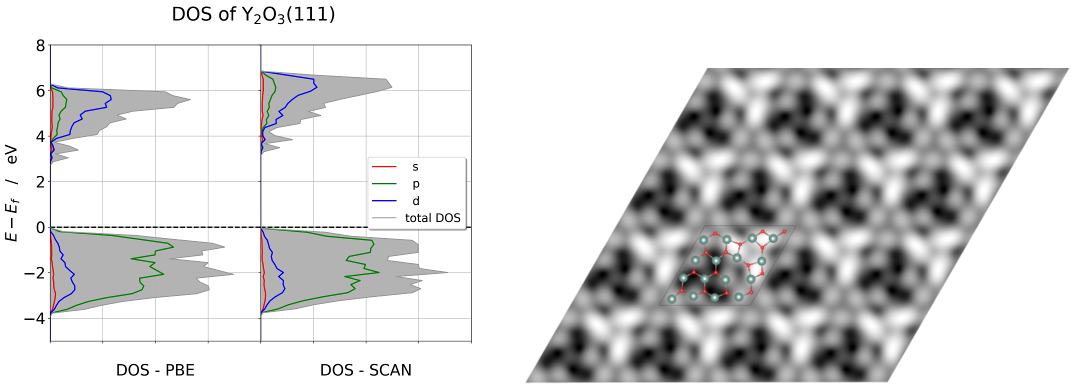

(a) **(b)**

Figure 6.4: Density of states for the c-Y_2O_3 (111) surface calculated with (a) PBE and SCAN functional. (b) shows a simulated STM image of this surface (U_{bias} = 5 eV). The gray balls are yttrium and the red balls are oxygen atoms. The lighter areas belong to 5-fold coordinated yttrium atoms though they are located at a lower height, compared to the darker area with 6-fold coordinated and higher located yttrium atoms.

10YSZ and 10YSZ(111) Surfaces

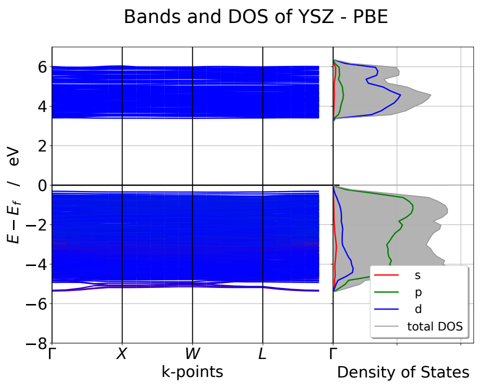

(a)

Figure 6.5: Band spectra and density of states for 10YSZ calculated with PBE functional. There is a band gap of approximately 3 eV to 4 eV, which would be larger when using SCAN functional.

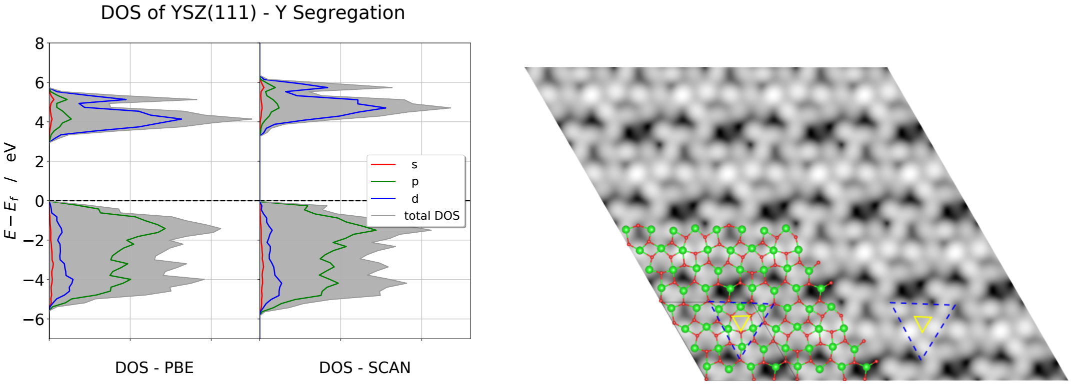

(a) **(b)**

Figure 6.6: (a) Density of states for the 10YSZ(111) surface with an yttrium subsurface layer calculated with the PBE and SCAN functional. (b) shows a simulated STM image of this surface (U_{bias} = 5 eV). The green balls are zirconium and the red balls are oxygen atoms. The previously mentioned triangle superstructure (blue triangle) with the oxygen vacancy in the surface (yellow triangle) is also marked.

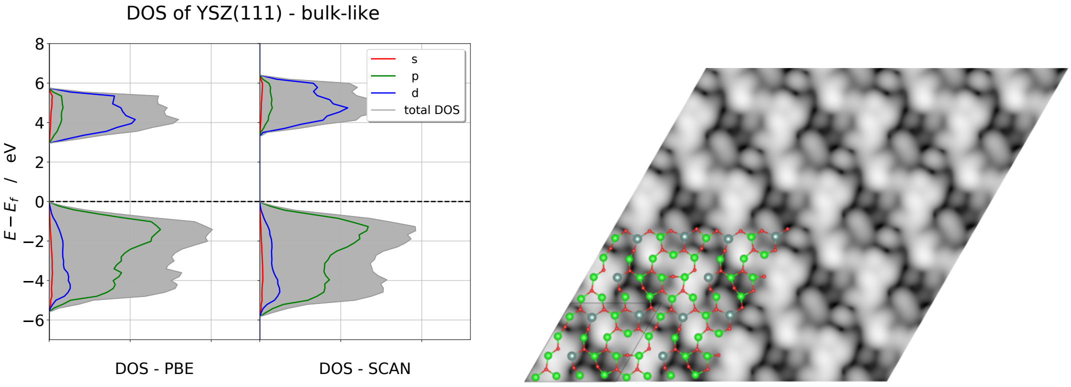

(a) **(b)**

Figure 6.7: (a) Density of states for the 10YSZ(111) bulk-like surface calculated with the PBE and SCAN functional. (b) shows a simulated STM image of this surface (U_{bias} = 5 eV). The green balls are zirconium, the gray balls are yttrium and the red balls are oxygen atoms.